FERMILAB-THESIS-2000-34

MEASUREMENT OF THE B^+ MESON CROSS SECTION IN PROTON-ANTIPROTON COLLISIONS AT 1.8 TEV USING THE FULLY RECONSTRUCTED DECAY $B^+ \to J/\psi\, K^+$

A Thesis

Submitted to the Faculty

of

Purdue University

by

Todd A. Keaffaber

In Partial Fulfillment of the

Requirements for the Degree

of

Doctor of Philosophy

May 2000

This thesis is dedicated to my wife Robin and my daughter Elora.

ACKNOWLEDGMENTS

The completion of a Ph.D. can be a long and frustrating journey. But with the help of several key and integral people, the road to completion was exciting and incredibly fulfilling. I would like to thank Daniela Bortoletto, my major professor, for her guidance, advice and intuition. Her inspiration and motivation were invaluable to me. I would like to thank Professor Arthur Garfinkel for the many discussions and his ability to always find a clear and, very often, novel way of approaching any problem presented. Many thanks also go to my Fermilab mentors Jonathan Lewis and Slawek Tkaczyk for their guidance and direction. Their experience and expertise have helped to make this accomplishment a reality. My gratitude and thanks go to Mark Bailey and Alvin Laasenen for their help and guidance. Being my predecessors, they were valuable resources and friends.

There were also many friends that I have made along the way which have made my graduate student career memorable. First, I would thank Andrew Scott for his friendship and the many discussions we've had that may or may not of contributed to this thesis. I would also like to thank Kara Hoffman and Adam Hardman for their advice. Finally, and most of all, I would like to thank my family. Thank you Robin and Elora for supporting and enduring this long journey. This is as much your accomplishment as it is mine. Also, thank you mom, dad, Scott, Brett and

Gregg for your love, understanding and support. This could not have been done without you.

TABLE OF CONTENTS

Page

Page

LIST OF TABLES

LIST OF FIGURES

Figure Page

Figure Page

Appendix
Figure

Figure Page

Figure Page

ABSTRACT

Keaffaber, Todd A., Ph.D., Purdue University May 2000. Measurement of the $B+$ Meson Cross Section in Proton-Antiproton Collisions at 1.8 TeV the Using Fully Reconstructed Decay $B^+ \to J/\psi\, K^+$. Major Professor: Daniela Bortoletto.

This thesis presents the measurement of the B^+ meson production cross section and the differential cross section, $d\sigma/dp_T$, from $p\overline{p}$ collisions at $\sqrt{s} = 1.8$ TeV. The B^+ meson is fully reconstructed using the exclusive decay $B^+ \to J/\psi K^+$ with $J/\psi \to \mu^+\mu^-$. The data set, consisting of about 110 pb^{-1}, was recorded by the Collider Detector at Fermilab during the 1992-1995 Tevatron run. The B^+ meson cross section was measured to be $3.52 \pm 0.38(stat) \pm 0.46(sys)\,\mu$b. The differential cross section is also presented.

1. INTRODUCTION

The study of heavy flavor production at the highest center-of-mass energy currently available provides the opportunity to check the accuracy of the quantum chromodynamic (QCD) predictions. There exist QCD calculations at next-to-leading order ($\mathcal{O}(\alpha_s^3)$) [1, 2] which, along with the parameterizations of the parton distribution functions down to $x \approx 10^{-5}$ [3], predict the b quark cross section. It is necessary to show that these predictions provide an adequate description of the cross section at 1.8 TeV before they can be confidently extrapolated to higher energies or more exotic phenomena.

In this thesis, the measurement of the B^+ meson production cross section in $p\overline{p}$ collisions at a center of mass energy of 1.8 TeV will be described. The analysis uses the decay $B^+ \to J/\psi K^+$ with $J/\psi \to \mu^+\mu^-$ and their charge conjugates. The data sample used represents an integrated luminosity of (108.1 ± 4.5) pb^{-1} collected by the Collider Detector at Fermilab (CDF) from 1992 to 1995 during the Tevatron collider run. The trigger requirements, which are based on the detection of the two muons from the J/ψ decay, will also be described along with the sources of contributions to the systematic uncertainty in the measurement.

2. B MESON PHENOMENOLOGY

The study of B^+ meson production in hadron colliders is of theoretical interest because it provides the opportunity to gauge the precision with which quantum chromodynamics (QCD) can be used to calculate the observed cross sections. $B^+(B^-)$ mesons are bound states of a $\overline{b}$ (b quark) and a $u(\overline{u}$) quark. While the binding is provided by the strong interaction B^+ mesons can only decay by the weak interaction. This chapter will provide a general description of the electroweak interactions and the hadronization of the B^+ mesons.

2.1 Electroweak Interactions

Quarks in their mass-eigenstate generations,

$$\begin{pmatrix} u \\ d \end{pmatrix} \begin{pmatrix} c \\ s \end{pmatrix} \begin{pmatrix} t \\ b \end{pmatrix} \tag{2.1}$$

may interact weakly with quarks in generations other than their own. The typical notation used to describe the degree of this "mixing" is the Cabibbo-Kobayashi-Maskawa (CKM) matrix[4, 5],

$$\begin{pmatrix} d' \\ s' \\ b' \end{pmatrix} = \begin{pmatrix} V_{ud} & V_{us} & V_{ub} \\ V_{cd} & V_{cs} & V_{cb} \\ V_{td} & V_{ts} & V_{tb} \end{pmatrix} \begin{pmatrix} d \\ s \\ b \end{pmatrix}, \tag{2.2}$$

which, by convention, leaves the +2/3-charged quarks unmixed; the states (d', s', b') are the weak eigenstates. Under the constraints that there be three quark gener-

ations and the CKM matrix be unitary, the mixing can be parameterized with three angles and one complex phase. The pursuit of measurements to determine the CKM matrix elements and to observe the charge-parity (CP) violation within the b-quark system (a result of a non-zero complex phase) constitutes a major component of many experimental programs at modern particle accelerators.

The understanding of the weak interactions has its foundations in Fermi's theory of β decay, introduced in 1934[6]. The four-fermion interaction was retained for several years before Sakurai introduced the universal V-A (vector and axial vector current) modification[7] to accommodate the experimentally observed parity violation. Unfortunately, the V-A Fermi theory violates unitarity violation (the predicted cross sections grew quadratically as a function of the center of mass energy) and is non-renormalizable at high energies. A theory is renormalizable if the predicted amplitudes of physical processes remain finite at all energies and for all powers of the coupling constant, often at the expense of the introduction of a finite number of experimentally determined parameters[8].

The "standard model" of electroweak interactions, developed primarily by Glashow, Weinberg, and Salam in the 1960's[9, 10, 11] and based on the gauge group $SU(2) \times U(1)$, hypothesized four intermediate gauge fields to avoid these difficulties: the W^+, W^-, Z^0, and the γ bosons. The standard-model electroweak Lagrangian that represents the charged-current weak interaction between fermion fields is

$$\mathcal{L}_{cc} = -\frac{g}{2\sqrt{2}} \sum_i \bar{\xi}_i \gamma^\mu (1-\gamma^5)(T^+ W_\mu^+ + T^- W_\mu^-)\xi_i \tag{2.3}$$

where g is the $SU(2)$ gauge coupling constant, $\gamma^\mu(1-\gamma^5)$ are the Dirac matrices representing the V-A current, T^+ and T^- are the weak isospin raising and lowering operators, respectively, $W_\mu^\pm$ are the massive weak charged boson fields, i represents the fermion families and ξ_i are the fermion fields. In charged-current

weak interactions of the b quark, the fermion fields are either left-handed $SU(2)$ doublets, $\xi_3 = \begin{pmatrix} t \\ \\ b' \end{pmatrix}_L$, or right-handed $SU(2)$ singlets, $\xi_3 = (b')_R$, where b' is the weak eigenstate defined in Equation (2.2).

2.2 b Quark Production

At the Tevatron in $p\overline{p}$ interactions, b quarks, and more generally heavy quarks, are produced in the hard collision of a parton from each hadron. The relativistic invariant phase space volume element for the final state b quark with four-momentum $p^\mu = (E, \vec{p})$ is

$$\frac{d^3p(b)}{E_b} = dy_b d^2p_T \tag{2.4}$$

where y is the rapidity defined as

$$y_b = \frac{1}{2}\ln\left(\frac{E_b + p_z(b)}{E_b - p_z(b)}\right) \tag{2.5}$$

The transverse momentum, p_T, of the b quark is the momentum projected on the plane perpendicular to the axis of the two income partons.

The differential cross section, $\hat{\sigma_{ij}}$, per invariant phase space volume for the production of a b quark can be written as

$$\frac{d^3\hat{\sigma_{ij}}}{dp_b^3/E_b} = \frac{E_b d^3\hat{\sigma_{ij}}}{dp_b^3}(x_i p_p, x_j p_{\bar{p}}, p_b; m_b, \mu, \Lambda) \tag{2.6}$$

where p_p and $p_{\bar{p}}$ are the momentum of the colliding hadrons, $x_i p_p$ and $x_j p_{\bar{p}}$ are the momenta of the incoming partons i and j, and p_b is the momenta of the outgoing b quark. The quantity Λ is an experimentally determined parameter used in the description of the dependence of the strong coupling constant, α_s, on the energy scale μ and m_b is the mass of the b quark.

The b quark differential cross section is found by integrating $E_b d^3\hat{\sigma_{ij}}/dp_b^3$ over all momentum fractions and summing over all types of partons in $p\overline{p}$ collision and is given as[1]

$$\frac{E_b d^3\sigma_{ij}}{dp_b^3} = \sum_{ij} \int dx_i dx_j \left(\frac{E_b d^3\hat{\sigma_{ij}}}{dp_b^3}(x_i p_p, x_j p_{\bar{p}}, p_b; m_b, \mu, \Lambda) \right) F_i^p(x_i, Q^2) F_j^{\bar{p}}(x_j, Q^2). \tag{2.7}$$

The structure functions, $F_i^p(x_i, Q^2)$ and $F_j^{\bar{p}}(x_j, Q^2)$, give the probability that a given parton will carry a momentum fraction, x, of its parent proton. These are determined experimentally by deep inelastic scattering of lepton-proton collisions. The parameter μ represents the energy scale of the process and Q^2 is the square of the four momentum transfer. By assumption, $|Q| \equiv \mu$, where $\mu = \sqrt{m_b^2 + p_T^2}$. The structure functions have an explicit Q^2 dependence resulting from the effects of the initial and final state gluon radiation that is included in the QCD calculations. Since the structure functions are measured at values of Q^2 that is lower than the momentum transfer at which the cross section is measured, they must be evolved to the appropriate value of Q^2. This is done using the Alterelli-Parisi equations using perturbative QCD[12].

The renormalization scale, μ, is introduced to handle divergent terms that arise in calculating $\hat{\sigma}$ at finite order in α_s. In a calculation to all orders in α_s, the divergent terms cancel out, so the calculation of $\hat{\sigma}$ would be independent of the choice of the renormalization scale. The scale is chosen such that the higher order terms that depend on $\log(Q^2/\mu^2)$ are well behaved at the scale involved in the interaction.

Integrating Equation (2.7) over the momentum p_B yields the total cross section of a b quark

$$\sigma(s) = \sum_{ij} \int dx_i dx_j \hat{\sigma_{ij}}(x_i p_p, x_j p_{\bar{p}}, p_b; m_b, \mu, \Lambda) F_i^p(x_i, \mu^2) F_j^{\bar{p}}(x_j, \mu^2) \tag{2.8}$$

where s is the square of the center of mass energy of the colliding proton and antiproton. The threshold condition for $b\bar{b}$ production is met when the square of the parton-parton center of mass energy, $\hat{s} \equiv x_i x_j s$ satisfies the condition $\hat{s} = 4m_b^2$.

The heavy mass of the b quark makes possible QCD calculations of $\hat{\sigma_{ij}}$ as a perturbative series in powers of the running coupling constant, α_s. The leading order terms ($\mathcal{O}(\alpha_s^2)$) of the series that contribute to the cross section, shown in Figure 2.1 are quark-antiquark annihilation and gluon-gluon fusion processes:

$$\begin{aligned} q + \bar{q} &\rightarrow b + \bar{b} \\ g + g &\rightarrow b + \bar{b}. \end{aligned} \tag{2.9}$$

The gluon-gluon fusion process is the dominant production mechanism for b quarks at the Tevatron. Some of the next-to-leading order terms ($\mathcal{O}(\alpha_s^3)$) in the α_s ex-

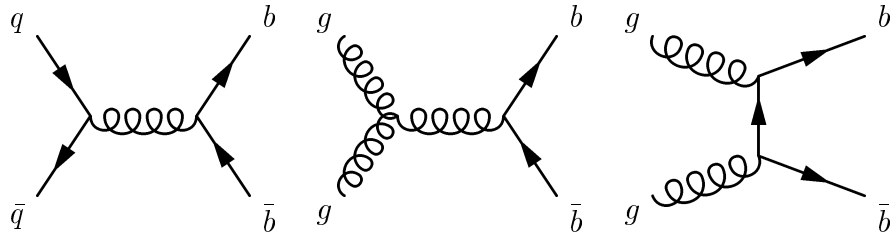

Fig. 2.1. Feynman diagrams for the lowest order ($\mathcal{O}(\alpha_s^2)$) mechanisms of b quark production. The diagram on the left is quark-antiquark annihilation. The center and right diagrams are gluon fusion processes which is the dominant heavy quark production mechanism at the Tevatron.

pansion are shown in Figure 2.2 and arise from processes [13] like:

$$\begin{aligned} q + \bar{q} &\rightarrow b + \bar{b} + g \\ g + g &\rightarrow b + \bar{b} + g \\ g + q &\rightarrow b + \bar{b} + q \\ g + \bar{q} &\rightarrow b + \bar{b} + \bar{q}. \end{aligned} \tag{2.10}$$

Due to the interference with diagrams containing virtual gluons, the two processes in Equation (2.9) can also contribute at $\mathcal{O}(\alpha_s^3)$. When the transverse momentum of

the b quark is much larger than its mass, some of the next-to-leading order $\mathcal{O}(\alpha_s^3)$ mechanisms contribute to the cross section by amounts comparable to the leading order $\mathcal{O}(\alpha_s^2)$ terms[1].

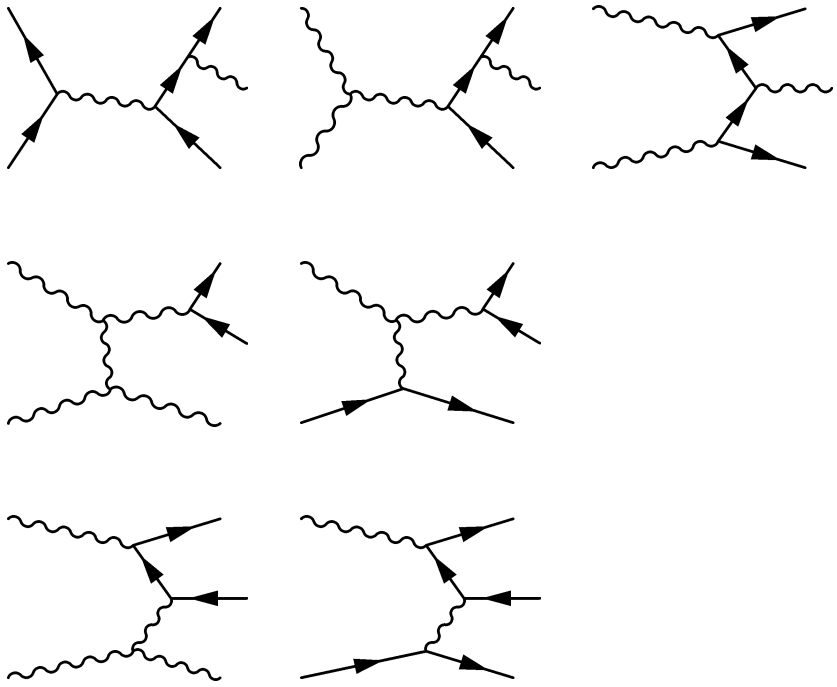

Fig. 2.2. Feynman diagrams for the next-to-leading order ($\mathcal{O}(\alpha_s^3)$) mechanisms of b quark production. The first row is hard gluon radiation, the second row is gluon splitting, and the last row is flavor exciation.

Theoretical uncertainties in the calculation of $\sigma(s)$ arise from the limited knowledge of the b quark pole mass, the choice of the renormalization scale μ, and the structure functions.The mass of the lightest $b\bar{b}$ state, $\Upsilon(1S)$ gives an estimate of the 4.75 GeV/c^2 for the mass of the b quark, and this is the value used in the cross section calculation.

2.3 Hadronization

The process of forming B hadrons from b quarks produced through hard scattering is called hadronization or fragmentation. It is a low Q^2, non-perturbative QCD process. The hadronization process is commonly described by the semi-empirical string fragmentation model[14] that describes the quark-antiquark interaction with the potential $V(r) \propto kr$. As the quark and the antiquark separate, the string stretches, and the potential energy increases until a new $q\bar{q}$ pair is created out of the vacuum to form the new ends of the string. The new strings can stretch and break, as well, and form more $q\bar{q}$ pairs until the available energy is exhausted. These new particles are referred to as fragmentation particles and include B hadrons. In the case of a B^+ meson, the quark combines with a u quark formed in the process.

The fragmentation process can be characterized by z, the fraction of of the initial b quark momentum that is carried by the B meson. The probability distribution of the B^+ meson p_T is described by a fragmentation function $D(z)$. Since fragmentation is a long-distance process and not calculable by perturbative QCD, a semi-empirical parameterization is used. Because the mass of the b quark is large, the B^+ meson it forms carries most of the initial p_T. Therefore, $D(z)$ is expected to peak near the maximum value of $z = 1$. The parameterization by Peterson *et al.* [15] incorporates this expectation:

$$D(z) = \frac{N}{z(1 - 1/z - \epsilon(1 - z))^2} \tag{2.11}$$

where N is set by the normalization requirement that $\int_0^1 D(z)dz = 1$. The term $1 - 1/z - \epsilon(1 - z)$ is the energy lost by the b quark through gluon emission. The Peterson parameter, ϵ, depends on the energy of the gluon products and is determined experimentally to be $\epsilon = 0.006 \pm 0.002$[16]. The value is based on a survey of several experimental e^+e^- observations. The search continues for better

understanding of b quark fragmentation, its sensitivity to the type of collision environment in which the b quark was produced and the flavor of the non-b quark constituting the final state hadron.

3. THE TEVATRON AND THE COLLIDER DETECTOR

The data used for this analysis were collected by the Collider Detector at Fermilab (CDF); a general purpose detector designed to study the collisions of protons and antiprotons. The collisions are produced using a superconducting collider, called the Tevatron, operating with six bunches of protons and antiprotons at a center-of-mass energy of $\sqrt{s} = 1.8$ TeV. The infrastructure utilized to produce the data sample is the synchronized result of many components working together from the production of the protons and antiprotons to their ultimate annihilation at the collision point within CDF. This chapter gives an overview of the accelerator complex and the CDF detector emphasizing the components of the detector that were instrumental for this measurement.

3.1 The Accelerator

The Tevatron, currently the world's highest energy accelerator, produces proton-antiproton collisions with a center-of-mass energy of 1.8 TeV. The process of providing high energy $p\overline{p}$ collisions requires a number of steps to get the particles to of collision. The Tevatron collider is the final stage in a series of seven accelerators[17, 18, 19] that are necessary for colliding the beams. A Cockroft-Walton pre-accelerator, a linear accelerator (Linac), and a synchrotron (Booster) operate in series to produce 8 GeV protons for injection into the Main Ring synchrotron. The Main Ring has two purposes: it serves as the final boosting stage

for protons and antiprotons before injection into the Tevatron, and it is the source of energetic protons which are used to produce antiprotons. The Antiproton Debuncher and the Antiproton Source are used in collecting and cooling the antiprotons for colliding beams. The overall layout of the accelerator complex is shown in Figure 3.1.

The process begins by ionizing hydrogen gas and accelerating the H^- ions to 750 keV in the Cockroft-Walton[20] electrostatic accelerator. The ions are fed into the 150 m Linac[20] which uses its 14 RF cavities and accelerates the negatively charged ions to 400 MeV. Both of these components can accelerate the beam once every 66 milliseconds.

From the Linac, the H^- ions are injected into the Booster, an alternating gradient proton synchrotron with a radius of 75 m, where the electrons are stripped off leaving only the protons. The booster accelerates the protons to 8 GeV and directs them to the Main Ring. The Main Ring is a circular synchrotron with a radius of 1000 m and which accelerates the protons up to 120 or 150 GeV. The proton beam that is accelerated to 120 GeV can be sent to the Antiproton source. As well as accepting the 8 GeV protons from the booster, the Main Ring can accept 8 GeV antiprotons and accelerate them up 150 GeV as well. The Main Ring can take as little as 2.4 seconds to accelerate the beam up to 150 GeV.

The Tevatron, located directly below the Main Ring in the same tunnel, can accept both protons and antiprotons from the Main Ring and accelerate them from 150 GeV to 900 GeV where they can be stored for hours. The use of superconducting magnets, which need to be cryogenically cooled, enables the Tevatron to accelerate the protons and antiprotons to higher energies than Main Ring even though they are the same size and shape.

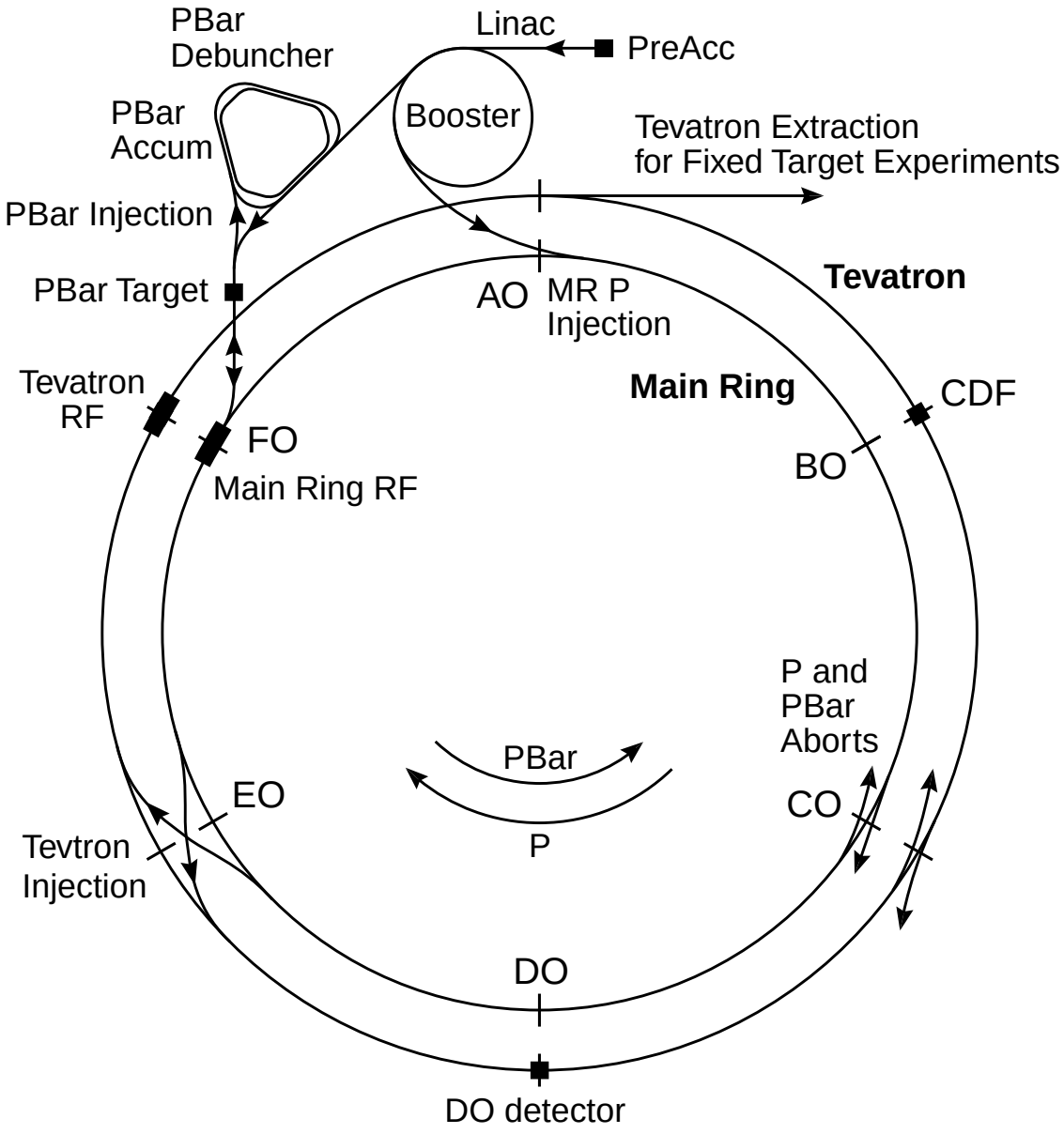

Fig. 3.1. The general layout of the collider facility at Fermilab (not to scale). Note that the Main Ring and the Tevatron are actually at the same radius but are shown separated in this figure for clarity.

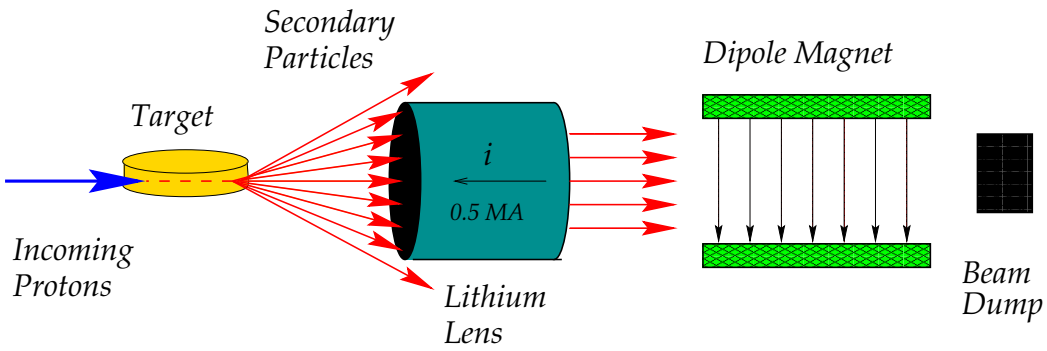

Fig. 3.2. Production of antiprotons.

Antiprotons[21] are produced using 120 GeV protons that are extracted from the Main Ring and directed to strike a nickel target as shown in figure 3.2. A lithium collection lens focuses the antiprotons and steers them to the Debuncher. The Debuncher[22] is one of the two synchrotrons that make up the antiproton source. The Debuncher is a rounded triangular shaped synchrotron with a mean radius of 90 m. It can accept 8 GeV protons from the Main Ring and 8 GeV antiprotons from the target station. The purpose of the Debuncher is to reduce the momentum spread and energy distribution of the antiprotons by bunch rotation and stochastic cooling[23]. The antiprotons are then transferred to the Accumulator for storage and cooling. The Accumulator is the second synchrotron of the Antiproton source and it is concentric with the Debuncher.

Once enough protons have been accumulated and the Tevatron has already been filled with 150 GeV protons bunches, antiprotons are transferred to the Main Ring, accelerated up to 150 GeV, and injected into the Tevatron in counter rotation to the protons. After the Tevatron has been filled with both protons and antiprotons, the two counter rotating beams are accelerated to 900 GeV and made to collide at several interaction regions.

Twelve counter circulating bunches, six bunches of protons and six bunches of antiprotons cross every 3.5 μs corresponding to a crossing frequency of 286

kHz. The instantaneous luminosity delivered to the CDF detector varied from a mean value of $\mathcal{L} = 3.5 \times 10^{30}\,\mathrm{cm}^{-2}\mathrm{s}^{-1}$ in Run 1A to a mean value of $\mathcal{L} = 8.0 \times 10^{30}\,\mathrm{cm}^{-2}\ \mathrm{s}^{-1}$ in Run 1B. Peak luminosities reached in Run 1B were as high as $\mathcal{L} = 2.6 \times 10^{31}\,\mathrm{cm}^{-2}\mathrm{s}^{-1}$. The typical bunch size in Run 1A was 12×10^{10} protons and 3×10^{10} antiprotons. For Run 1B, the number of protons per bunch was increased to 22.5×10^{10} and the number of antiprotons to 6.5×10^{10} per bunch. The CDF detector is located at the B0 interaction region where it records the 1.8 TeV collisions.

3.2 The CDF Detector

The CDF detector is a 5000 ton general purpose device designed to study the collisions of protons and antiprotons at energies of 1.8 TeV. A comprehensive description of the detector can be found in Reference [24]. CDF, shown in Figure 3.3, is composed of several specialized detector elements, each designed to identify a certain class of particle or to precisely measure their properties. Its capabilities include charged particle tracking, high resolution momentum measurement and finely segmented electromagnetic and hadronic calorimetry. Figure 3.4 shows a side view of one quadrant of the detector where the placement of each detector subsystem can be seen.

CDF is a cylindrical detector that surrounds the Tevatron beam pipe. The Cartesian coordinate system used is right handed with the z-axis pointing in the proton beam direction, the y-axis pointing up, and the x-axis pointing out of the Tevatron ring. The central detector region contains a large high resolution tracking chamber which operates in a 1.4 T magnetic field produced by a superconducting solenoid. The magnetic field is oriented along the proton beam. Since charged particles traversing the magnetic field follow helical trajectories, a cylindrical co-

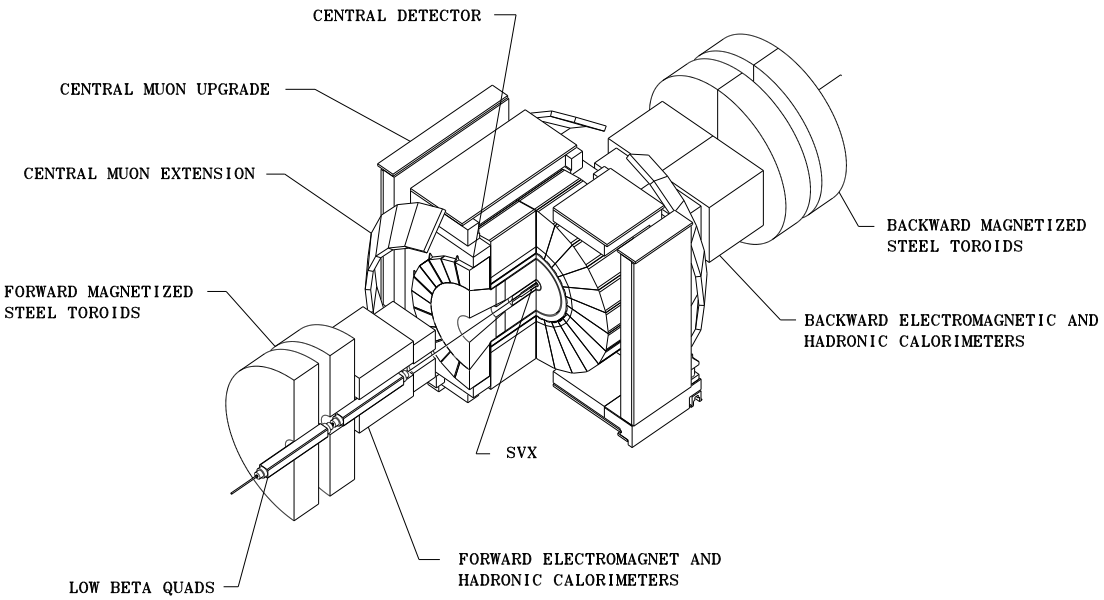

Fig. 3.3. An isometric view of the CDF detector with one quadrant cut away.

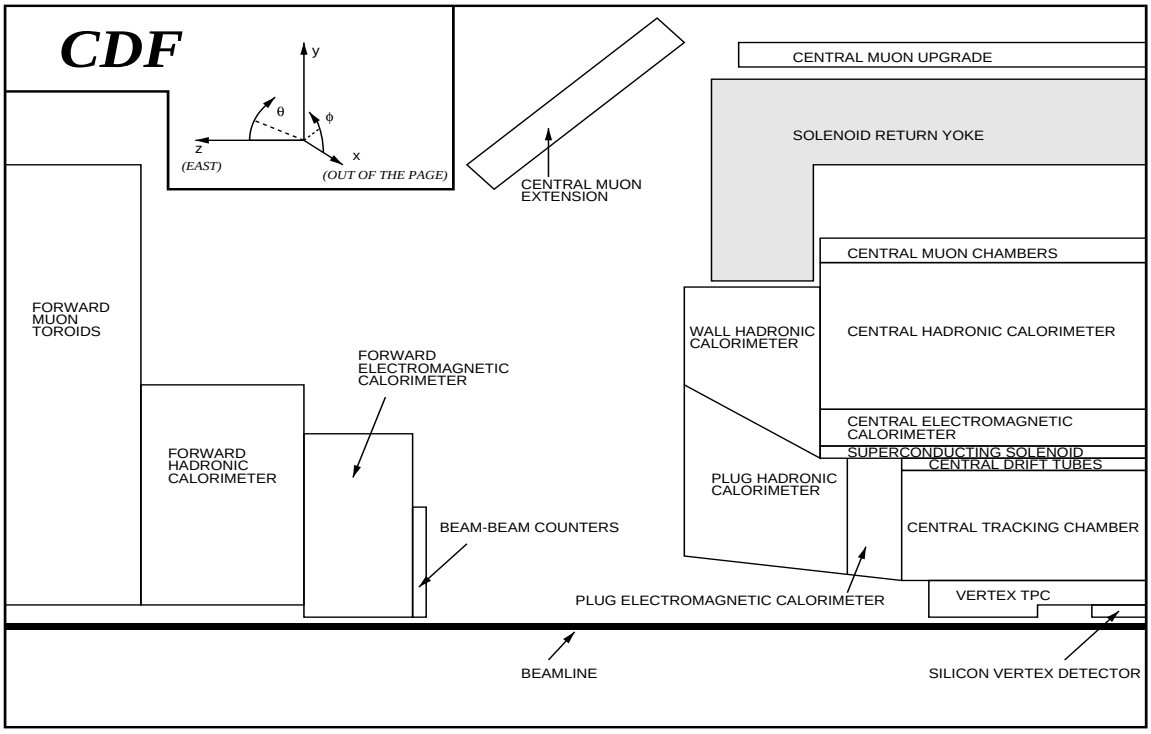

Fig. 3.4. A cross sectional view of one quadrant of the CDF detector. (Not drawn to scale)

ordinate system provides a natural description of the CDF geometry. Like the Cartesian system, the z-axis points along the proton beam and the zero value of z is defined at the center of the detector. The radial direction, r, and azimuthal angle, ϕ, have the standard definitions. A fourth variable, η, called pseudorapidity, is defined in terms of the polar angle, θ, as $\eta = -\ln(\tan(\theta/2))$.

3.3 Tracking Systems

The reconstruction of the exclusive decay $B^+ \rightarrow J/\psi\, K^+$ requires the precise measurement of each particles' charge, momentum and decay vertices. The measurement of theses quantities is accomplished by using four distinct but complimentary tracking subsystems: the silicon vertex detector (SVX), the vertex time projection chamber (VTX), the central tracking chamber (CTC), and the central muon chambers (CMU).

3.3.1 The Silicon Vertex Detector (SVX)

The first tracking subsystem outside the Tevatron beam pipe is the SVX. The SVX[25, 26] is a four layer silicon microstrip vertex detector that consists of two identical barrels that meet at $z = 0$ yielding a total active length of 51 cm . Figure 3.5 shows an isometric view of one of the barrels. The SVX was designed to extrapolate the track's helical path back into the region within the beam pipe with a precision high enough to differentiate secondary from primary vertices. Prompt tracks extrapolate to the primary vertex while non-prompt tracks originate from a secondary vertex. Since the luminous region of the $p\overline{p}$ interaction region is a Gaussian distribution having a standard deviation of $\sigma \sim 30$ cm, approximately 60% of the $p\overline{p}$ interaction vertices lie within the geometrical acceptance of the SVX.

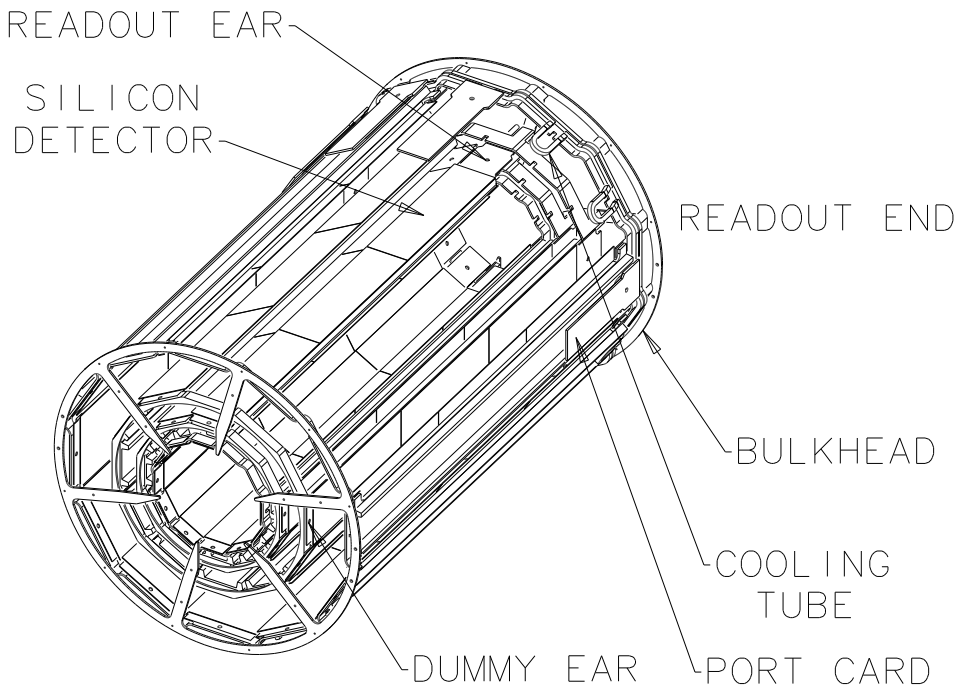

Fig. 3.5. An isometric view of one of the two silicon microstrip detector barrels showing the ladder arrangement and the support frame.

For Run 1B a new silicon vertex detector, SVX′ [27], was installed to replace the SVX used in Run 1A. The replacement was warranted due to the radiation damage the SVX had sustained resulting in increased leakage current and a significant degradation in hit efficiency by the end of Run 1A. The SVX′ was very similar in design to the SVX. The major differences being that the DC coupled silicon microstrip detectors of the SVX were replaced in the SVX′ by AC coupled devices to reduce leakage current and coherent noise, the readout chips were upgraded to be radiation hard for the increased luminosity of Run 1B, and the inner radius was reduced from 3.00 cm to 2.86 cm to eliminate some of the geometrical cracks in the inner most layer. Unless otherwise noted, references to the SVX apply to the SVX′ as well.

In both barrels of the SVX, the four layers are each segmented in twelve ladders that subtend approximately 30° in azimuth and are oriented parallel to the beam. A ladder is constructed from three detectors which are bonded together end to end to form a single unit with an active region of 25.5 cm, as shown in Figure 3.6.

Each sensor is composed of p-type silicon strips embedded in an n-type silicon wafer which is approximately 300 μm thick. A reverse bias voltage is applied across the sensor to deplete the wafer of mobile charge carries. This is accomplished by taking advantage of the pn junction created at each implant strip. When a charged particle passes through the detector, pairs of electrons and holes are created. The electrons drift to the nearest strip along the electric field line and induces a current. Since the implant strips run parallel to the beam and the wire bonding of the three detectors essentially creates strips that run the length of the barrel, only ϕ information is obtained from charge collection. The SVX cannot provide z position information because of the lack of segmentation of the barrels in the z direction. The radial information is provided by the layer number.

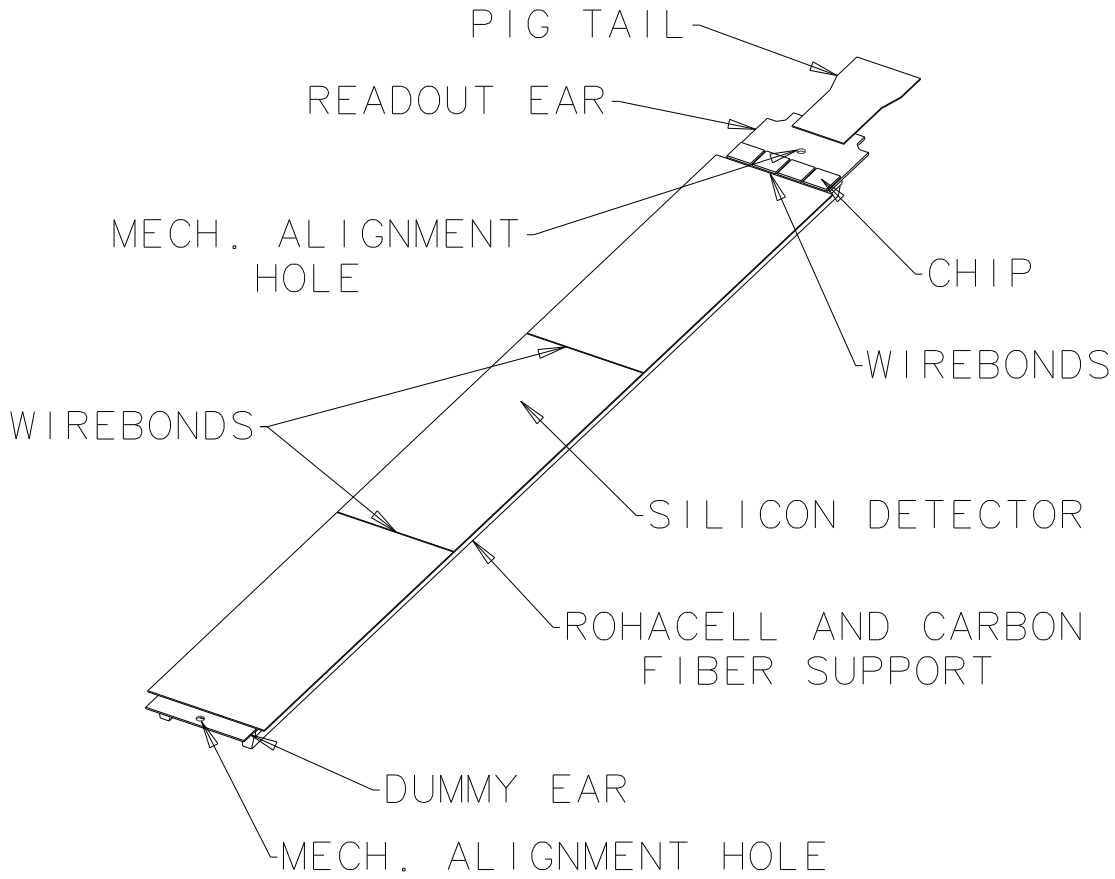

Fig. 3.6. An SVX ladder constructed from three silicon detectors, readout electronics, and support structure.

The inner three layers have strip pitch of 60 μm, while the outer layer has a strip pitch of 50 μm. The average position resolutions for the SVX and the SVX$'$ were measured to be 13 μm and 11.6 μm, respectively, and the high transverse momentum (asymptotic) impact parameter resolution was determined to be 17 μm for the SVX and 13 μm for the SVX$'$. Adjacent ladders in a given layer slightly overlap each other to provide full azimuthal coverage. This is achieved with a 3° rotation of the ladders about their major axes. The SVX$'$ has all four of its layer overlapped, however, the the innermost layer of the SVX suffers from a 1.26° gap in ϕ between adjacent ladder modules.

As shown in Figure 3.6, the readout end of each ladder has a small circuit board that contains readout chips, each of which serve 128 channels. Because the ladder widths increase with radius, the number of readout strips on a given ladder module depends on the layer in question. The innermost layer, for example, has 256 readout strips whereas the outermost layer has 768 readout strips. The total number of readout strips on the SVX is 46,080.

Since the silicon strips in the SVX$'$ are AC coupled to the readout chips, while those for the SVX were DC coupled, the SVX$'$ benefits from a marked reduction in noise compared to the SVX. An additional advantage of the AC coupled SVX$'$ design is that the readout chip preamplifiers, which have 40% more gain than their SVX counterpart, will not saturate, even after significant radiation damage has increased the silicon microstrip leakage current appreciably. These features allowed the SVX$'$ to handle the increased luminosities delivered during Run 1B.

3.3.2 The Vertex Time Projection Chamber (VTX)

The VTX, a vertex time projection chamber surrounding the SVX, was designed to measure the trajectories of charged particles in the r-z plane in a pseu-

dorapidity range $|\eta| < 3.0$. The VTX is important for the determination of the z position of the primary vertex and the identification of multiple interactions in the same beam crossing. The VTX resolution of a primary vertex location along the beam line, which is nominally 2 mm, depends on the number of detected tracks originating from that location and the number of primary $p\overline{p}$ interactions in the event.

The VTX, which extends 132 cm from the detector center in each z direction and has a radius of 22 cm, consists of 28 drift modules. Each module contains two drift regions separated by an aluminum high voltage grid to minimize drift time. End caps on each side of the drift modules are azimuthally segmented into octants, see Figure 3.7, and are rotated by 15° with respect to the adjacent modules (in z) to eliminate inefficiencies near module boundaries. Within each octant, 16 or 24 sense wires, depending on the z position of the module, are oriented tangentially, thereby providing tracking information in the r-z view. The z location of a track with respect to a given wire in a given module is determined by the drift time, and the r information is determined from the radial location of the wire. The electric field is maintained near 1.6 kV/cm and the gas used is a 50:50 mixture of argon and ethane.

3.3.3 The Central Tracking Chamber (CTC)

The largest tracking subsystem of the CDF detector is the CTC; a drift chamber covering the pseudorapidity range of $-1.0 < \eta < 1.0$. It is the only device that can perform three dimensional momentum and position measurements; both of which are essential to the reconstruction of exclusive B^+ meson decays. The CTC surrounds the VTX and the SVX and has an inner diameter of 55.4 cm , an outer diameter of 276.0 cm and a length of 320.13 cm [28].

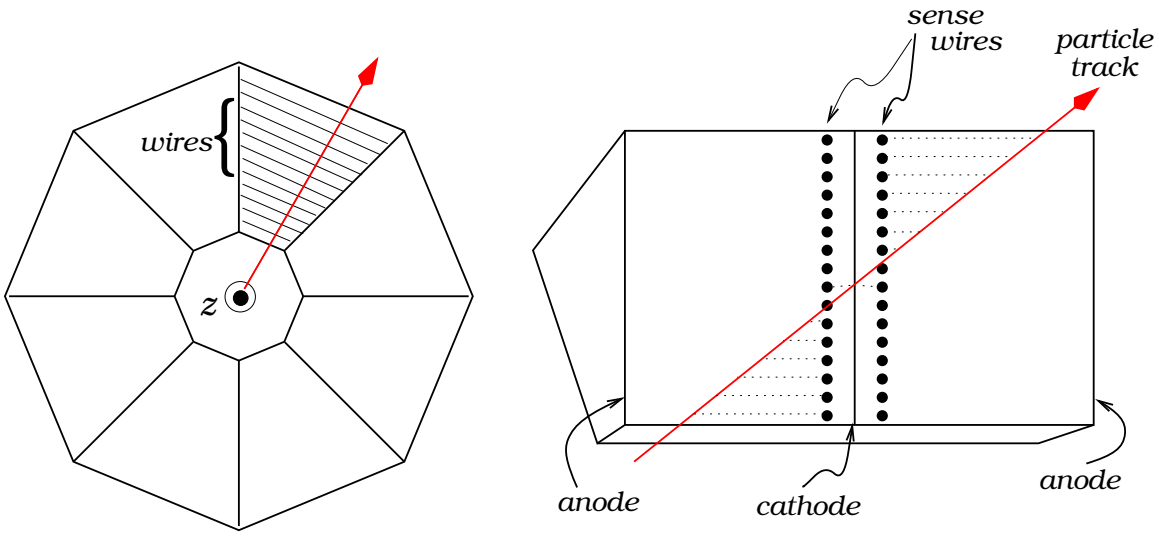

Fig. 3.7. Schematic diagram of the VTX. The left shows a cross section of one drift module in the plane perpendicular to the beam line showing the orientation of the sense wires. The right shows the side view of one octant of a drift module with an example particle track.

The CTC contains 84 layers of 40 μm diameter gold plated tungsten sense wires arranged into 9 superlayers. Five layers have 12 sense wires oriented parallel to the beam line, called the axial super layers, and the other four layers have six sense wires tilted 3° with respect to the beam line called the stereo super layers. A stereo superlayer lies between each axial superlayer. Starting with the innermost superlayer labelled as 0, layers 0, 2, 4, 6, and 8 are axial superlayers and layers 1, 3, 5, and 7 are stereo. The configuration is illustrated in Figure 3.8 which shows the wire slot location in the aluminum end plates. The majority of the CTC pattern recognition recognition is done using the data from the axial layers, which provide the r-ϕ tracking information. The stereo layers furnish the tracking information in the r-z view.

Each superlayer is divided into open drift cells which are tilted at an angle of 45° with respect to the radial direction. For a drift field value of 1350 kV/cm and a magnetic field of 1.4 T in the argon/ethane/alcohol gas mixture that fills

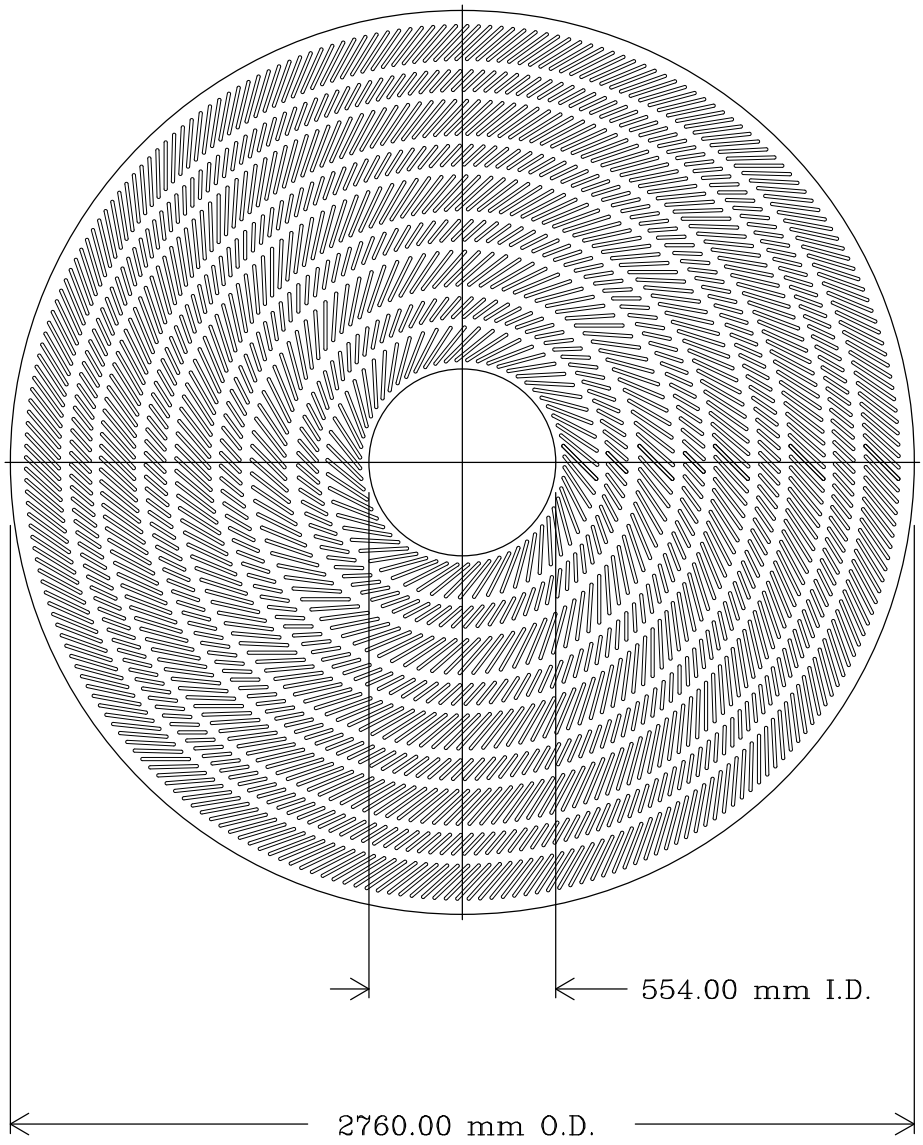

Fig. 3.8. The CTC end plate viewed along the z axis showing the location of the wire slots for the axial and stereo superlayers.

the chamber, this tilt causes the electrons produced by charged particles to drift in a direction perpendicular to the radial direction. The tilt also allows cells to be overlapped by about 20% and helps to resolve ambiguities in the pattern recognition.

The part of the particle trajectory that is reconstructed in the axial superlayers is a circular arc in the r-ϕ plane. The curvature of the arc varies inversely with the transverse momentum of the particle. As the momentum increases, the curvature of the track becomes more uncertain as the arc approaches a straight line. The r-ϕ resolution of the chamber is better than 200 μm at each wire layer. The r-z resolution is not as good and is on the order of 1 cm. Constraining tracks from the same particle to originate from a common vertex results in an overall momentum resolution of the combined SVX-CTC system of $\delta p_T/p_T = \sqrt{(0.0009 p_T)^2 + (0.0066)^2}$, where p_T is the transverse momentum in units of GeV/c.

3.4 Central Muon Detector (CMU)

The CMU provides muon identification out to $|\eta| \leq 0.6$ and resides on the outer edge of the central hadronic calorimeter, 347.0 cm from the beam axis, as indicated in Figure 3.9. Each 12.6° azimuthal wedge comprises three modules, each subtending 4.2° in ϕ.

A CMU module, shown in Figure 3.10 consists of four towers, each with four layers of rectangular drift cells. A sense wire which extends parallel to the beam line is located near the center of each cell. The r-ϕ location of the sense wire is offset by 2 mm for alternate layers. That is, the outermost and second innermost cells in each tower are oriented such that their sense wires lie on a radial line that originates from the geometric center of the detector. The other two drift cells are offset to determine which side of the radial line the track passed. As labeled in 3.10,

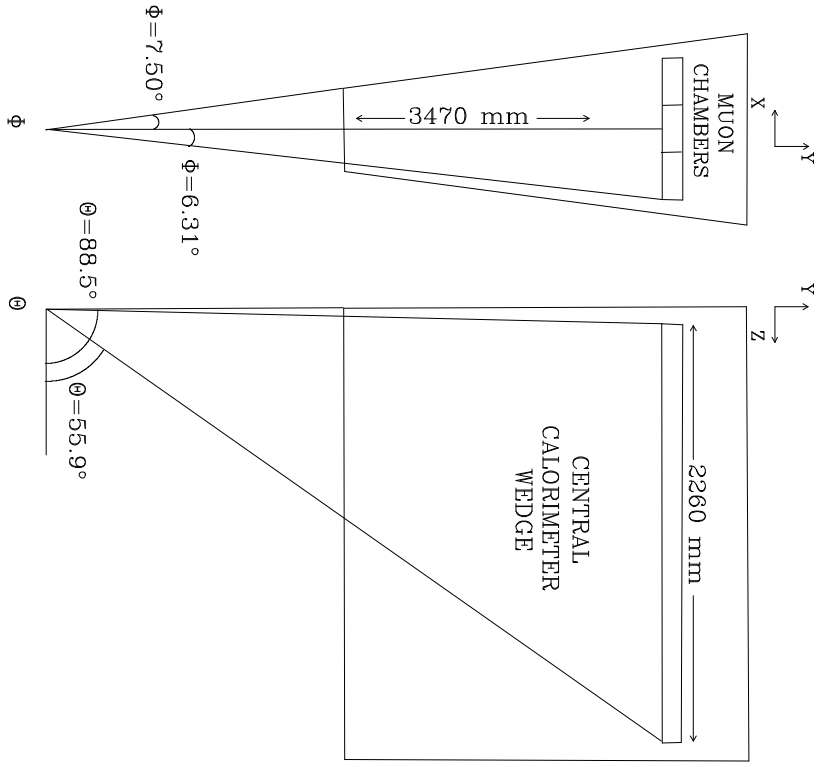

Fig. 3.9. The layout of the central muon (CMU) wedge with respect to the central hadronic calorimeter wedge in both the azimuthal (left figure) and polar (right figure) views.

the quantities t_2 and t_4 represent drift electron arrival times and their difference, $|t_4 - t_2|$, determines the angle between the candidate muon and the radial line. This provides a crude, but fast measurement of the muon's transverse momentum through the relation

$$\alpha \approx \sin\alpha = \frac{eL^2B}{2Dp_T} \tag{3.1}$$

where α is the angle between the muon track and the radial direction, e is the muon charge, B is the magnetic field, L is the radius of the solenoidal coil, and D is the radius of the innermost sense wire plane of the muon chambers.

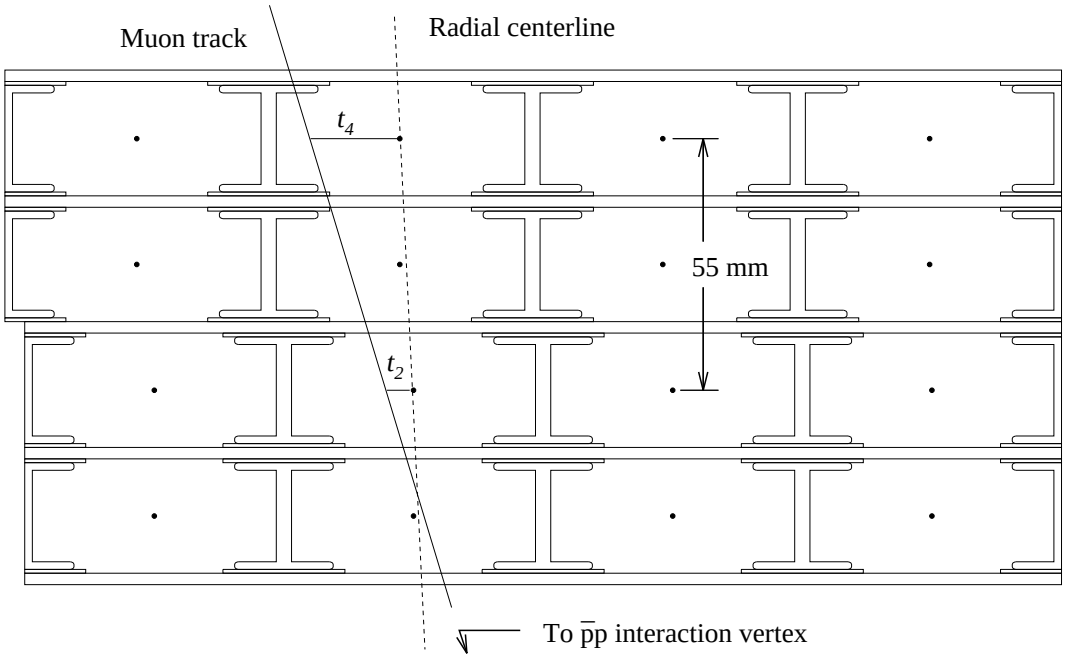

Fig. 3.10. Layout of a central muon detector (CMU) module showing the four towers, each with four layers of rectangular drift cells.

The relationship between the drift times and the transverse momentum of the muon allows implementation of a Level 1 trigger, which will be discussed in Chapter 4. The pulse height at each end of the sense wire is recorded allowing the position

of the particle track in z to be determined by charge division. The resolution achieved is 1.2 mm in the z direction and 200 μm in r-ϕ.

4. DATA SAMPLE AND EVENT SELECTION

This chapter discusses the method of selecting the B^+ meson candidates. It should be noted that any reference to a specific charge state also implies the the charge conjugate state. The decay channel used is $B^+ \to J/\psi\, K^+$ where the J/ψ is required to decay into two muons. The general algorithm for identifying a B^+ meson candidate is to combine two muon tracks, constrain them to come from a common point in space, and calculate their invariant mass. If it is within acceptable limits of the world average J/ψ mass, then another track is added assuming that it has the mass of a kaon. The three tracks are fit to a common vertex which is required to be displaced from the beam line while constraining the two muon tracks to the world average mass of the J/ψ. The three track invariant mass is formed and the distribution of the B^+ meson candidates is then fit to determine the number of signal events over background.

4.1 The Data Sample

The experimental data used in this measurement, referred to as Run 1, were recorded, using the CDF detector, from 1992 to 1995. Run 1 is comprised of two data-taking intervals known as Run 1A and Run 1B. The Run 1A data set took approximately nine months to collect starting from August of 1992 and ending in May of 1993. The data collected during Run 1A correspond to a time-integrated luminosity of $\int \mathcal{L} dt = (19.6 \pm 0.8)$ pb^{-1}. Run 1B began in January of 1994

and ended in July of 1995. The recorded time-integrated luminosity was $\int \mathcal{L}dt = 89.0 \pm 3.6$ pb^{-1} yielding a combined Run 1 total of $\int \mathcal{L}dt = 108.6 \pm 4.5$ pb^{-1}.

The intervening period between the end of Run 1A to the beginning of Run 1B was used to improve the CDF detector. The SVX was replaced with SVX$'$, as described in chapter 3, new trigger requirements and hardware were implemented, and a significantly improved data acquisition system was commissioned.

Even though the CDF detector underwent several significant changes between Run 1A and Run 1B, the present study used the entire Run 1 sample. The differences between the two data sets, such as the trigger efficiency and the track reconstruction efficiency, were accounted for in the analysis. Therefore, with these corrections, the Run 1 data set could be regarded as a single uniform sample.

4.2 The Trigger System

The purpose of the triggering system was to reduce the rate at which data was written to tape while still selecting interesting physics events. Over the course of Run 1, the CDF detector was exposed to an estimated 12.5 trillion $p\overline{p}$ collisions[29]. A CDF event, which amounted to the digitized information of a bunch crossing that could be read out from the CDF detector, had a data length of ∼165 kB. Such an event size could only be reliably written out to several 8 mm magnetic tapes at a rate of approximately 10 Hz, which constitutes the principal limitation of the CDF data acquisition system. A three level trigger system was designed to accommodate the $p\overline{p}$ interaction rate and select interesting physics events with a ∼30,000:1 rejection factor. Each level employed a logical "OR" of a limited number of programmable selection criteria that collectively reduced the data rate exposed the next higher trigger level. The reduction in rate presented to the higher trigger levels provided time for more sophisticated analyses of potential

events while decreasing the amount of time that the CDF detector was unable to consider subsequent $p\overline{p}$ events, referred to as dead time.

4.2.1 Level 1

The Level 1 trigger required less time than the 3.5 μs bunch crossing period to reach a decision on whether or not a given event passed the criteria to go on to Level 2; it therefore incurred no dead time. The short decision time was achieved by the analog read-out and processing of data from selected components with dedicated "FASTBUS"-based electronics[30]. At an instantaneous luminosity of $\mathcal{L} = 5 \times 10^{30}\,\mathrm{cm}^{-2}\mathrm{s}^{-1}$, the Level 1 trigger acceptance rate was approximately 1 kHz[31]. Although it could have been configured to base its decisions on information from several different subsystems, the typical Level 1 trigger primarily used signals from the calorimeters and the muon systems. Since this measurement required muon identification, only the muon component of the Level 1 trigger will be described.

The muon component of the Level 1 trigger exploited the relative drift electron arrival times Δt between pairs of drift cell layers in a given CMU module, as described in Section 3.4. The two cells constituting each of these pairs were separated in r by one drift cell, as shown in Figure 3.10. The trigger logic operated on objects, called muon stubs, that were defined by the existence of any wire pair in a 4-tower 4.2° muon detector module with a Δt less than a value corresponding to a given minimum p_T requirement.

Out of the seven Level 1 triggers that involved muon candidates, two were directly relevant to this analysis because they specifically identified dimuon candidates in the central region of the CDF detector. One of these dimuon triggers (TWO_CMU_3PT3) required that the two CMU stubs exist, whereas the other (TWO_CMU_CMX_3PT3) required that the two stubs each be in either the

CMU or the CMX (central muon extension) modules. Even though CMX muons were not used in this analysis, the latter trigger did allow events in which the both muons had CMU stubs.

The Level 1 system made no further requirements on the positions of the two muons stubs, except that they be located in noncontiguous modules. That is, at least one muon module lacking a muon stub must have resided between the two modules where muon stubs were observed. If this was not the case, then the two adjacent stubs were merged into a single muon stub for the purposes of the Level 1 trigger. The minimum p_T requirement on each stub in these two triggers was nominally 3.3 GeV/c.

4.2.2 Level 2

After the Level 1 trigger passed an event, the Level 2 trigger uses the information collected at Level 1 to decide if the event should go on to the Level 3 trigger. In a $p\overline{p}$ beam crossing for which the Level 1 trigger did not fire, a timing signal from the Tevatron announcing the occurrence of the next beam crossing would cause the stored signals in the detector to be cleared in preparation for the next crossing. If the Level 1 trigger did fire, then subsequent timing signals were inhibited for 20 μs, during which the Level 2 trigger made its decision. At the same time the Level 2 trigger was processing, up to five bunch crossings could occur. At an instantaneous luminosity of $\mathcal{L} = 5 \times 10^{30}\text{cm}^{-2}\text{s}^{-1}$, the typical Level 2 output rate was approximately 12 Hz[31].

The Level 2 trigger could perform simple tracking calculations to determine basic topological features of the event using the same calorimetry and muon signals used at Level 1 with greater sophistication at the expense of detector dead time.

High speed track pattern recognition was achieved in Level 2 with the central fast tracker (CFT), a hardware track finder that detected high-p_T charged particles in the CTC (Section 3.3.3). The CFT measured transverse momentum and azimuth (ϕ) since it only examined hits in the five axial superlayers of the CTC. For a given trajectory of an axial superlayer by a charged particle, the CFT considered two types of timing information: prompt and delayed hits. Prompt hits, which occurred within 80 ns after the beam crossing were due to short drift times caused by charged particles traversing the plane of the sense wires in a superlayer. Pairs of delayed hits, one on each side (in ϕ) of a given superlayer, that occurred 500 ns after the beam crossing were recorded. The absolute prompt and delayed drift times provide information on a track's trajectory, whereas the relative drift times yield measurements of curvature, and therefore p_T. After all the drift hits were recorded, the CFT attempted to construct tracks by first examining hits in the outermost superlayers. For each sense wire in the outer layer with a prompt hit, the CFT looked to the inner layers for "roads", or hit patterns, that matched patterns in a look-up table that had eight p_T bins and two ϕ bins, one for each sign of curvature. The p_T bins ranged from 3 to 30 GeV/c with a resolution of $\delta p_T/p_T \sim 0.035 \times p_T$, where p_T is in units of GeV/c.

The Level 2 trigger system organized the energy clusters from calorimetry, CFT tracks, and muon stubs into clusters called "physics objects". These included jets, photons, electrons, taus, muons, ΣE_T (total transverse energy) and neutrinos (whose signature is missing transverse energy). All of the dimuon selection triggers at Level 2 impose matching criterion between at least one of the two Level 1 muon stubs and a CFT track. Early in the data taking period, the requirement was that the stub and the extrapolated track have a separation in ϕ that 15° or less. This

was later tightened to $\Delta\phi \leq 5^\circ$ to reduce further the trigger rate due to accidental coincidences.

The Run 1A Level 2 trigger required one track to be found by the CFT whereas in Run 1B the Level 2 triggers required two CFT tracks. The various dimuon Level 2 triggers used in this analysis are listed in Appendix A along with their prerequisite Level 1 triggers.

4.2.3 Level 3

The Level 3 trigger[32] was a flexible, high-level, software based computer processor "farm" that could reconstruct several events in parallel. When the Level 2 trigger accepted an event, the channels in the CDF detector with valid data were digitized and read out by the data acquisition system and were then transported to the Level 3 processor farm. Over the course of Run 1, both the Level 3 trigger system and the data acquisition system underwent several significant changes. Although most of these changes took place between Run 1A and Run 1B, not all of them were implemented for physics data taking at the beginning of Run 1B.

For the purposes of analyses involving central muons, the Level 3 trigger reconstructed muon stubs and CTC tracks using algorithms that were largely identical to those employed in the off-line event reconstruction (refer to Section 4.6). However, since the three dimensional track reconstruction constituted most of the Level 3 execution time, only the faster of the two tracking algorithms used in the off-line code was utilized in the trigger.

Run 1A used only one dimuon trigger to form the data sample for the present analysis. It contained dimuon candidates from the decay $J/\psi \rightarrow \mu^+\mu^-$ which required two oppositely charged muon candidates with an invariant mass in the

range 2.8-3.4 GeV/c^2. The Run 1B trigger did not impose the opposite sign requirement and had an invariant mass window of 2.7-4.1 GeV/c^2.

In addition, the Level 3 dimuon triggers used in this study placed position matching requirements between the muon stubs and their associated CTC tracks. The algorithm extrapolated the CTC track to the appropriate muon subsystem and determined the difference in position between the projected track and the muon stub in both the r-ϕ plane and the z direction, correcting for energy loss and multiple scattering as a function of p_T. The Run 1A J/ψ tracks were required to match the muon stubs within four standard deviations of the combined multiple scattering and measurement uncertainties, whereas in Run 1B they were required to match within three standard deviations.

If an event was accepted by the Level 3 trigger, the data is then written to 8-mm tapes to be processed by the offline event reconstruction. The offline event reconstruction produced higher level physics objects from the low level detector output data structures. Since execution speed was less critical, the offline could make use of better calibration and alignment constants, more comprehensive run condition information, and more sophisticated tracking algorithms than were possible at Level 3. Once the offline was complete, the data was stored for future physics analysis.

4.3 Primary Vertex Selections

The primary vertex position, or point of origin, of the decay process under examination was crucial to this analysis. Primary vertex information was used in the calculation of the proper decay lengths. This section describes the process of measuring the positions of the vertices in a given event, and selecting a single vertex in events where more than one vertex was observed.

The transverse and longitudinal coordinates of the primary vertices were measured in two very different ways. The longitudinal coordinate (z) was established on an event-by-event basis using data from the VTX detector (refer to Section 3.3.2), where the vertex quality was determined on the basis of the number of VTX hits used to identify the vertex. As the measurement uncertainty calculated by the vertex-finding software was deemed to be unreliable due to the resolution of the VTX subsystem, a fixed uncertainty of $\sigma_z = 0.3$ cm was assumed for all events. The transverse coordinates, x and y, of the primary vertices in an event were typically calculated using the measured run-averaged beam position. The rationale for this was that the transverse beam position typically varied less than 10 μm in either the x or y directions over the course of a single data-taking run and that any event-by-event transverse coordinate measurements would be biased by the fluctuating track multiplicities and event topologies in individual events. The slopes and intercepts of the run-averaged beam position were therefore combined with the event-by-event z locations of the vertices in an event to determine the transverse positions of those vertices. The transverse coordinate measurement uncertainties were fixed to $(\sigma_x, \sigma_y) = (25,25)$ μm, corresponding to the observed circular beam spot size in the transverse plane.

During the latter stages of Run 1B, when the instantaneous luminosities often exceeded those in Run 1A by an order of magnitude, the primary vertex multiplicities also increased dramatically. Whereas in Run 1A the average number of high quality vertices in a given event was ~ 1.6 with $\sim 3\%$ of events having at least four such vertices, Run 1B events averaged ~ 2.9 high quality vertices with $\sim 5\%$ of events having at least eight such vertices. Once a pair of muon candidates had been identified, the z coordinates of the two candidates were used to select a single vertex. Specifically, of those vertices possessing the highest quality classification

for the given event, the vertex that had the shortest longitudinal displacement from either of the two muon candidates was chosen as the primary vertex corresponding to the muon objects. The position coordinates of muon candidates, as opposed to those of other tracks used in this analysis, were used to select primary vertices because the two muon candidate tracks constituted a well known and distinct part of the final state under study.

4.4 Track Quality Criteria

Track quality requirements were used to reduce the backgrounds arising from poor track measurements in the CDF detector. Track candidate fits reconstructed for this study were required to have used at least four hits in each of at least two axial superlayers of the CTC (refer to Section 3.4 for a description of the CTC). These track fits also had to use at least two hits in each of at least two stereo superlayers of the CTC. No requirement was made on which two of the five axial and four stereo superlayers were used in the fit.

Tracks possessing transverse momenta $p_T > 250$ MeV/c were reconstructed in the offline stage of the data reduction process. Useful measurement of tracks with $p_T < 250$ MeV/c would have been difficult due to the number of track helices whose radius of curvature is small enough so that the track loops inside the detector ("loopers") and the large number of hits available populating the inner superlayers of the CTC. As described in Appendix C, a study of the low p_T pattern recognition efficiency indicated that a requirement of $p_T > 800$ MeV/c (see Figure C.23) would ensure that candidate tracks would be in a p_T range with a relatively constant and measurable tracking efficiency. The p_T requirement imposed on candidate kaon tracks is 1.25 GeV/c and the muons are required to have a p_T of at least 1.8 GeV/c.

Tracks with high absolute pseudorapidity tended to have a reduced reconstructing efficiency because the track path would cross the CTC endplate before traversing enough layers to deposit the requisite number of the useful hits. Requiring the radii at which extrapolations of the track helices intersected one of the endplate planes of the CTC, R_{Exit}^{CTC}, was used to remedy the problem by diminishing the pseudorapidity acceptance. For example, a cut of $R_{Exit}^{CTC} > 132.0$ cm requires that the track traverses all nine superlayers of the CTC. However, a requirement of $R_{Exit}^{CTC} > 110$ cm, which corresponds to the track passing through the outer edge of superlayer six before crossing the end plate plane, defined a set of tracks with a high reconstruction efficiency while minimizing the reduction in geometric acceptance[33]. This requirement was imposed on the non-muon track candidates after multiple scattering and energy corrections had been applied. Muon candidates were not subject to an R_{Exit}^{CTC} cut as they are required to have a valid muon CMU stub which lies outside of the CTC volume.

In this study, information from the VTX and the CTC subsystems were employed in the reconstruction of track paths. The helical trajectories of the tracks were extrapolated back into the SVX where associated hits were sought using a road algorithm. If a sufficient number of good SVX hits were found, then the track was refit using all of the relevant VTX, CTC, and SVX information and the resulting track helix was used.

4.5 Muon Candidate Selection

The minimum transverse momentum required of a muon to traverse the central calorimeters and the solenoid magnet at $\eta \sim 0$ and reach the CMU subsystem was $\sim$1.4 GeV/c. For Run 1A, each muon had to have a minimum transverse momentum of 1.8 GeV/c with at least one muon of the pair having a $p_T > 2.8$ GeV/c. Run

1B required that each muon's transverse momentum be greater than 2.0 GeV/c for the TWO_CMU_TWO_CFT and the TWO_CMU_ONE_CFT_6TOW triggers whereas the TWO_CMU_CMX_TWO_CFT trigger had p_T criteria identical to the trigger used in Run 1A. Even though the low edge of these p_T requirements fell within inefficient regions of the measured Level 1 and Level 2 p_T dependent trigger efficiency distributions, imposing a higher requirement would have decreased the number of B^+ candidates and weakened the statistical significance of the measurement.

A major source of muon background was due to the charged kaons and pions decaying in flight to yield muons within the CDF tracking volume. In some cases, the charged kaon or pion tracks were reconstructed in the CTC, and the daughter muons registered stubs in the muon systems. A second major source of muon background was that due to hadronic "punch-through" particles, namely hadrons that passed through the calorimeters and entered the muon systems. An average of 5.4 pion interaction lengths lies between the CMU and $p\overline{p}$ collision region, resulting in approximately 1 in 220 high energy hadrons traversing the calorimeters undetected.

In order to reduce these backgrounds, a track candidate in the CTC, when extrapolated out to the muon chambers, was required to match the position of a muon stub. This condition was only met if the muon stub and the extrapolated CTC track is within three standard deviations of the multiple scattering and the measurement uncertainties in both the transverse (r-ϕ) and longitudinal (z) planes. This translates into matching cuts of $\chi^2(r-\phi) \leq 9.0$ and $\chi^2(z) \leq 12.0$.

Each muon is also required to have SVX information. This allows a more precise proper decay length measurement (see Section 4.7).

4.6 J/ψ Selection

$J/\psi \to \mu^+\mu^-$ candidates were formed by considering all the muon candidates in a given event that met the criteria outlined in the previous section. The two candidates constituting the muon pair were required to possess charges of opposite sign. A kinematical fit of the two muons is performed constraining the two tracks to originate from the same point in space. The resulting invariant mass is then required to satisfy the following condition:

$$\left| \frac{M_{\mu\mu} - M_{J/\psi}}{\delta_{\mu\mu}} \right| \leq 4.1 \tag{4.1}$$

where $M_{\mu\mu}$ is the invariant mass of the muon pair, $M_{J/\psi}$ is the world average J/ψ mass of 3.09688 GeV/c^2 [34], and $\delta_{\mu\mu}$ is the estimated mass error from the "vertex-constrained" kinematic fit. The choice of 4.1 will be discussed in the next chapter, but represents a 3.3σ cut on the fitted distribution.

The distribution of the J/ψ mass candidates that passed the selection requirements is shown in Figure 4.1. The J/ψ width varies as a function of p_T, so the mass distribution is non-Gaussian. Therefore, the mass distribution is fit with a sum of two Gaussians, plus a linear background. The number of J/ψ is 86829 $\pm$ 2113 over background with a mass of $M_{\mu\mu} = 3.0951 \pm 0.001$ GeV/c^2. The fitted widths of the two Gaussians are 13.2 ± 0.2 MeV/c^2 and 27.8 ± 0.5 MeV/c^2.

4.7 B^+ Meson Selection

After a sample of J/ψ candidates have been selected, the process of finding the remaining charged kaon to reconstruct the $B^\pm$ candidate begins. In this energy ranges, the CDF detector lacks the ability to differentiate kaon tracks from pion tracks, and, therefore all tracks passing the quality cuts are considered kaon candidates. As a consequence of this mass assignment, the combinatorial back-

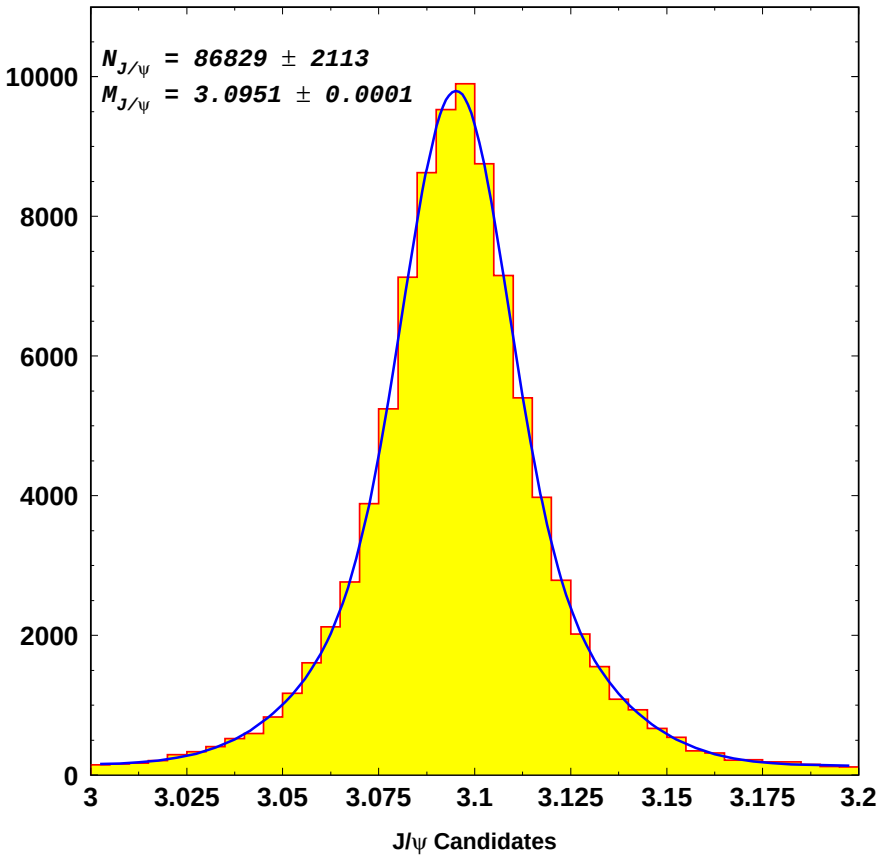

Fig. 4.1. J/ψ invariant mass distribution reconstructed from the dimuon decay channel.

ground could significantly degrade the signal to background ratio. Fortunately, the charged particle inclusive cross section in $p\overline{p}$ collisions is a rapidly falling function of transverse momentum[35]. Decay products from B^+ meson tend to have a higher p_T than the other unassociated tracks in the event, such as those from the underlying event, so imposing p_T cuts is an efficient method of enhancing the signal to background ratio. The kaon is required to have transverse momentum of 1.25 GeV/c or greater.

To form the $B^+ \to J/\psi\, K^+$ decay, the muons forming the J/ψ candidate and the kaon candidate are combined by kinematically fitting the three tracks. Two constraints are imposed in the fit. The first is that all three tracks originate from the same point in space and the second is that the dimuon invariant mass is required to be the world average J/ψ mass.

Once the fit is done, the decay vertex of the B^+ meson is required to be distinct from the primary vertex of the event to enhance the signal to background ratio. The signed proper decay length in the B^+ rest frame is defined as

$$ct(B) = \frac{\overrightarrow{X_{J/\psi}} \cdot \overrightarrow{p_T^B}}{p_T^B} \cdot \frac{1}{(\beta\gamma)^B} = \frac{M_B \overrightarrow{X_{J/\psi}} \cdot \overrightarrow{p_T^B}}{(p_T^B)^2} \tag{4.2}$$

where

$$\overrightarrow{X_{J/\psi}} = (x_{J/psi} - x_{PV})\hat{i} + (y_{J/\psi} - y_{PV})\hat{j} \tag{4.3}$$

and $(\beta\gamma)^B$ is the relativistic boost of the B^+ meson. The $(x_{J/\psi}, y_{J/\psi})$ are the x and y coordinates of the J/ψ decay vertex and the (x_{PV}, y_{PV}) are the transverse coordinates of the primary vertex associated with the two muons (see Section 4.3). This definition utilizes the transverse momentum of all three tracks while the position information of only the J/ψ decay vertex (two muon tracks) is used under the assumption that, since the J/ψ decays electromagnetically, it is the same as

the B^+ meson decay vertex. This method has the advantage of utilizing the better precision of the SVX, since the muons are required to have SVX information.

The proper decay length is required to be greater than 100 μm. In addition, the transverse momentum of each B candidate is required to be greater than 6.0 GeV/c, which is the Monte Carlo prediction for the minimum B^+ momentum necessary to produce the decay products which pass all the other selection cuts. The following list summarizes the selection cuts:

- Minimal quality cuts on the tracks:
  - $\geq$ 2 axial layers with at least 4 used hits
  - $\geq$ 2 stereo layers with at least 2 used hits
- Require SVX information
  - Number of found hits ≥ 3
- ($p_T(\mu_1 \text{ and } \mu_2) \geq 2.0$) GeV/$c$ or ($p_T(\mu_1 \text{ and } \mu 2) \geq 1.8$ GeV/c and $p_T(\mu_1 \text{ or } \mu_2) \geq 2.8$ GeV/c)
- Muon matching $\chi^2(r\text{-}\phi) \leq 9.0$
- Muon matching $\chi^2(z) \leq 12.0$
- $|M_{\mu\mu} - M_{J/\psi}| \leq 4.1\sigma$
- $|Z_{vertex}| \leq 60.0$ cm
- All events pass DIMUTG
- $p_T(K^{\pm}) \geq 1.25$ GeV/c
- $p_T(B) \geq 6.0$ GeV/c
- $ct \geq 100$ μm
- $R_{Exit}(K^+) \geq 110.0$ cm

Figure 4.2 shows the B^+ invariant mass distribution after all the selection requirements have been applied. The distribution is fit with a Gaussian signal function plus a linear background using a unbinned maximum likelihood method. See Section 6.1 for a detailed description of the fit procedure. The region below 5.15 GeV/c^2 has been excluded from the fit to prevent overestimating the combinatorial background under the B^+ mass peak. Some $B^+ \to J/\psi\, K^+$ candidates could be incompletely reconstructed $B^0 \to J/\psi\, K^{*0}$ decays, and with perfect mass resolution the invariant mass formed for these partially reconstructed B^0 mesons

would lie at least one pion mass (140 MeV/c^2) below the B^+ mass. The fit results in 387 ± 32 B^+ candidates over background.

4.8 Background Checks

Two similar decay modes that could possibly contribute to the signal region of the $B^+ \to J/\psi\, K^+$ invariant mass distribution are $B^+ \to J/\Psi\pi^+$ and $B^+ \to \chi_{c1}(1p)K^+$ where $\chi_{c1}(1p) \to J/\Psi\gamma$. For the former decay mode, the pion track is reconstructed as a kaon and the resulting invariant mass is shifted higher than the B^+ mass due to the wrong mass assignment. Figure 4.3 shows the invariant mass distribution of Monte Carlo $B^+ \to J/\Psi\pi^+$ events reconstructed as $B^+ \to J/\psi\, K^+$. The ratio of branching ratios relative the $B^+ \to J/\psi\, K^+$ is[34]

$$\frac{\mathcal{B}(B^+ \to J/\Psi\pi^+)}{\mathcal{B}(B^+ \to J/\Psi K^+)} = 0.051 \pm 0.014. \tag{4.4}$$

Using the measured number of $B^+ \to J/\psi\, K^+$ signal events (387 ± 32) and the ratio of branching ratios, the expected number of $B^+ \to J/\Psi\pi^+$ events to contribute is 20 ± 6. Since the statistical error of the $B^+ \to J/\psi\, K^+$ events is larger than the expected number of $B^+ \to J/\Psi\pi^+$ events, the potential background is considered to have a negligible contribution.

For the $B^+ \to \chi_{c1}(1p)K^+$ decay mode, only the J/ψ and the kaon will be reconstructed. The invariant mass of the partially reconstructed decay falls below the fitting range of the mass distribution and therefore does not contribute any significant background to the B^+ signal region. Figure 4.4 shows the invariant mass distribution when the $B^+ \to \chi_{c1}(1p)K^+$ decay is reconstructed as a $B^+ \to J/\psi\, K^+$ event in Monte Carlo.

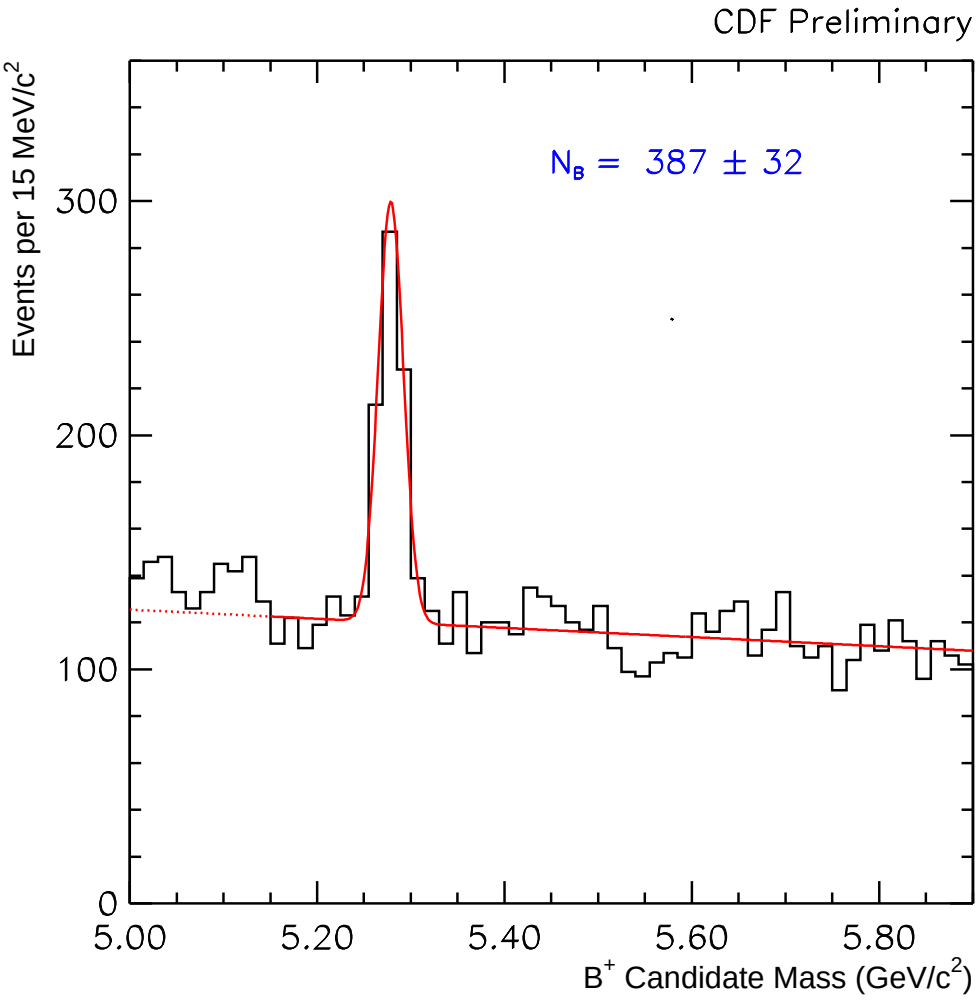

Fig. 4.2. B^+ invariant mass distribution reconstructed from the decay $B^+ \to J/\psi\, K^+$.

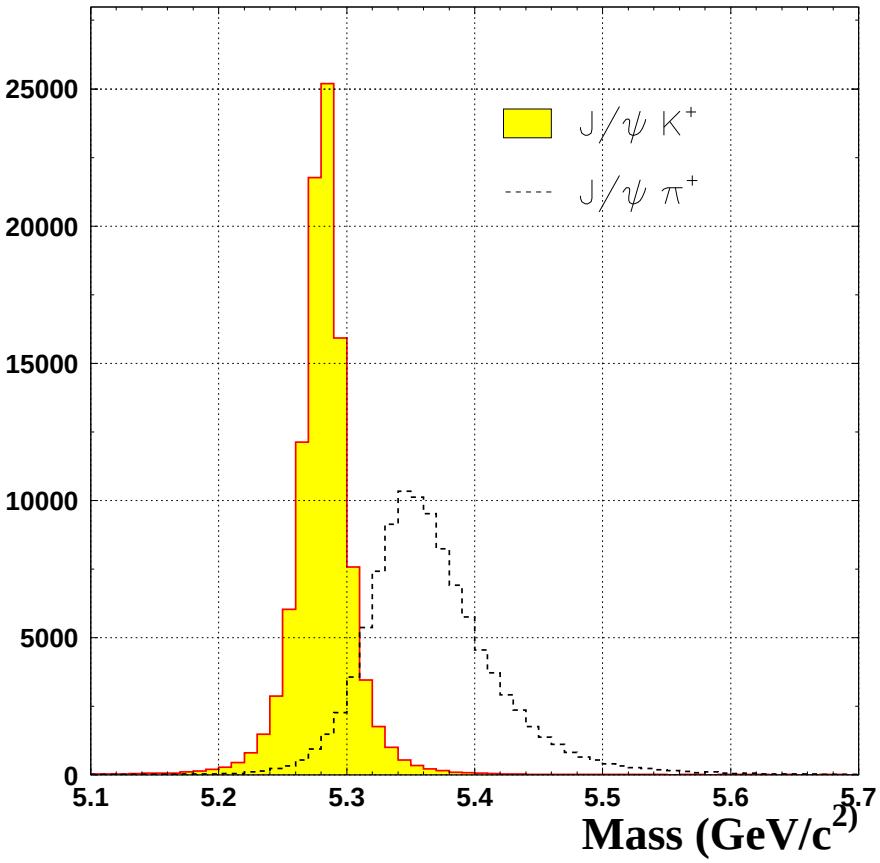

Fig. 4.3. Monte Carlo $B^+ \to J/\psi\pi^+$ (dashed line) events reconstructed as $B^+ \to J/\psi\, K^+$ candidates (solid histogram).

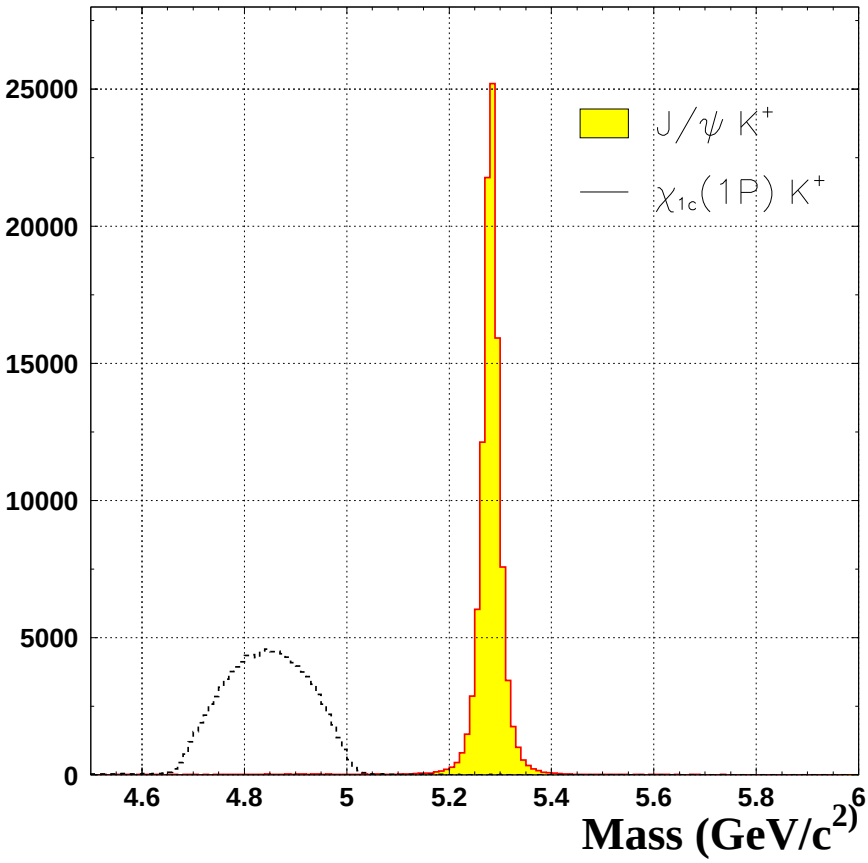

Fig. 4.4. Monte Carlo $B^+ \to \chi_{1c}(1P)K^+$ events (dashed line) reconstructed as $B^+ \to J/\psi\, K^+$ candidates (solid histogram).

5. DETECTOR ACCEPTANCE AND RECONSTRUCTION EFFICIENCY

Since this cross section analysis is a measurement of an absolute rate at which the B^+ meson is produced, it is essential to know the proportion of candidates that go unobserved due to both the fiducial detector geometry and the kinematic selection criteria. Measurements of the geometrical acceptance of the detector and reconstruction efficiencies are used to determine the total number of B^+ mesons produced. This chapter describes the methods of determining the detector acceptance and the reconstruction and selection efficiencies using a Monte Carlo event generator in conjunction with detector and trigger simulators. The first section (Section 5.1) explains the efficiencies that required Monte Carlo simulations and Section 5.2 details the efficiencies that were measured with data.

5.1 Geometric and Kinematic Acceptance

5.1.1 Monte Carlo Event Generator

To produce the B^+ decays, single b quarks were generated according to an inclusive transverse momentum spectrum based on a next-to-leading order QCD calculation [1] that used the Martin-Roberts-Stirling MRST parton distribution or structure functions [36]. The renormalization scale was set to $\mu = \mu_0 \equiv \sqrt{(m_b^2 + p_T^2(b))}$ and a b quark mass of $m_b = 4.75$ GeV/c^2. The b quarks were produced in the rapidity range $-1.1 < y_b < 1.1$ with $p_T(b) \geq 5.5$ GeV/c and fragmented into B^+

mesons according to a model that used the Peterson fragmentation function [15] with the Peterson parameter set to, $\epsilon_b = 0.006$ [16].

5.1.2 Monte Carlo Decay of B^+ Mesons

Decays of Monte Carlo generated B^+ mesons into the J/ψ and the kaon final states were performed using a modified version of the CLEO QQ Monte Carlo program[37]. Properties of the relevant particles, including mass, lifetime, and intrinsic width, were updated in the program to reflect the current world average values[34]. In the $B^+ \rightarrow J/\psi K^+$ decay, since the B^+ and the kaon are pseudo-scalar particles, the J/ψ particle is purely longitudinally polarized which is accounted for in the QQ package.

5.1.3 Detector Simulation

Once the Monte Carlo B^+ mesons were generated and decayed into their final state, a full Monte Carlo simulation of the CDF detector, called QFL, was utilized. QFL propagates the particles through the magnetic field and uses the known resolutions of each detector component to smear out the measured track helix parameters. It also incorporates the geometrical distribution of matter in the detector to simulate multiple Coulomb scattering and energy lost by particles as they pass through matter.

The simulation produced raw data structures that were in most cases identical to those read out from the actual detector during data taking runs. This allowed the subsequent processing of the Monte Carlo events to be identical to that used for the actual data.

As discussed in Section 4.1, the CDF detector geometry changed between Runs 1A and 1B as well as the location and distribution of the material due to cabling

and support structures. To account for theses differences, full simulations for both portions of the run were performed and the acceptances were averaged, weighted by integrated luminosity.

5.1.4 Trigger Simulation

Since the muons in the data sample used for this analysis were required to pass the J/ψ Level 1 and Level 2 triggers, a simulation of the triggers has been included in the acceptance calculation. This simulation randomly accepts muon candidates with a probability determined by the trigger efficiencies. For the Run 1A simulation, the module MU2TRG was used while DIMUTG module[38] was used for Run 1B simulation. The main difference being that the Run 1A triggers used one muon to trigger an event whereas the Run 1B triggers required that two muons to pass the trigger requirements. Each module used parameterizations of the measured muon trigger efficiencies to determine the probability that a given candidate satisfied the requirements.

5.1.4.1 Run 1A Trigger Efficiencies

The Level 1 trigger efficiencies for Run 1A was determined by analyzing a data sample containing events that passed a single muon trigger. Some of these events also contained a second muon. The invariant mass of the trigger muon and any other muon was formed. Using the invariant mass distribution, the J/ψ candidates were identified and the second (non-trigger) muon leg was considered to be a good muon candidate. Since the second muon was not required to pass the Level 1 trigger, it could be used to provide an unbiased estimate of the trigger efficiency. The fraction of non-trigger J/ψ muon legs that passed Level 1 was calculated as a function of the muon transverse momentum.

The Level 2 trigger efficiency is simply a measure of the CFT tracking efficiency (refer to Section 4.2.2) which is determined by the roads that have been defined for the CFT pattern recognition algorithm. The efficiency was determined using the Run 1A J/ψ data set. For all J/ψ candidates, one muon leg which had an associated CFT track (which meant that it passed the Level 2 trigger) was identified. Then the fraction of second legs which also have an associated CFT track was determined as a function of the muon transverse momentum.

5.1.4.2 Run 1B Trigger Efficiencies

The Run 1B Level 1 muon trigger is fundamentally the same as the Run 1A Level 1 trigger. Therefore, the Level 1 efficiency used in Run 1A is applied to Run 1B.

Unlike the Level 1 trigger, the Level 2 trigger was changed dramatically between Run 1A and Run 1B. In Run 1A a dimuon pair could pass the trigger as long as one of the muons had an associated CFT track. For Run 1B, both muons had to have an associated CFT track and a CMU stub that passed the Level 1 trigger. The data sample used to measure the Level 2 dimuon trigger efficiency consist of J/ψ events where both muons are required to pass the Level 1 trigger and one muon is required to pass a single CFT track Level 2 trigger. The muons that were not responsible for triggering the Level 2 trigger made up an unbiased sample used to measure the Level 2 dimuon trigger efficiency.

5.1.5 Combined Geometrical Acceptance and Trigger Efficiency

The events were processed by the same analysis code used on the data to estimate the combined acceptance and trigger efficiency. The products of these quantities are listed in Table 5.1.

Table 5.1. The product of the trigger efficiency and the acceptance in the p_T bins for Run 1A, Run 1B and the integrated luminosity weighted average for Run 1.

p_T Range	$\langle p_T \rangle$	Trigger Efficiency×Acceptance (%)		
(GeV/c)	(GeV/c)	Run 1A	Run 1B	Run 1
6 - 9	7.34	2.01±0.02	1.61±0.02	1.70±0.03
9 - 12	10.35	5.29±0.05	4.20±0.04	4.44±0.06
12 - 15	13.36	8.36±0.10	6.53±0.09	6.93±0.13
15 - 25	18.87	11.96±0.14	9.26±0.12	9.57±0.11

Figure 5.1 shows the geometric and kinematic acceptance for Runs 1A and 1B data as a function of the B^+ transverse momentum. The acceptance is plotted at the mean p_T, $\langle p_T \rangle$, in each of the ranges shown in Table 5.1. The calculation of the $\langle p_T \rangle$ is presented in Appendix B.

The selection criteria used to define the geometric and kinematic acceptance are listed below:

- Minimal quality cuts on the tracks:
  - ≥ 2 axial layers with at least 4 used hits
  - ≥ 2 stereo layers with at least 2 used hits
- ($p_T(\mu_1 \text{ and } \mu_2) \geq 2.0$) GeV/$c$ or ($p_T(\mu_1 \text{ and } \mu_2) \geq 1.8$ GeV/c and $p_T(\mu_1 \text{ or } \mu_2) \geq 2.8$ GeV/c)
- $|M_{\mu\mu} - M_{J/\psi}| \leq 4.1\sigma$
- $p_T(K^{\pm}) \geq 1.25$ GeV/c
- $p_T(B) \geq 6.0$ GeV/c
- $R_{Exit}(K^+) \geq 110.0$ cm

The Run 1B acceptance is slightly higher than the acceptance in Run 1A because the muon pair can have one of two p_T combinations. That is, for the Run 1B

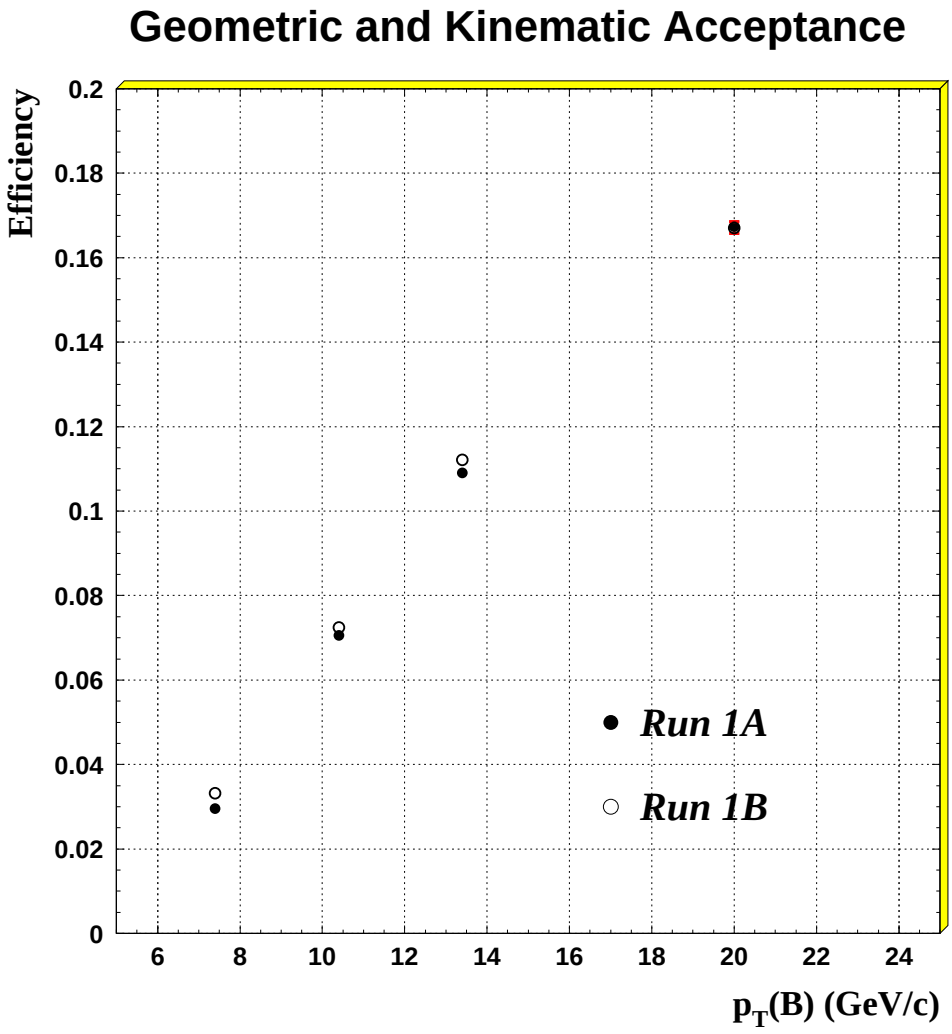

Fig. 5.1. Geometric and kinematic acceptance as a function B^+ meson p_T.

acceptance, the two muons can have a transverse momentum combination where each muon has a p_T greater than 2.0 GeV/c or the combination where each muon has a p_T greater than 1.8 GeV/c with one muon's p_T greater than 2.8 GeV/c. Whereas for Run 1A, only the latter combination is utilized.

Figure 5.2 shows the trigger efficiency for each portion of Run 1 as a function of the B^+ transverse momentum. The trigger efficiency for Run 1A is $\sim 20\%$ higher than Run 1B. Two effects contribute to this difference. One is the requirement of two CFT tracks (refer to Section 4.2.2) in Run 1B which lowers the trigger efficiency by $\sim 15\%$ relative to Run 1A. Run 1A only requires that one track be found by the CFT. The other is a $\sim 10\%$ difference in trigger acceptance.

5.2 Efficiencies of the Offline Selection Requirements

The detector acceptance and trigger efficiencies described in the previous section did not include all of the criteria for selecting a B^+ candidate. This section presents the efficiency of the offline selection requirements and a description of the efficiency calculation.

5.2.1 Muon Matching Requirements

Muons forming the J/ψ candidates were required to pass selection cuts based on the χ^2 of the match between the intercept of the muon chamber track segment and the CTC track in both the r-ϕ and z directions. The matching cuts applied are $\chi^2(r\text{-}\phi) \leq 9.0$ and $\chi^2(z) \leq 12.0$. The efficiency of these cuts was determined from a sample of J/ψ candidate events containing muons which were only required to pass the looser Level 3 matching requirements of $\chi^2(r-\phi) \leq 16.0$ and $\chi^2(z) \leq 16.0$. In each event, a muon was randomly chosen, and if it passed the matching cuts, the invariant mass of the dimuon pair was calculated. The efficiency of the cuts

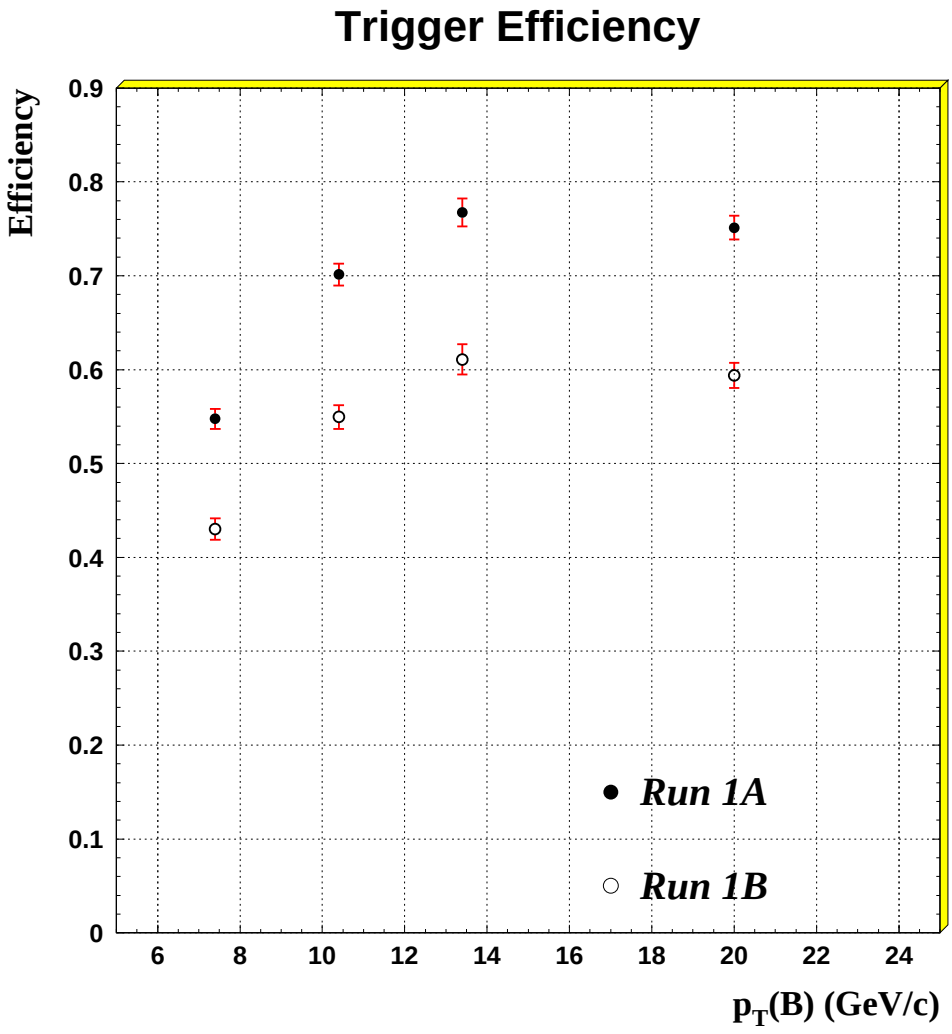

Fig. 5.2. Trigger efficiencies for Run 1A and Run 1B as a function of the $p_T(B^+)$.

was found by dividing the number of J/ψ for which the second muon leg passed the cuts by the number of J/ψ for which at least the first leg passed the cuts. The efficiency of requiring both J/ψ muons to pass the cuts is then the product of the efficiency for each muon to pass the cuts, and was determined to be $98.7 \pm 0.2\%$ [39]. The uncertainty is due to the statistical error on the fits to the J/ψ invariant mass distributions.

5.2.2 SVX Fraction

Since both muons from the J/ψ are required to have been reconstructed in the SVX (refer to Section 3.3.1), the fraction of events that are not observed in the SVX needs to be known. The efficiency of this requirement was measured using the same J/ψ data set that is used the measure the B^+ cross section since $\sim 20\%$ of the events are produced from B mesons; the other $\sim 80\%$ originate from the primary vertex called prompt events. The muons contained in this sample have either been reconstructed by the CTC or have been reconstructed by the CTC and the SVX.

The SVX fraction is measured by counting the number of J/ψ's with SVX information and dividing by the number of J/ψ's that have only been reconstructed in the CTC. The SVX fraction is $52.35 \pm 0.55\%$ for Run 1A and $56.33 \pm 0.23\%$ for Run 1B. The fraction for Run 1B is larger than Run 1A because the inner layer of the SVX was moved in closer to the beam line to eliminate the small separation between the first layer silicon wafers present in Run 1A (see Section 3.3.1.) The uncertainty is due to the statistical error on the fits to the J/ψ invariant mass distributions.

5.2.3 J/ψ Normalized Mass Cut

The J/ψ normalized mass cut is used to reduce the combinatorial background by selecting muon pairs that are very likely to be a J/ψ. Figure 5.3 shows the normalized J/ψ mass distribution, as defined by Equation (4.1), for Run 1A, Run 1B, and the entire Run 1 data set. The mass window cut was chosen to be $\pm 3.3\hat{\sigma}$ where $\hat{\sigma}$ is taken from the width of the Gaussian fitted Run 1B normalized mass distribution. Given this choice, the efficiency of the mass window cut is the fraction of the area of the Gaussian lying within the mass window, which is 99.9%. Ideally, if the error on the mass determination were correctly estimated, the width of the normalized J/ψ mass would be 1. The fact that these widths are greater than 1 indicate that some of the tracking parameter errors are underestimated.

5.2.4 ct Cut Efficiency

The efficiency of requiring the B^+ mesons to have a proper decay length, defined by Equation (4.2), to be greater than 100 μm was determined using Monte Carlo generated events and the lifetime resolution measured in the J/ψ data set. The Monte Carlo events were generated and decayed using the same method to calculate the acceptance described in Sections 5.1.1 and 5.1.2, but the lifetime resolution was obtained from data.

The data used to measure the lifetime resolution was the background events obtained from the sidebands (5.20-5.25 GeV/c^2 and 5.35-5.40 GeV/c^2) of the B^+ invariant mass distribution. These events were chosen since the majority of them would have a lifetime consistent with zero. The lifetime distributions were fit with Gaussian function for the prompt (central) peak and exponential function for each side of the central peak. Figure 5.4 shows the fit to the distributions in the four $p_T(B^+)$ ranges and the corresponding lifetime resolution which is determined

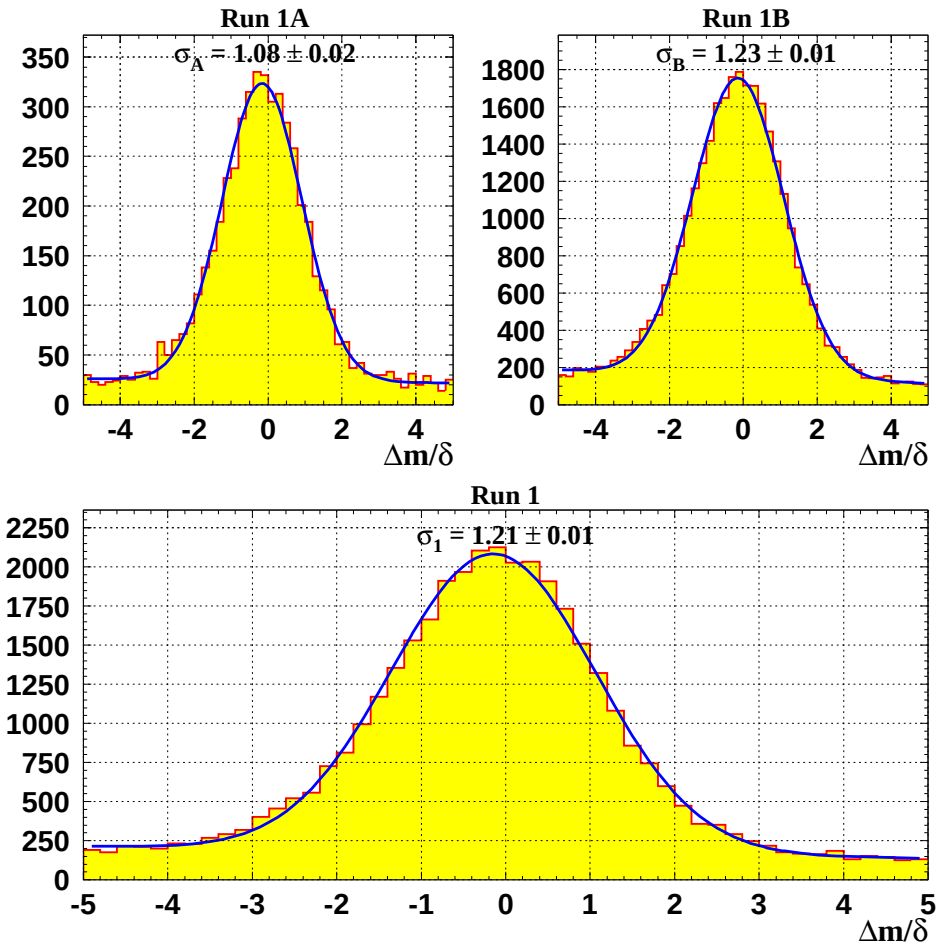

Fig. 5.3. Normalized mass for the J/ψ candidates.

by the width of the central Gaussian. Figure 5.5 shows the resolutions for Run 1A and Run 1B. Since the difference between the two runs is much smaller than the difference between the lowest and highest p_T ranges, th ct cut efficiency was measured as a function of the B^+ transverse momentum.

The Monte Carlo generated lifetime was smeared using a Gaussian resolution function with a width that was measured in the data for each p_T range. The efficiency is then the fraction of events that pass the 100 μm ct cut. Table 5.2.4 lists the efficiencies in each p_T range. The systematic error on the efficiency were obtained by varying the resolution of the Gaussian by $\pm\sigma$.

Table 5.2. ct cut efficiencies in each of the four p_T bins.

p_T Range GeV/c	$\langle p_T \rangle$	ct Efficiency
6 - 9	7.34	$78.3 \pm 0.2\%$
9 - 12	10.35	$78.9 \pm 0.4\%$
12 - 15	13.36	$78.5 \pm 0.5\%$
15 - 25	18.87	$78.0 \pm 0.3\%$

Since the efficiency showed virtually no variation with the B^+ transverse momentum even though the resolution doubled from the lowest to the highest p_T bin, the average of the four values was determined and the largest error was taken as the error on the calculated average; $78.4 \pm 0.5\%$.

5.2.5 Tracking Efficiencies

One drawback of the QFL detector simulation is that it is perfectly efficient at reconstructing any particle tracks that are contained within the detector volume.

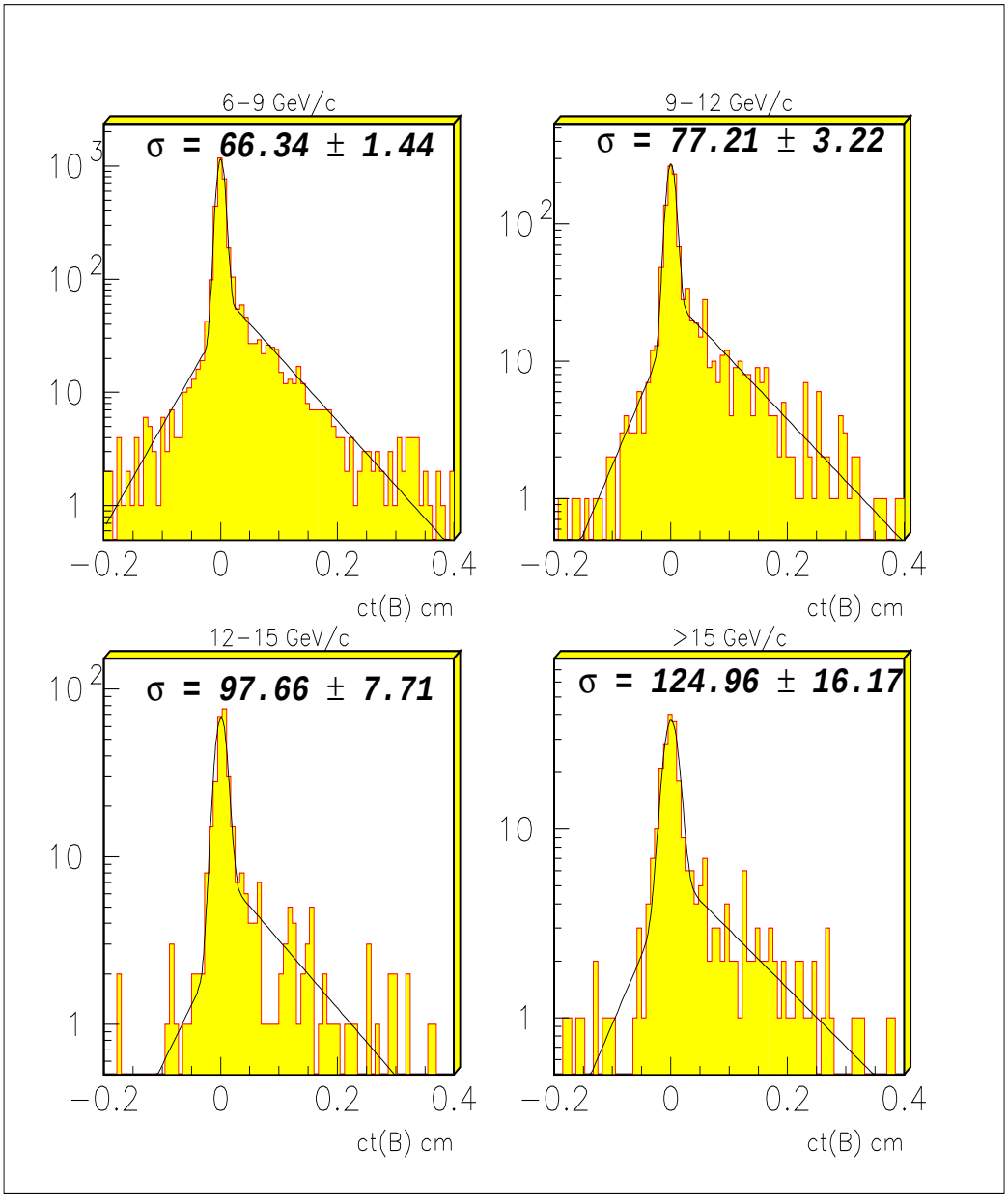

Fig. 5.4. The lifetime distribution of the $B+$ background events in p_T ranges: 6-9. 9-12, 12-15, and > 15 GeV/c.

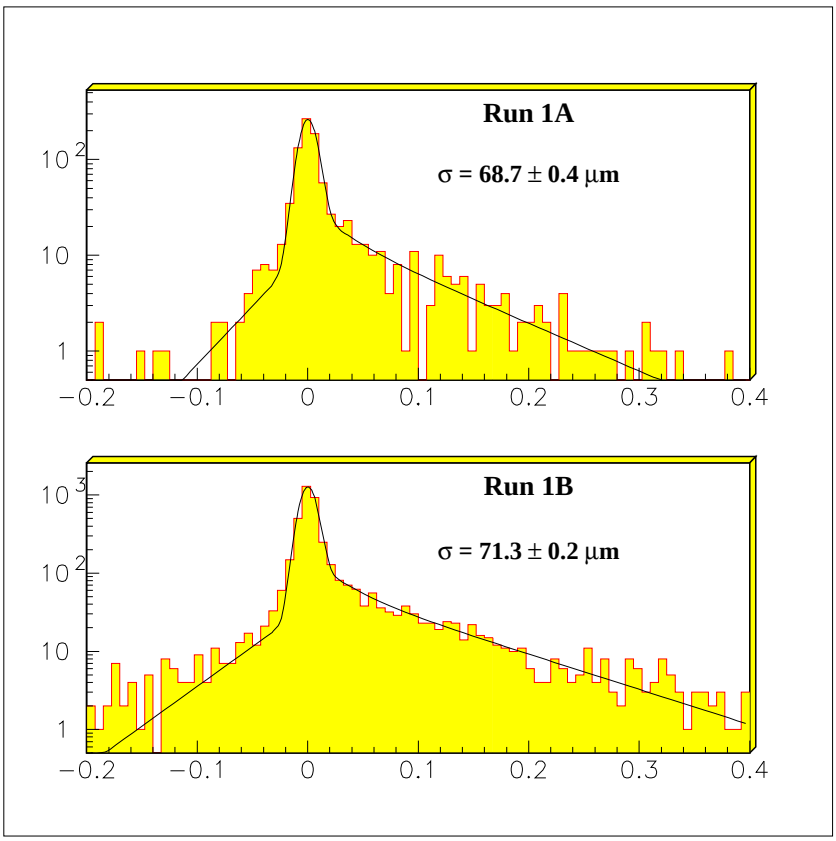

Fig. 5.5. The lifetime distribution of the $B+$ background events for Run 1A and Run 1B.

Since the CDF detector is not perfectly efficient at reconstructing tracks, it is necessary to apply an additional correction for this.

There are two components that comprise the tracking efficiencies. The first part is the efficiency of the tracking that is done in the Level 3 trigger system. Inefficiencies in the tracking of the muons at this stage can cause the event to be rejected from the data sample. Once an event has been accepted at Level 3, one must account for the offline CTC track reconstruction efficiency. This stage may improve the track quality or find new tracks that were missed at Level 3.

5.2.5.1 Level 3 Online Tracking Efficiency

The Level 3 online tracking efficiency was determined using a special data set in which all events that pass the Level 2 triggers were written out. The efficiency is therefore the fraction of events that were identified by the Level 3 trigger and was measured to be $97 \pm 2\%$.

During Run 1A, there was a portion of the data taking that suffered from the start time of each event being incorrectly determined, referred to as "bad T0" runs. The net effect of these runs was an extra inefficiency in reconstruction at Level 3 and was determined to be $\sim 4\%$[40]. The Level 3 efficiency used for Run 1A is $93.1 \pm 2.0\%$.

5.2.5.2 CTC Offline Tracking Efficiency

Since the Level 3 online tracking is a simplified version of the track reconstruction that is done offline, it is assumed that all muons identified by Level 3 can be reconstructed offline. However, it is still necessary to correct for the track finding efficiency for the kaon track. A detailed study[41] of the CTC track reconstruction efficiencies was conducted. To measure the efficiency, a Monte Carlo generated

kaon track was "embedded" in a displaced J/ψ event. The angle of the kaon direction with respect to the J/ψ direction and the momentum were adjusted so that the vector sum of each particle's four momentum created a B^+ meson. This was done for $\sim 42,000$ events. The events were reconstructed and the fraction of events where the kaon was successfully found is the CTC track reconstruction efficiency. Appendix C summarizes the methodology and results of the track reconstruction efficiency measurements. The single track reconstruction efficiency was measured to be $99.6 \pm 0.9\%$ for a track with $p_T > 0.8$ GeV/c and with $R_{Exit}^{CTC} > 130$ cm.

5.2.6 Run 1B Luminosity Correction

It was observed that the upsilon ($\Upsilon(1S)$, $\Upsilon(2S)$, $\Upsilon(3S)$) production cross section[42] decreased over the course of Run 1B. This was corroborated by a similar decrease in the J/ψ yield. Since it was found that the track reconstruction efficiency was constant throughout Run 1b, and no other detector effects showed a similar decrease, a correction factor for the integrated luminosity was measured in the J/ψ data set. The correction was derived by plotting the J/ψ yield as a function of instantaneous luminosity. The cross section drops linearly with increasing instantaneous luminosity. By fitting the decrease with a line, a correction for the J/ψ yield was determined to be $12 \pm 4\%$[43].

5.2.7 Summary of the Reconstruction Efficiencies

The reconstruction efficiencies are summarized in Table 5.2.7. For the B^+ candidates decaying to particles completely contained within the detector acceptance, the reconstruction efficiency is $36.8 \pm 1.1\%$.

Table 5.3. Summary of reconstruction efficiencies for the B^+ meson. The efficiencies that are not common between 1A and 1B are combined using an integrated luminosity weighted average. The error on each efficiency is absolute.

Source	Efficiency	
	Run1A (%)	Run1B (%)
CTC Tracking	$(98.9 \pm 1.5)^3$ $= 96.7 \pm 2.6$	$(99.6 \pm 0.9)^3$ $= 98.8 \pm 1.6$
CTC-μ Linking	$(99.8 \pm 0.2)^2$ $= 99.6 \pm 0.3$	
Muon Chamber Efficiency	$(98.0 \pm 1.0)^2$ $= 96.0 \pm 1.4$	
μ Matching Cut	98.7 ± 1.0	
Z Vertex Cut	95.3 ± 1.05	93.7 ± 1.1
L3 μ Tracking	93 ± 2	97 ± 2
ct Cut	78.4 ± 0.5	
SVX Fraction	52.35 ± 0.55	56.33 ± 0.23
Total	36.8 ± 1.1	

6. CROSS SECTION CALCULATION AND MEASUREMENT

Using the J/ψ data set and the selection criteria described in Chapter 4, a B^+ data sample was produced in which the inefficiencies were well understood and the systematic uncertainties were minimized. Once the B^+ candidates have been selected and the reconstruction efficiencies and detector acceptance have been determined, the differential cross section and the total cross section can be calculated. This chapter presents the cross section calculations and the results.

6.1 Differential Cross Section

To measure the B^+ meson differential cross section as a function of p_T, the invariant mass distribution is divided into four p_T ranges: 6-9, 9-12, 12-15, and 15-25 GeV/c. Figure 6.1 shows the mass distribution for each p_T range. The number of B^+ candidates was determined using an unbinned maximum likelihood fit to a Gaussian signal function plus linear background. The likelihood function used is:

$$\mathcal{L} = f_{sig} + f_{back} \tag{6.1}$$

where

$$f_{sig} = \frac{N_{signal}}{N_{total}\sqrt{2\pi}s\sigma_i} e^{-\frac{1}{2}\left(\frac{M_i - M}{s\sigma_i}\right)^2} \tag{6.2}$$

and

$$f_{back} = \frac{1 - N_{signal}}{N_{total}} m\left(M_i - \frac{w}{2}\right) + \frac{1}{w} \tag{6.3}$$

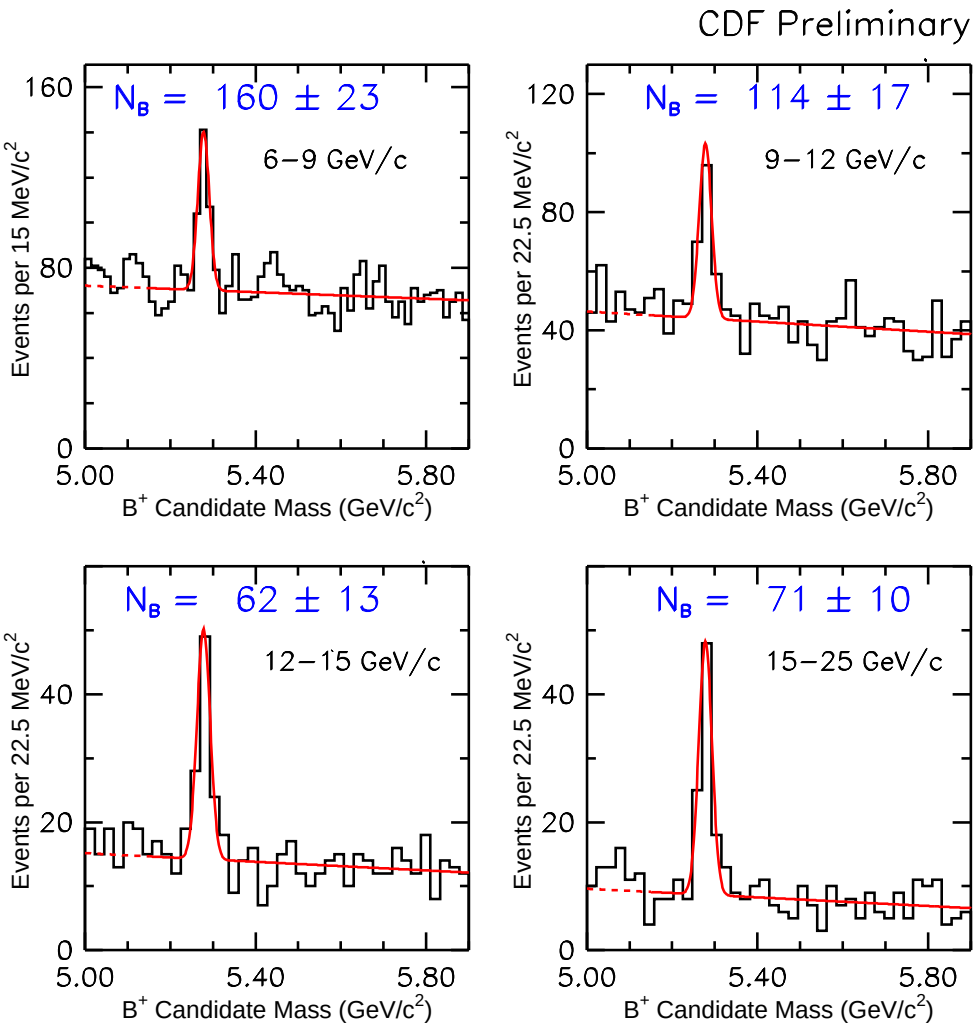

Fig. 6.1. B^+ candidate mass distribution for the four p_T ranges. The overlayed curve is for illustration only.

The definitions of the parameters used in the likelihood function are as follows:

N_{signal}	=	the number of signal events
N_{total}	=	the total number of signal + background events
M	=	the fitted mass of the Gaussian signal distribution
M_i	=	the mass of the i^{th} B^+ candidate
σ_i	=	the error on M_i
s	=	the mass error scale factor for σ_i
m	=	slope of the background
w	=	the mass range in which the fit is performed

The calculated mass of each B^+ candidate, M_i, is obtained from a kinematic fit of the two muon and kaon tracks. As discussed in Section 4.7, the three tracks are required to originate from the same point in space and the dimuon invariant mass is constrained to the world average J/ψ mass. The resulting error of the kinematic fit of the invariant mass is σ_i and relies on the track parameter covariance matrix of each track. The parameter M is the B^+ mass of the Gaussian signal distribution returned by the fit of the total data sample. The mass error scale factor, s, is required to increase the error of the B^+ mass since the errors of the track parameters are underestimated (see Section 5.2.3).

The mass region used in the fit is from 5.15 to 6.00 GeV/c^2 where the extended range above the B^+ mass is utilized to obtain a better estimation of the slope of the background. The region below 5.15 GeV/c^2 is excluded to avoid overestimating the combinatoric background under the B^+ peak since some of the $B^+ \to J/\psi\, K^+$

candidates could be incompletely reconstructed $B^0 \to J/\psi K^{*0}$ decays. The invariant mass of these partially reconstructed B^0 mesons would lie about one pion mass (140 MeV/c^2) below the B^+ mass.

The differential cross section $d\sigma/dp_T$ is calculated with the following equation:

$$\frac{d\sigma(B^+)}{dp_T} = \frac{N^i_{Signal}/2}{\Delta p_T \cdot L \cdot A_i \cdot \epsilon \cdot \mathcal{B}} \tag{6.4}$$

where N_{Signal} is the number of B^+ mesons determined from the likelihood fit of the B^+ candidate mass distribution in each p_T range. The factor of 1/2 is included because both B^+ (contains a $\overline{b}$ quark) and B^- (contains a b quark) mesons are detected, while the cross section is quoted for only one species of b quark. The width of the p_T bin is Δp_T, A is the Monte Carlo acceptance which includes the kinematic and trigger efficiencies, and ϵ is the additional reconstruction efficiency not included in the simulation (see Table 5.2.7). Due to the elimination of runs in which detector hardware operations were marginal and the use of select triggers, the Run 1B integrated luminosity utilized was (78.5 $\pm$ 3.2) pb^{-1}. The Run 1A integrated luminosity remained the same and therefore the total integrated luminosity for Run 1 cross section calculation is (98.1 $\pm$ 4.0) pb^{-1}. The branching ratios [34] are

$$\mathcal{B}(B^\pm \to J/\psi K^\pm) = (9.9 \pm 1.0) \times 10^{-4} \tag{6.5}$$

$$\mathcal{B}(J/\psi \to \mu^+\mu^-) = (6.01 \pm 0.19) \times 10^{-2} \tag{6.6}$$

Table 6.1 lists the cross section for each p_T bin. The error on the number of events in the "Events" column of Table 6.1 is statistical only. The three errors quoted on the cross section are statistical *(stat)*, uncorrelated *(sys_{uc})*, and fully correlated *(sys_{fc})*, respectively.

Table 6.1. B^+ meson differential cross section from the Run 1B data.

$\langle p_T \rangle$ GeV/c	Events	Acceptance (%)	Cross Section (nb/GeV/c)
7.34	160 ± 23	1.70 ± 0.01	816 ± 118 $(stat)$± 29 (sys_{uc})± 107 (sys_{fc})
10.35	114 ± 17	4.44 ± 0.01	221 ± 32 $(stat)$± 8 (sys_{uc})± 29 (sys_{fc})
13.36	62 ± 13	6.93 ± 0.02	76.7 ± 15.7$(stat)$± 2.2(sys_{uc})± 10.0(sys_{fc})
18.87	71 ± 11	9.86 ± 0.04	18.8 ± 2.6$(stat)$± 0.5(sys_{uc})± 2.5(sys_{fc})

6.2 Systematic Uncertainties

The systematic errors have been divided into two classes: uncorrelated uncertainties that change from one p_T bin to the next (sys_{uc}), and the fully correlated errors that are independent of p_T (sys_{fc}). The variation of the Peterson parameter, the QCD renormalization scale, and the trigger efficiency all change the shape of the Monte Carlo $p_T(B^+)$ spectrum and thus contribute to the uncorrelated systematic uncertainty listed in Table 6.2. The QCD renormalization uncertainty was determined by varying mass of the b quark by ± 0.25 GeV/c^2 and the renormalization scale, μ_0, from $\mu_0/2$ to $2\mu_0$. The Peterson parameter and the trigger efficiency systematic uncertainties were measured by varying their respective parameters by $\pm 1\sigma$. The total uncorrelated systematic uncertainty is the quadrature sum of the three individual uncertainties.

Table 6.2 lists the second class of uncertainties, the correlated systematic errors that are independent of the B^+ transverse momentum. The reconstruction uncertainty is the fractional uncertainty on the total reconstruction efficiency from the bottom line of Table 5.2.7. The luminosity systematic was taken from reference [44] while the branching ratio uncertainty comes from reference [34]. The kaon

decay-in-flight was based on the results of a simulation that about 8% of the kaons decay in flight and half were successfully reconstructed[45]. This assumes that such tracks are modeled realistically in the simulation. Like the total uncorrelated error for each p_T bin, each uncertainty contribution is assumed to be independent of the others and the total correlated uncertainty is the quadrature sum of each component listed in Table 6.2.

Table 6.2. Summary of B^+ transverse momentum dependent (uncorrelated) systematic fractional uncertainties.

Source	Error in each p_T Bin			
	7.2	10.3	13.3	18.2
QCD renormalization uncertainty	1.6%	1.5%	1.7%	1.5%
Peterson parameter uncertainty	0.7%	1.6%	1.0%	1.7%
Trigger efficiency uncertainty	3.1%	2.7%	2.1%	1.7%
Uncorrelated Total (sys_{uc})	3.6%	3.5%	2.9%	2.8%

6.3 Results

Figure 6.2 shows the differential cross section compared with the next-to-leading order NDE QCD[1] calculation using the MRST structure function set. The value of the B^+ meson transverse momentum at which to plot the four measured cross section points is described in Appendix B. The dashed lines indicate the change in the theoretical predictions as the b quark mass is varied between 4.5 and 5.0 GeV/c, the renormalization scale is varied between $\mu_0/2$ and $2\mu_0$, and the Peterson fragmentation parameter is varied between 0.004 and 0.008. Also

Table 6.3. Summary of B^+ transverse momentum independent (fully correlated) systematic fractional uncertainties.

Source	Error
Reconstruction Efficiency	$\pm 3.1\%$
Luminosity uncertainty	$\pm 4.1\%$
Branching ratio uncertainty	$\pm 10.6\%$
Kaon decay-in-flight uncertainty	$\pm 4.0\%$
Luminosity Correction	$\pm 4.0\%$
Fully Correlated Total (sys_{fc})	$\pm 13.1\%$

included in the theoretical variation is the 6.1% error on the measurement of the b quark fraction[46]. The b quark fraction is the probability that a b quark hadronizes into a B^+ mesons. The solid curve is for the central values of these parameters: $m_b = 4.75$ GeV/c^2, $\mu_0 = \sqrt{m_b^2 + p_T^2}$, $\epsilon_P = 0.006$, and $f_u = 0.375$. The measured cross section is higher than the theoretical calculations even when the free parameters are varied to increase the predictions.

The comparison between data and theory is accomplished by plotting (Data-Theory)/Theory on a linear scale as shown in Figure 6.3. The level of agreement is determined by fitting a line through the four points yielding an average ratio of 1.85 ± 0.15. The error on the scale factor is the statistical error returned by the fit and is driven by the errors from the data points which include the statistical and the uncorrelated systematic errors (see the previous section). The fitted line to the four points has a confidence level of 77% indicating excellent shape agreement between the measured and theoretical differential cross sections. The ratio of data over theory shows that the data is 2.87 ± 0.23 times higher than the theoretical

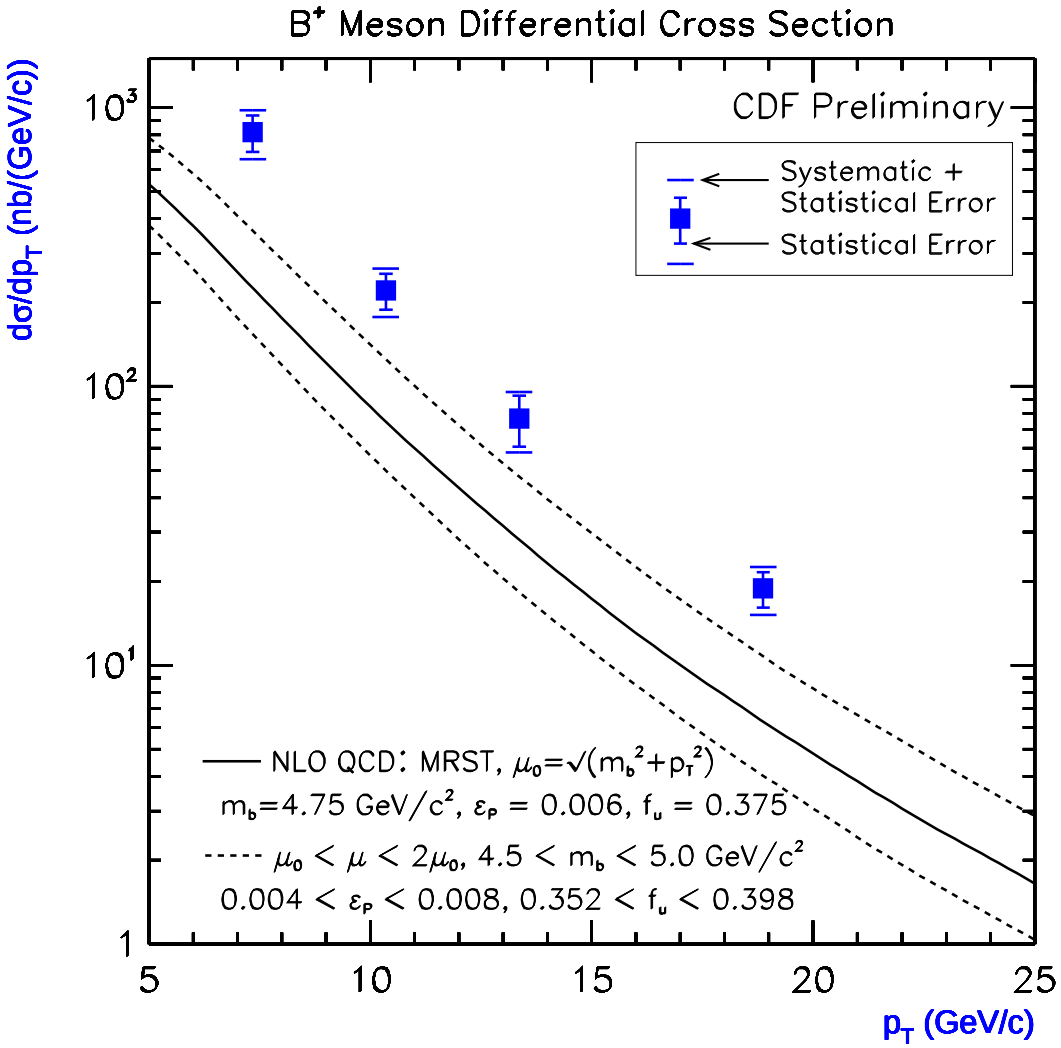

Fig. 6.2. B^+ meson differential cross measurements compared to the theoretical prediction using the MRST structure function set.

predictions. The hatched band around the fit line is fully correlated systematic errors of 13.1%. Also shown on Figure 6.3 is the comparison of CTEQ5M[47] structure functions to the MRST structure functions. The difference between the two structure functions is small compared to the uncertainty due to the variation of the renormalization scale, the b quark mass, and the Peterson parameter.

To obtain the total cross section, the last p_T bin used in the differential cross section calculation is replaced with a B^+ candidate distribution whose transverse momentum range is > 15 GeV/c and is shown in Figure 6.4. The total cross section is determined from an equation similar to that used for the differential cross section:

$$\sigma(B^+) = \left(\sum_{i=1}^{4} \frac{N^i_{signal}/2}{A_i} \right) \cdot \frac{1}{L \cdot \epsilon \cdot \mathcal{B}} \tag{6.7}$$

The first term (in parentheses) is the total number of events for $p_T(B^+) > 6.0$ GeV/c which is the sum of the acceptance corrected number of signal events found in each p_T bin. The acceptance measured for the p_T range of > 15 GeV/c is $10.19 \pm 0.04\%$ and the measured total cross section is

$$\sigma_B(p_T \geq 6.0\,\mathrm{GeV/c},\ |\mathrm{y}| \leq 1.0) = 3.52 \pm 0.38(\mathrm{stat} + \mathrm{sys_{un}}) \pm 0.46(\mathrm{sys_{fc}})\,\mu\mathrm{b}. \tag{6.8}$$

where the second error is the quadrature sum of the statistical and uncorrelated systematic uncertainties.

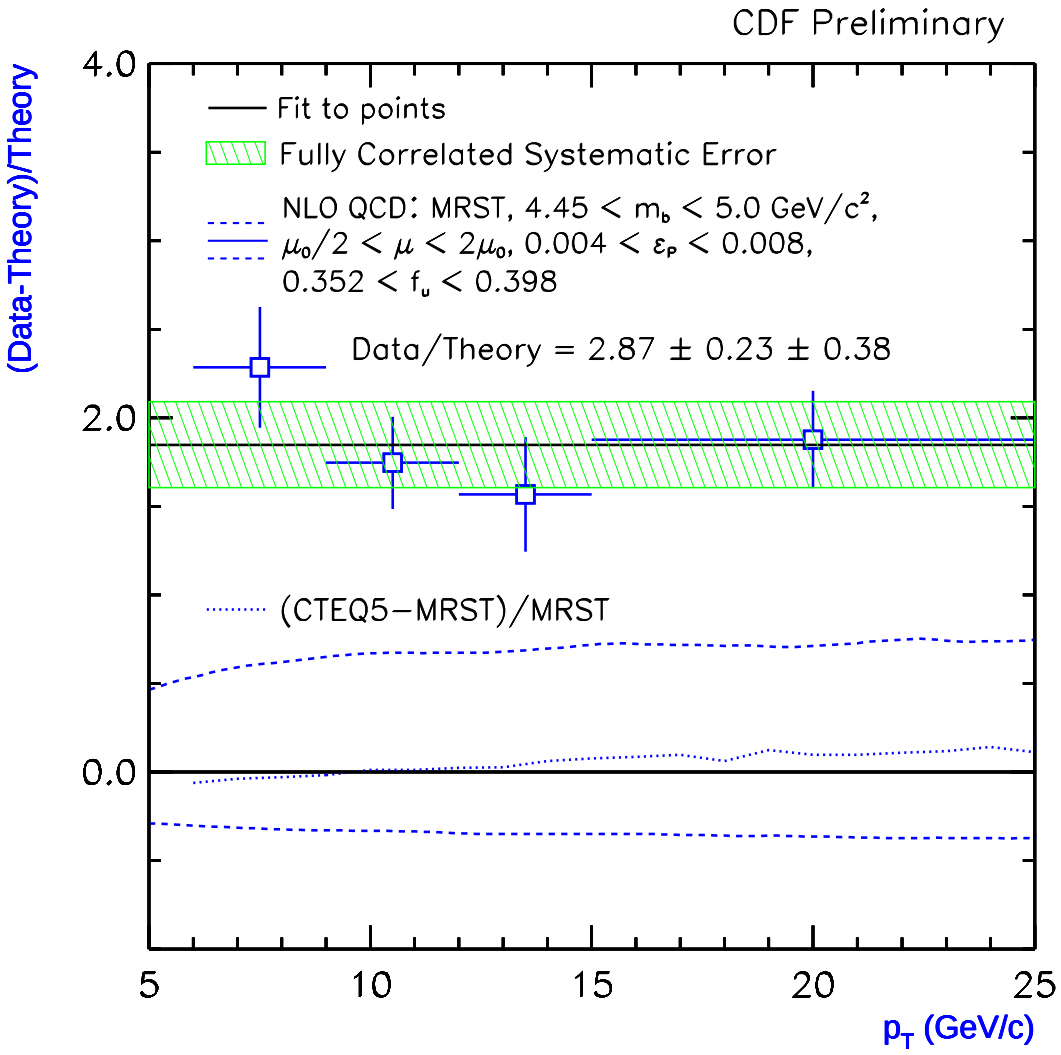

Fig. 6.3. Plot of (Data-Theory)/Theory as a shape comparison with the NLO QCD differential cross section calculations using the MRST and CTEQ5M structure function sets.

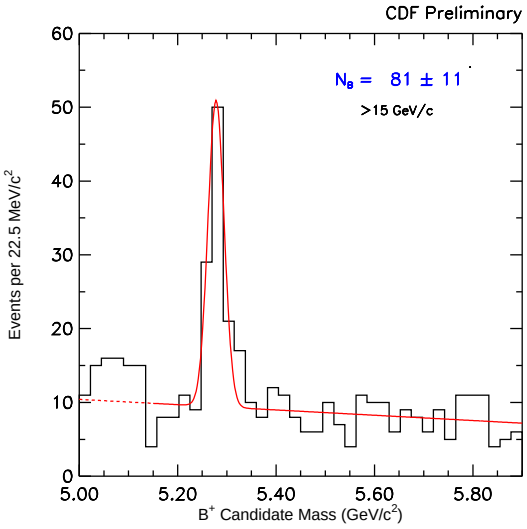

Fig. 6.4. B^+ candidate distribution for the transverse momentum range of $p_T >$ 15.0 GeV/c. This range replaces the 15-25 GeV/c momentum range so that the total B^+ meson cross section can be calculated.

7. CONCLUSIONS

The exclusive decay $B^+ \to J/\psi\, K^+$ was used to measure the production cross section of the B^+ meson from collected by the CDF detector. A sample size of 387 ± 32 events was obtained from $\int \mathcal{L} dt = (108.1 \pm 4.5)$ pb^{-1} of 1.8 TeV proton-antiproton collisions produced by the Fermilab Tevatron collider.

The measured total B^+ production cross section for $p_T(B^+) \geq 6.0$ GeV/c and $|y| \leq 1.0$ is

$$\sigma_B(p_T \geq 6.0\,\mathrm{GeV/c},\ |\mathrm{y}| \leq 1.0) = 3.52 \pm 0.38(\mathrm{stat} + \mathrm{sys_{un}}) \pm 0.46(\mathrm{sys_{fc}})\,\mu\mathrm{b} \quad (7.1)$$

where the first uncertainty is the combined statistical uncorrelated systematic uncertainties and the second is the fully correlated systematic uncertainty. The differential cross section is measured to be 2.87 ± 0.23 times (1.85 ± 0.15 for the ratio of (Data - Theory)/Theory) higher than the NLO QCD predictions with excellent agreement in shape.

APPENDICES

APPENDIX A: DIMUON TRIGGERS

The dimuon triggers that were used to construct the data samples studied in this analysis are listed below. The Level 2 trigger along with the prerequisite Level 1 trigger are shown. Refer to Section 4.2.2 for a description of the Level 2 triggers and Section 4.2.1 for the Level 1 triggers.

A.1 Run 1A Dimuon Triggers

Only one dimuon trigger was utilized in this analysis for the data taken in Run 1A: TWO_CMU_ONE_CFT. This trigger required two CMU Level 2 muon clusters with one of the clusters required to match a CFT track. The Level 1 prerequisite trigger is TWO_CMU_3PT3. This trigger is dynamically prescaled.

A.2 Run 1B Dimuon Triggers

For Run 1B, three dimuon triggers were utilized.

1. TWO_CMU_TWO_CFT: Two CMU Level 2 muon clusters and two matching CFT tracks were required. The Level 1 prerequisite trigger is TWO_CMU_3PT3. This trigger is not prescaled, and the two muon clusters are required to be in non-contiguous modules. If one cluster is in the $+z$ region of the CDF Detector and the other cluster is in the $-z$ region, then the two clusters are required to have different ϕ values.
2. TWO_CMU_CMX_TWO_CFT: Either two CMU Level 2 or one CMU and one CMX Level 2 muon clusters are required with each muon track matching a CFT track. The prerequisite Level 1 trigger is TWO_CMU_3PT3. The trigger is dynamically prescaled.
3. TWO_CMU_ONE_CFT_6TOW: Two adjacent CMU Level 2 muon stubs, which together form a single cluster that spans six or more calorimeter trigger

towers, are necessary. The single cluster is required to match a CFT track, and the Level 1 prerequisite trigger is TWO_CMU_3PT3. The trigger is dynamically prescaled and is intended to offset losses due to the requirement of non-contiguous modules imposed in the TWO_CMU_TWO_CFT trigger.

APPENDIX B: MEAN p_T DETERMINATION

To obtain the values of $p_T(B)$ at which the differential cross section points are plotted, the integrated cross section for each p_T range is first determined from the theoretical prediction and then divided by the width of the tranxverse momentum bin. The resulting value is found on the central theoretical curve and the corresponding p_T is found. Table B.1 shows the transverse momentum point in each p_T range.

Table B.1. Mean B^+ meson p_T for the four transverse momentum ranges used to determine the differential cross section.

p_T Range (GeV/c)	$\langle p_T \rangle$ (GeV/c)
6 - 9	7.34
9 - 12	10.35
12 - 15	13.36
15 - 25	18.87

APPENDIX C: CTC TRACK RECONSTRUCTION EFFICIENCY

C.1 Introduction

Any exclusive cross section analysis relying on the tracking information supplied by the CTC requires knowledge of the track reconstruction efficiency. There have been several studies in the past [48, 33, 49, 50] that have measured the reconstruction efficiency using the technique of track embedding (a short summary of each measurement is located in the appendix). An improved study of the CTC track reconstruction efficiency is presented.

Monte Carlo tracks are embedded into data events and then identified using a χ^2 matching technique, both described in detail below. The study done by Andreas Warburton[33] incorporated occupancy effects by using data-tuned wire-hit efficiencies. We focus on "aging" of the CTC – the deterioration of the track reconstruction over the course of Run 1B that cannot be attributed to instantaneous luminosity effects. The CTC was thought to have shown some signs of aging through the studies of [51, 52, 42]. Greg Field, *et al.* and Paul Ngan, *et al.* have shown a loss in the J/ψ yield even after correcting for the occupancy effects measured by Warburton. This study was an attempt to find the origin of the J/ψ loss. The conclusion is that there is no observable "aging" in the CTC track reconstruction and therefore cannot be used to explain the loss of J/ψ 's.

C.2 Data Sample

The data sample for this study is comprised of $\sim 42,000$ displaced J/ψ 's selected from the Run 1B DST files residing on tape. Using CTC or SVX (if available) information, the J/ψ 's were selected using the cuts shown in table C.1. Canonical CTC quality cuts - two axial superlayers with four or more hits and two stereo superlayers with two or more hits - were imposed on the muons along with

a 3.5 GeV/c transverse momentum requirement on the J/ψ . The proper decay length of the J/ψ was required to be greater than 100 μm. CTVMFT was used to constrain the two muons to a common vertex. Once selected, the SVX information was ignored for the rest of the procedure.

Table C.1. Data J/ψ selection requirements.

$ct \geq 100\mu$m
2 Axial layers with $\geq$ 4hits
2 Stereo layers with $\geq$ 2 hits
$Prob(\chi^2) \geq 0.01$
$2.9 \leq M_{\mu^+\mu^-} \leq 3.3$ GeV/c^2
$p_T\,(M_{\mu^+\mu^-}) \geq 3.5$ GeV/c

The data sample comes mainly from runs at the beginning and the end of Run 1B. Figures C.1 and C.2 show the instantaneous luminosity profile of the event sample and the Run 1B data set, respectively, while figures C.3 and C.4 compare the class-12 primary vertex distributions of each.

C.3 Track Embedding Procedure

The embedded tracks are generated by decaying Monte Carlo $B^{\pm}$ mesons with QQ[53] via the mode $B^+ \rightarrow J/\psi\, K^+$. The difference in direction between the Monte Carlo J/ψ and the data J/ψ is used to create a rotation matrix for the kaon track to preserve the orientation of the simulated $K^{\pm}$ with respect to the data J/ψ (see Appendix D. After the kaon track is rotated, the helix parameters are calculated and used as input to CTADDH[54]. The curvature (c), azimuth

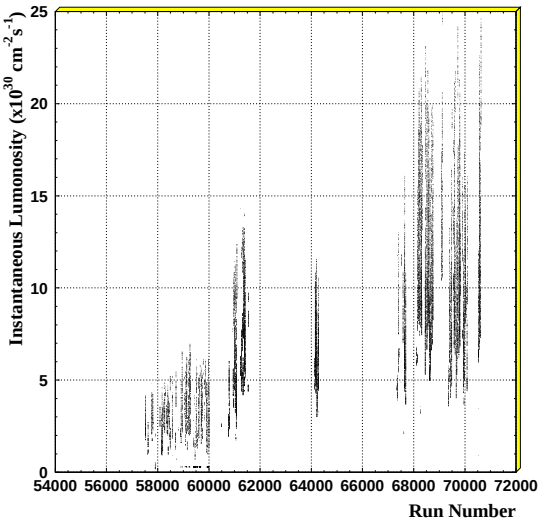

Fig. C.1. Instantaneous luminosity profile of the selected events for the embedding sample.

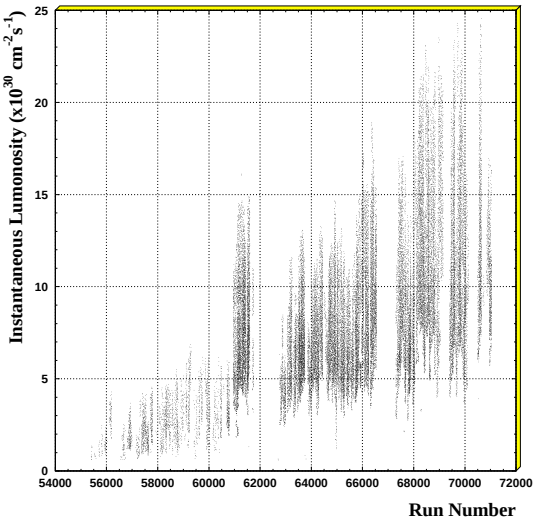

Fig. C.2. Instantaneous luminosity profile of the Run 1B data set.

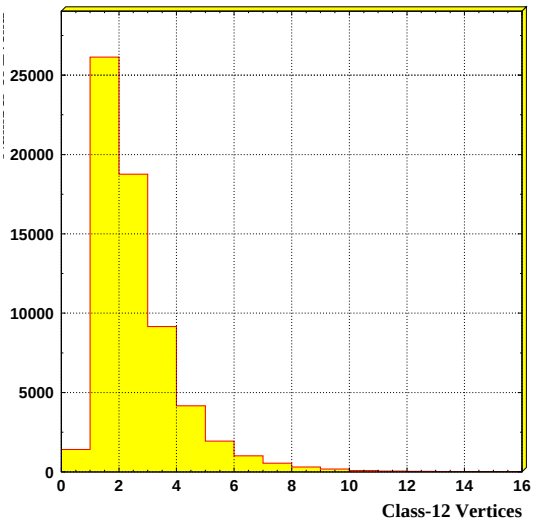

Fig. C.3. Class-12 primary vertex distribution of the embedding sample.

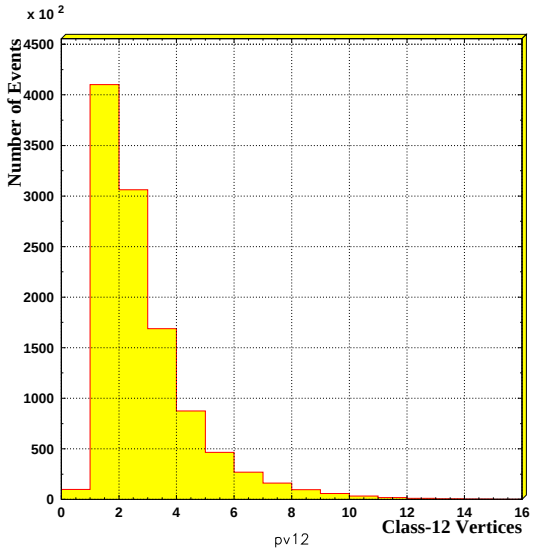

Fig. C.4. Class-12 primary vertex distribution of the Run 1B data set.

(ϕ_0), and polar angle ($cot\theta$) helix parameters of the tracks to be embedded are derived from the 3-momentum and charge information of the simulated kaon track. Additional information from the data J/ψ decay vertex is used to calculate the impact parameter (d_0) and the longitudinal displacement (z_0). The exit radius of the track is calculated and required to be greater than 130.0 cm *before* the track can be embedded. Once the track parameters are known, they are stored for later use, and the routines CTADDH and CVADDH are used to embed the hits into the CTC data banks.

C.3.1 Run and Pseudo-Rapidity Dependence

CTADDH, by default, embeds tracks with 100% wire-hit efficiencies for each of the 84 wire layers. It has been shown [51] that the average number of used hits per super layer in the track fit decreases as a function of instantaneous luminosity. To include this effect in the reconstruction efficiency, Andreas Warburton [33] iteratively adjusted the wire-hit efficiencies in the subroutine CTADDH.CDF until the mean number of hits per superlayer used in the embedded-track fits matched those measured in data [51]. This was done for both axial and stereo superlayers. The inner superlayers of the CTC had the biggest reduction in the wire-hit efficiency.

Once the number of used hits per super layer for data and embedded tracks converged, the reconstruction efficiency was studied as a function of several observables such as the transverse momentum, the exit radius, the instantaneous luminosity, and the number of class 12 vertices. Even though the reduced wire-hit efficiencies were not given a run dependence (*i.e.* constant with respect to the run number), the two-track reconstruction efficiency was shown to decrease with run number when all primary vertex multiplicities were considered. Restricting the

efficiency to the events with only one Class-12 primary vertex, the decrease was eliminated concluding that the most deleterious effect on the pattern recognition is the one of occupancy. The run dependence is a reflection of the fact the higher instantaneous luminosity events occurred toward the end of the run while the lower instantaneous luminosity events were at the beginning of the run.

A variation on the above procedure was devised to quantify how much of the reconstruction efficiency degradation can be attributed to aging as opposed to occupancy effects. Therefore, the wire-hit efficiencies were tuned to yield the same mean number of used hits for the reconstructed muon tracks coming from $J/\psi \rightarrow \mu^+\mu^-$ decays as a function of run number and pseudo-rapidity η. The data used for tuning the wire-hit efficiencies were the muon legs of the side-band subtracted J/ψ's. Events with only one class-12 primary vertex were used to ensure that the reduced wire-hit efficiencies would reflect the aging of the chamber and not instantaneous luminosity effects.

We divide Run 1B into the same 11 run bins used in the trigger efficiency module DIMUTG [38]. Figures C.5 and C.6 show the average number of used hits as a function of run number for muon tracks in data. Figures C.7 and C.8 show the average number used hits for both axial and stereo layers for the embedded tracks after iteratively adjusting the wire-hit efficiencies in CTADDH.

The used-hit dependence on η, tuned simultaneously with the run dependence, is parameterized as a parabola. Figures C.9 and C.10 show the used hit profiles of the axial superlayers for early and late run bins, respectively. The most prominent feature in the figures is the decrease in the number of used hits at low η, specifically in super layers 0 and 2. The dip at low η is a result of less charge deposited in the CTC resulting in fewer hits with pulse height over threshold for the track fit. Like the used hit run dependent plots, these were created using side-band subtracted

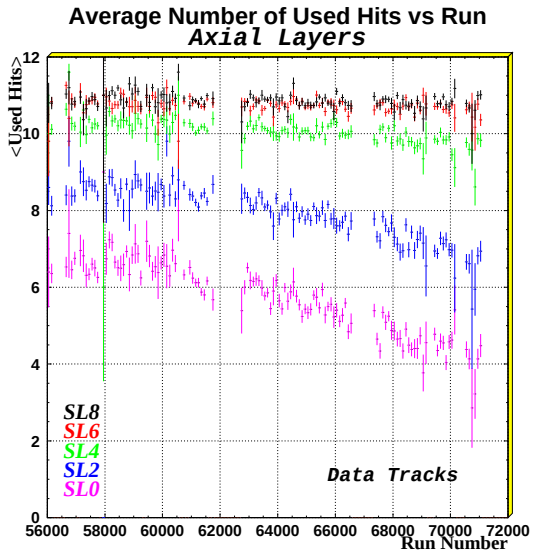

Fig. C.5. Average number of used hits vs run for muons from data for the axial superlayers of the CTC.

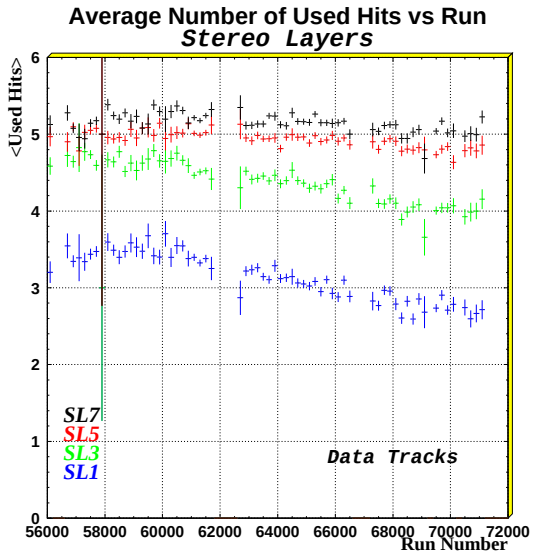

Fig. C.6. Average number of used hits vs run for muons from data for the stereo superlayers of the CTC.

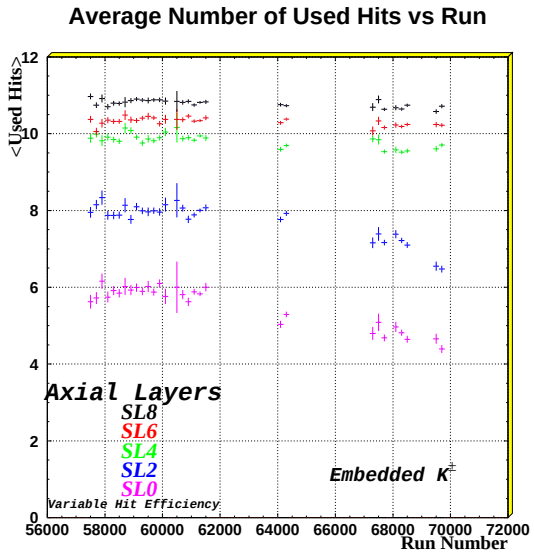

Fig. C.7. Average number of used hits vs run for the embedded tracks for the axial superlayers of the CTC.

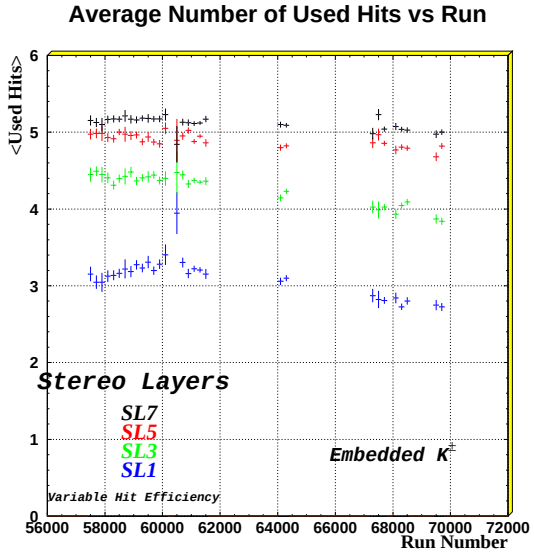

Fig. C.8. Average number of used hits vs run for the embedded tracks for the stereo superlayers of the CTC.

muon data and restricting the events to those containing only one primary vertex. Figures C.11 and C.10 show the used hits for the embedded tracks as a function of η for early and late runs. Run bin 2, with about 7 pb^{-1} of data, represents the range 58324 to 60881 and run bin 10, approximately 11 pb^{-1}, encompasses runs 69095 to 70150. Comparing figures C.9 and C.10 with the figures C.11 and C.10 show a good agreement of tuned wire-hit efficiencies. Figures C.13, C.14, C.15 and C.16 show similar agreement in the stereo layers.

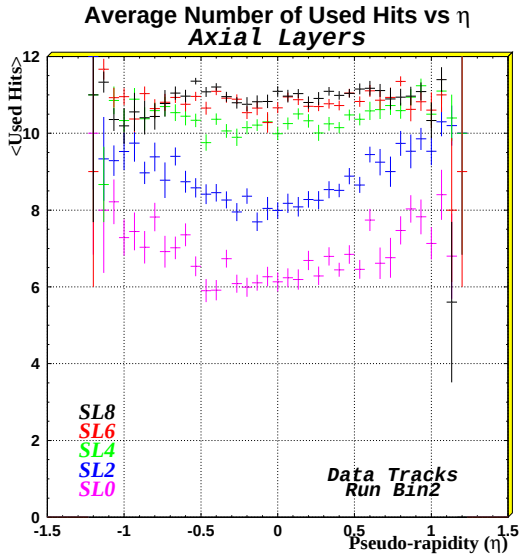

Fig. C.9. Pseudo-rapidity dependence of the used hits in the axial layers of the CTC for muon data. Run bin 2 is the run range 58324 to 60881.

C.3.2 "Found" Track Definition

Using the same method as [33] which is described in [34], a matching χ^2 was calculated using the embedded (α) and reconstructed ($\widehat{\alpha}$) helix parameters of a track with the expression

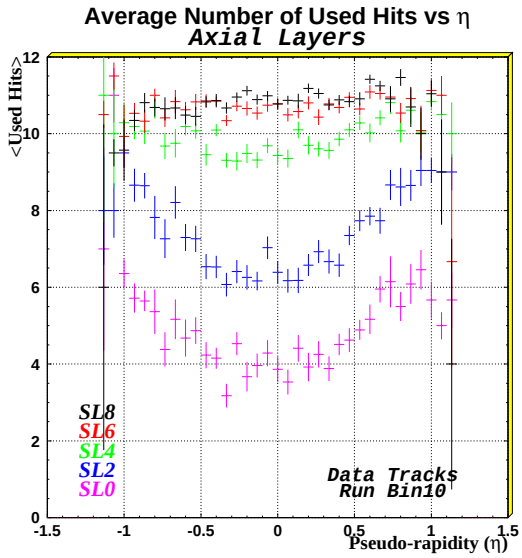

Fig. C.10. Pseudo-rapidity dependence of the used hits in the axial layers of the CTC for muon data. Run bin 10 is the range 69095 to 70150.

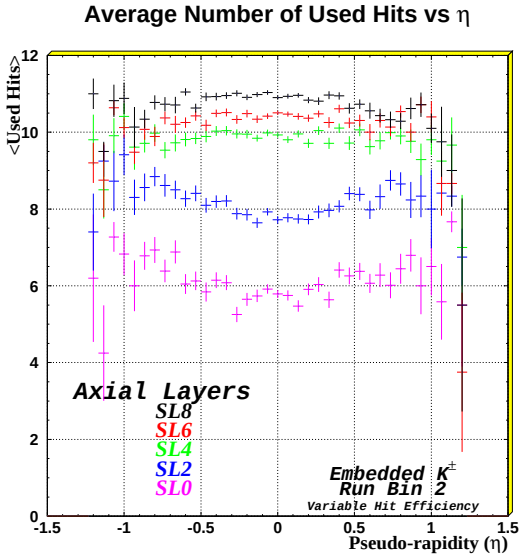

Fig. C.11. Pseudo-rapidity dependence of the used hits in the axial layers of the CTC for the embedded tracks. Run bin 2 is the run range 58324 to 60881.

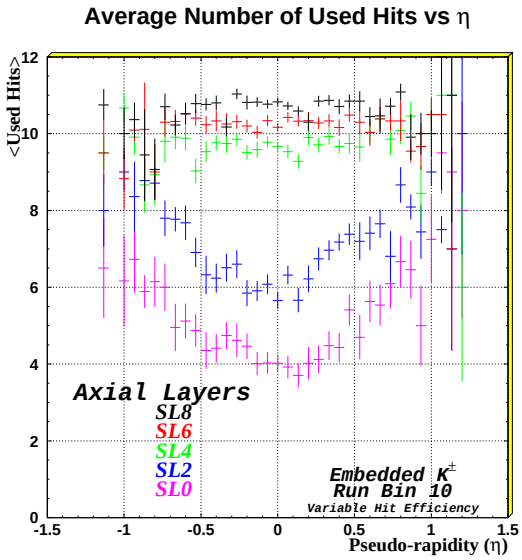

Fig. C.12. Pseudo-rapidity dependence of the used hits in the axial layers of the CTC for the embedded tracks. Run bin 10 is the range 69095 to 70150.

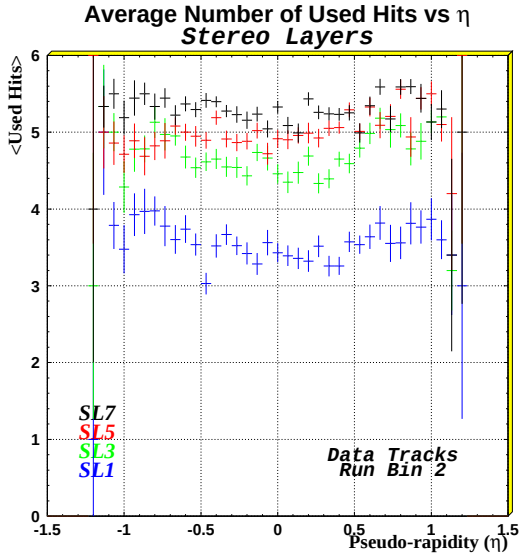

Fig. C.13. Pseudo-rapidity dependence of the used hits in the stereo layers of the CTC for muon data. Run bin 2 is the run range 58324 to 60881.

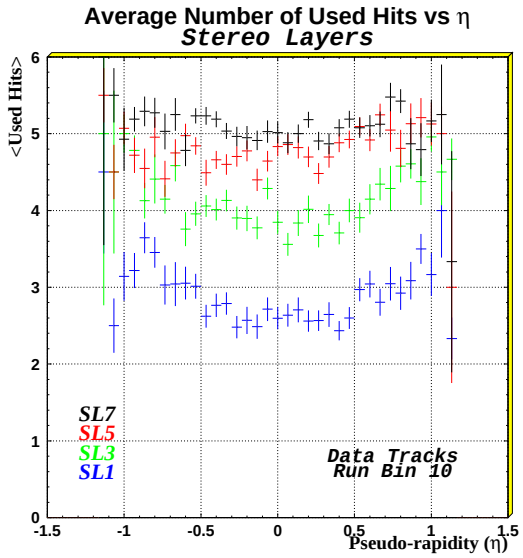

Fig. C.14. Pseudo-rapidity dependence of the used hits in the stereo layers of the CTC for muon data. Run bin 10 is the range 69095 to 70150.

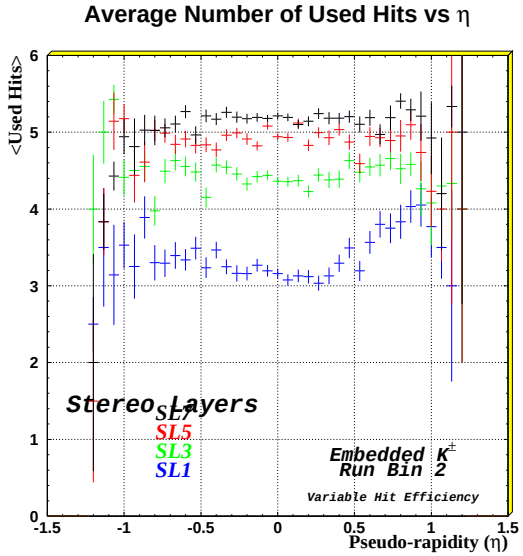

Fig. C.15. Pseudo-rapidity dependence of the used hits in the stereo layers of the CTC for the embedded tracks. Run bin 2 is the run range 58324 to 60881.

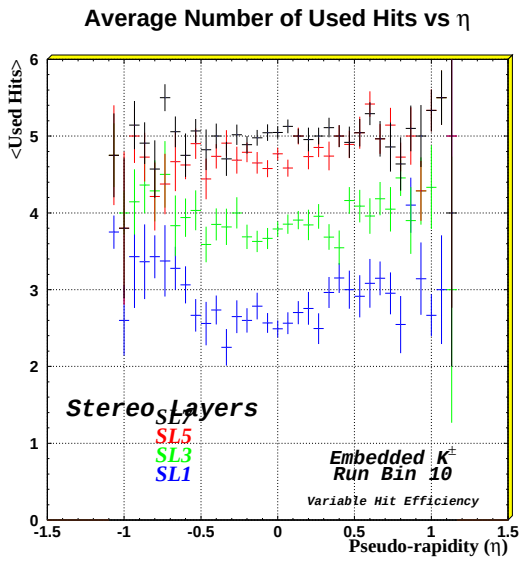

Fig. C.16. Pseudo-rapidity dependence of the used hits in the stereo layers of the CTC for the embedded tracks. Run bin 10 is the range 69095 to 70150.

$$\chi^2 = (\alpha - \widehat{\alpha})^T \widehat{V^{-1}} (\alpha - \widehat{\alpha}), \tag{C.1}$$

where $\widehat{V}$ is the 5×5 covariance matrix of the reconstructed track. For each track in the reconstructed event, the χ^2 was formed and the track with the smallest χ^2 was retained for consideration as the "found" track. Figure C.17 shows plots of the matching χ^2 distributions for positive and negative embedded kaons. The distributions are fit to a χ^2 probability density function plus an exponential background [50]:

$$P(\chi^2) = \frac{P1}{P2}\left(\frac{\chi^2}{P2}\right)^{\frac{P3}{2}-1} \exp\left(-0.5\left(\frac{\chi^2}{P2}\right)\right) + P4 \times P5 \exp\left(-P5\chi^2\right) \tag{C.2}$$

Fixing the number of degrees of freedom ($P3$) to 5.0 (the error of 1.414 is an artifact of PAW caused when the parameter is fixed), the fit yields a scale factor ($P2$) of 1.6.

Contrary to past studies, we have not scaled the covariance matrix by a factor of 2.0. Reference [50] used a scale factor of ~ 1.3 for all parameters except for the

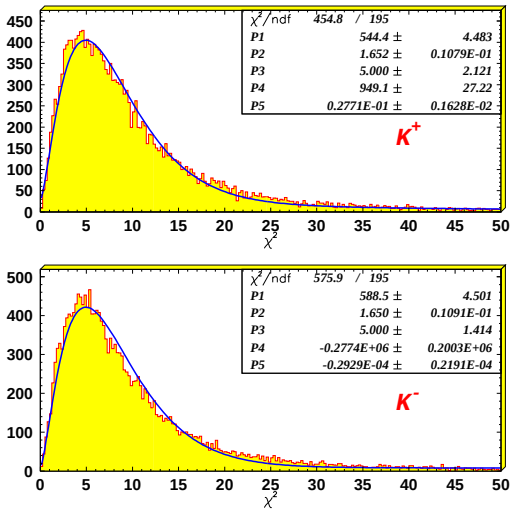

Fig. C.17. Minimum matching χ^2 distributions (histograms) for embedded K^+ (top) and K^- (bottom). The fitting function (curve) is defined in Equation. C.2.

curvature, which was scaled according to a parameterization of track p_T. Equation C.2 was used as the fitting function to check that the distributions were consistent with five degrees of freedom and a scale factor of 1.0. Reference [33] used a global scale factor of 1.5 achieving a fit consistent with five degrees of freedom and a scale factor of 1.0. Monte Carlo tracks are not expected to need a scale factor for the covariance matrix. However, the fit to the distributions shown in figure C.17 show that a scale factor of $\sim$ 1.6 is required. We cannot explain the need of a scale factor for Monte Carlo tracks.

A global scale factor for the reconstructed covariance matrix is inadequate as indicated by the track parameter pull distributions shown in figures C.18 and C.19. Since the pull distributions have different widths, a scale factor for each track parameter would be more appropriate. These distributions contain the information from the embedded tracks for early and late runs as well as for all p_T.

A summary of the track parameter pull distributions widths and means are shown in Tables C.2 and C.3, respectively. The row labeled "Early" represents run numbers less than 62000, while "Late" refers to run numbers greater than 67000. "Low p_T ", "Mid p_T ", and "High p_T " refer to track parameter pulls made with the transverse momentum of the embedded track in the $0.4 \leq p_T \leq 1.0$ GeV/c range, the $1.0 \leq p_T \leq 2.0$ GeV/c range, or the p_T >2.0 GeV/c range. Each distribution was fit with a Gaussian function.

As can be seen in Table C.2, there is no change between the early and late runs in the widths of the r-ϕ track parameter pulls. The r-z parameters do change - getting larger as Run 1B progressed. The widths of all five parameters did vary over the three different p_T bins.

Table C.2. Summary of the widths of the track parameter pulls. The format of each entry is (positive track)/(negative track).

Parameter Pull Widths					
	c	d_0	ϕ_0	$\cot\theta$	z_0
Average	1.60/1.60	1.35/1.33	1.21/1.20	1.42/1.38	1.47/1.42
Early	1.66/1.68	1.43/1.41	1.25/1.24	1.34/1.30	1.43/1.39
Late	1.66/1.68	1.43/1.41	1.25/1.24	1.47/1.41	1.58/1.49
Low p_T	1.68/1.67	1.05/1.09	1.03/1.06	1.01/0.84	1.64/1.47
Mid p_T	1.74/1.76	1.21/1.19	1.07/1.07	1.33/1.20	1.53/1.41
High p_T	1.59/1.60	1.43/1.41	1.27/1.25	1.43/1.39	1.47/1.43

The one relenting empirical fact is that for a sufficiently high minimum matching χ^2, the efficiencies are relatively insensitive to the covariance scale factors.

Table C.3. Summary of the means of the track parameter pulls. The format of each entry is (positive track)/(negative track).

Parameter Pull Mean					
	c	d_0	ϕ_0	$\cot\theta$	z_0
Average	-0.08/0.25	-0.14/0.27	0.13/-0.24	-0.09/0.03	0.11/-0.05
Early	-0.05/0.26	-0.13/0.29	0.12/-0.25	-0.07/0.05	0.10/-0.06
Late	-0.12/0.25	-0.16/0.26	0.13/-0.25	-0.12/0.01	0.11/-0.03
Low p_T	-0.65/0.62	-0.18/0.35	0.10/-0.20	-0.20/0.12	0.31/-0.31
Mid p_T	-0.21/0.45	-0.14/0.35	0.10/-0.24	-0.14/0.07	0.18/-0.11
High p_T	-0.28/0.20	-0.13/0.26	0.13/-0.25	-0.07/0.02	0.09/-0.03

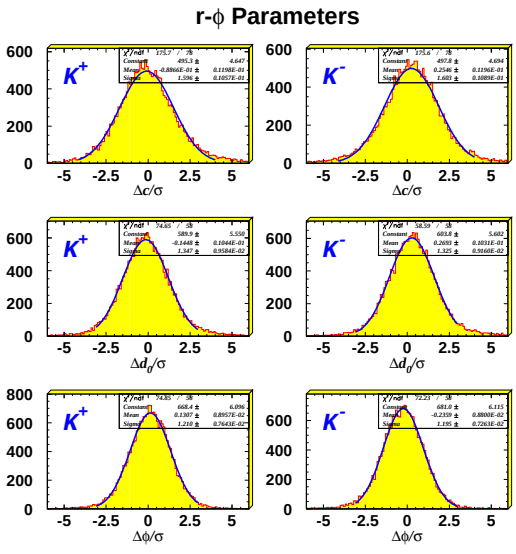

Fig. C.18. The individual pull distributions for the r-ϕ helical parameters. Parameters P1 through P3 are the Gaussian function parameters (normalization, mean and width).

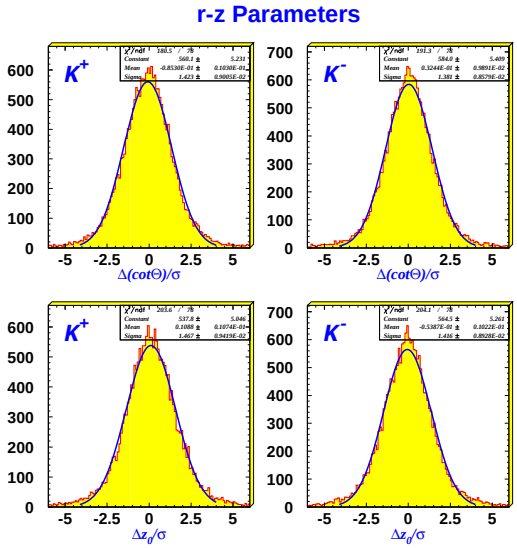

Fig. C.19. The individual pull distributions for the r-z helical parameters. Parameters P1 through P3 are the Gaussian function parameters (normalization, mean and width).

This can be seen by looking at plots of the minimum matching χ^2 vs the next-to-minimum matching χ^2 which is shown in figure C.20. Therefore, using precedence [33], a track is designated as found if its matching χ^2 is less than 500:

$$\chi^2 < 500. \tag{C.3}$$

Figure C.20 shows that the cut at 500 is efficient at separating found tracks and any other track in the event. In the case where no track passed the cut, the minimum matching χ^2 was, in general, much larger than 500. Figure C.21 shows the p_T dependence of the minimum matching χ^2 of the reconstructed tracks. There is no observable p_T dependence.

C.4 Efficiencies

The track reconstruction efficiency is defined as the number of found tracks, $\chi^2_{min} < 500$, divided by the total number of embedded tracks. Since the generated

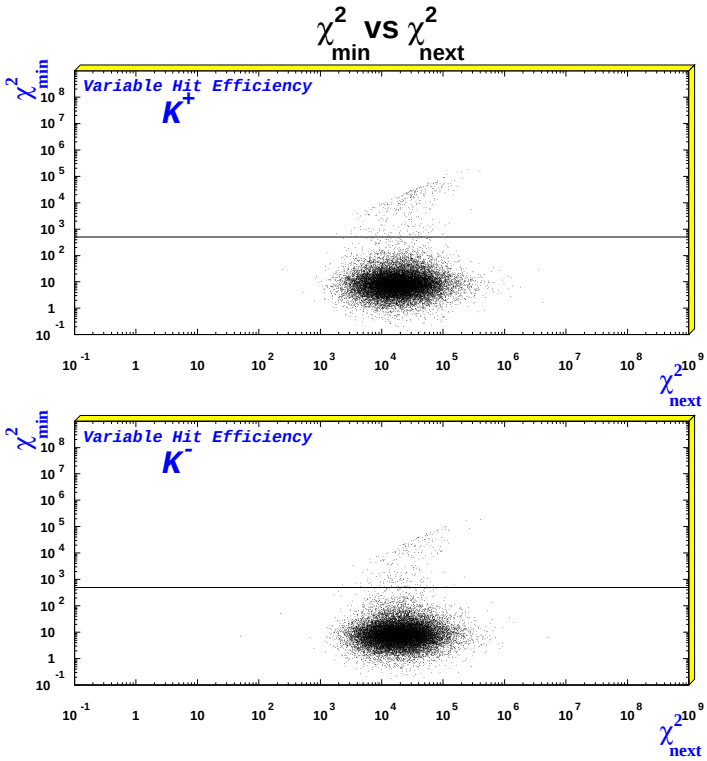

Fig. C.20. The minimum matching χ^2 vs the next-to-minimum matching $\chi^2$for positive kaons (top) and negative kaons (bottom). The horizontal line represents the maximum value for a "found" track.

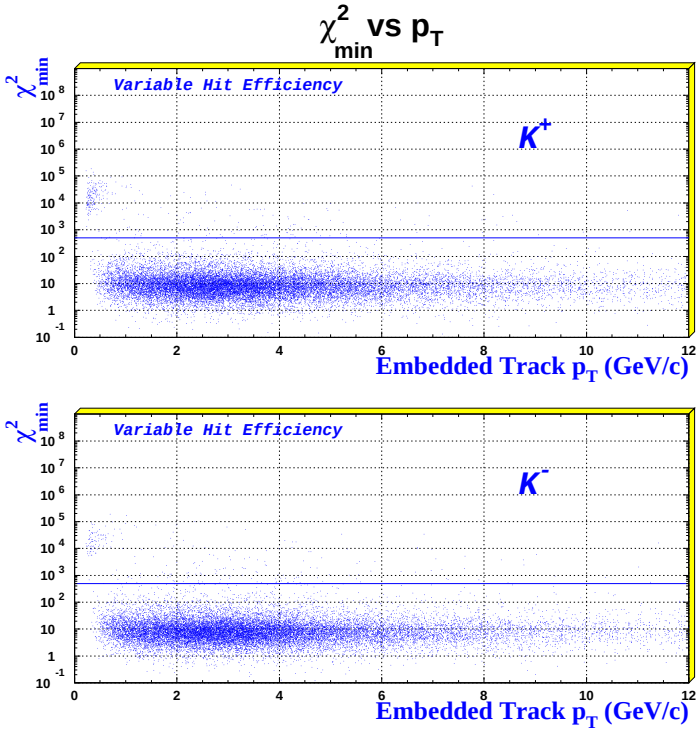

Fig. C.21. The minimum matching χ^2 vs the embedded track transverse momentum. The horizontal line shows the "found" track cut. The top plot is for positive kaons and the bottom plot for negative kaons.

track was required to have an exit radius of 130 cm before it could be embedded, the following efficiencies did not have an exit radius cut on the reconstructed tracks. "Early" refers to runs below 62000 while "late" pertains to runs 67000 and above. The efficiencies were made for early and late runs to study the effect of a time dependent tracking degradation and the instantaneous luminosity effects have been removed by using the wire-hit efficiencies described in section C.3.

C.4.1 p_T Dependence

The p_T dependence of the efficiency plotted for early and late runs is shown in figure C.22. There is a slight difference in efficiency between the early and late runs for $p_T < 0.75$ GeV/c. No run dependent differences were observed for tracks with a transverse momentum exceeding 0.8 GeV/c. The errors shown are statistical only. Figure C.23 combines the early and late run samples and is then fit using Equation C.4

$$\epsilon = P1 * Freq(\frac{x - P2}{P3}) * Freq(\frac{x - P4}{P5}) \tag{C.4}$$

where *Freq* is the frequency function

$$Freq(x) = \frac{1}{\sqrt{2\pi}} \int_{-\infty}^{x} \exp(\frac{t^2}{2}) dt, \tag{C.5}$$

P1 is plateau efficiency at infinite p_T, and P2 through P5 are parameters defining the two onset functions. The fit results in a plateau reconstruction efficiency of 99.6±0.9% per track.

C.4.2 Primary Vertex Dependence

Three p_T bins have been used to examine the dependence of the tracking efficiency as a function of the number of class 12 primary vertices. The bins are listed below.

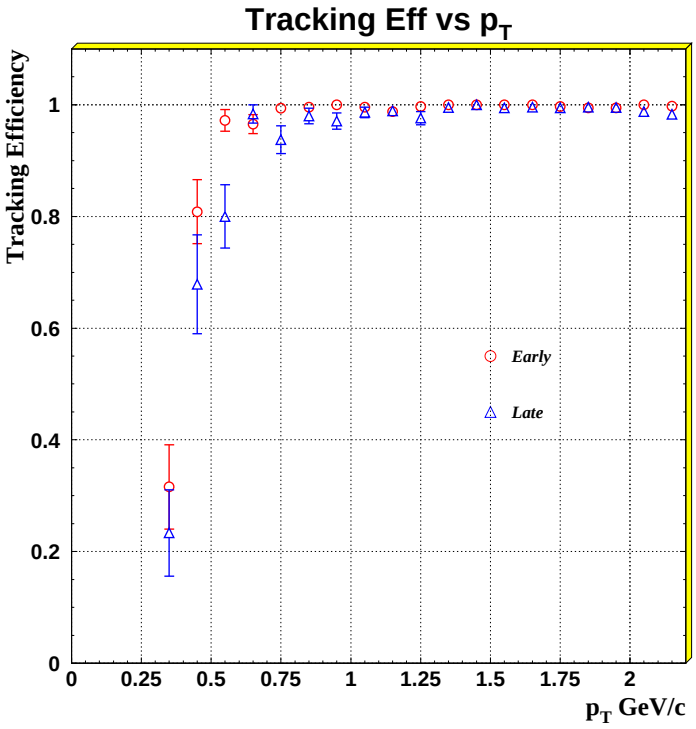

Fig. C.22. Tracking efficiency vs p_T for the early and late runs.

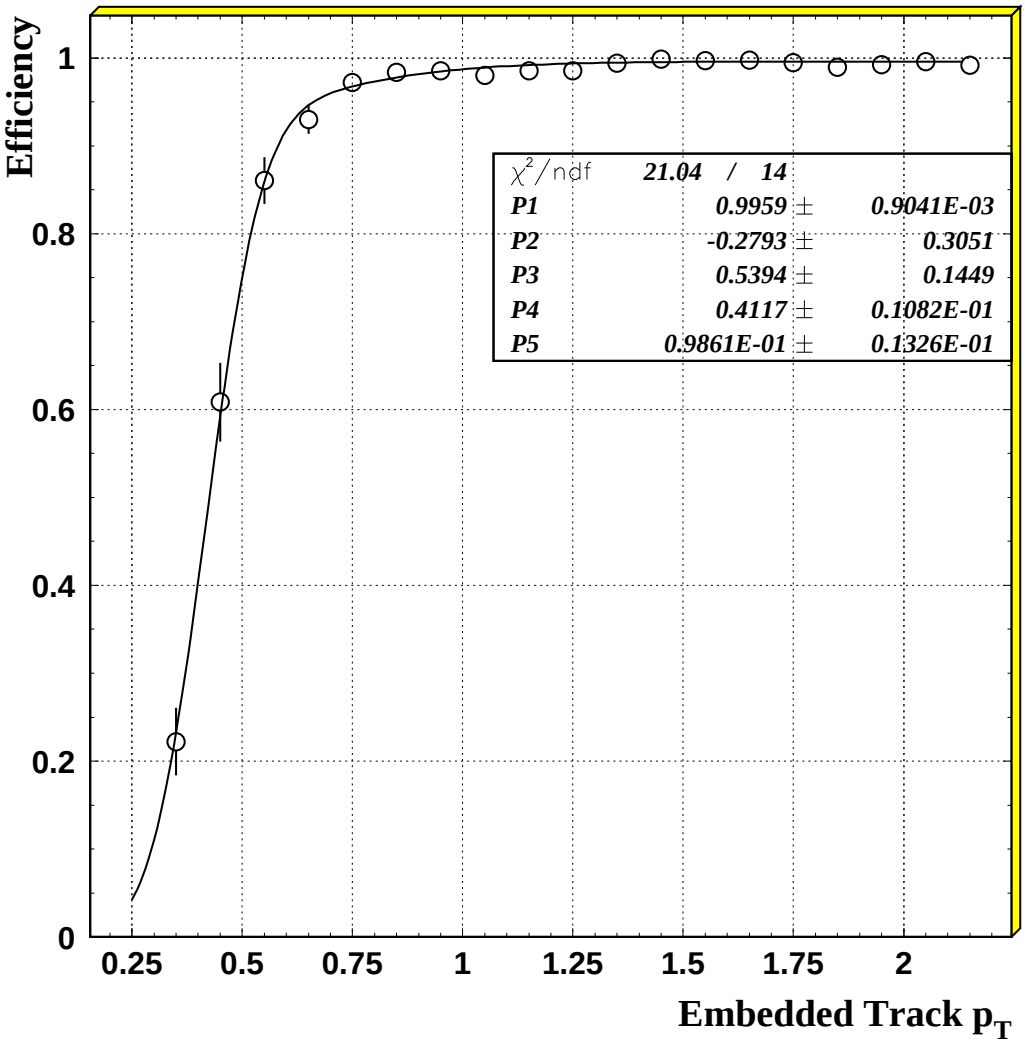

Fig. C.23. Tracking efficiency vs p_T combining the early and late runs. The plateau efficiency is 99.6±0.9%.

1. $0.4 \leq p_T \leq 1.0$ GeV/c
2. $1.0 \leq p_T \leq 2.0$ GeV/c
3. $p_T > 2.0$ GeV/c

We show no statistical difference in the tracking efficiency, see figure C.24, between early and late runs for events with five or fewer primary vertices in the low momentum bin. Figures C.25 and C.26 show the tracking efficiency for the mid and high momentum bins. The track reconstruction efficiency for tracks with $p_T > 1.0$ GeV/c falls at very high CTC occupancy, but the behavior is consistent throughout the course of Run 1B showing that there is no observed effect associated with wire aging. It should be noted that, while this indicates that the ability to reconstruct a track does not decrease rapidly as the individual hit efficiencies decrease, the quality of the fit can be expected to degrade as hits are lost, which should be, in principal, reflected in the track covariance matrix.

C.4.3 Run Dependence

The run dependence of the reconstruction efficiency is shown in figure C.27 for the low p_T bin with an observable drop of less than 5%. The mid and high p_T bins are shown in Figures C.28 and C.29. We observe only a slight loss of efficiency over the course of Run 1B. Figures C.30, C.31, and C.32 show the same plots without the restriction of four or fewer primary vertices. Figures C.28 through C.32 show that occupancy and time do not affect the track reconstruction efficiency for tracks with $p_T > 1.0$ GeV/c. Comparing figures C.27 and C.30 reveals that increased event multiplicity does degrade the track reconstruction efficiency for low p_T tracks.

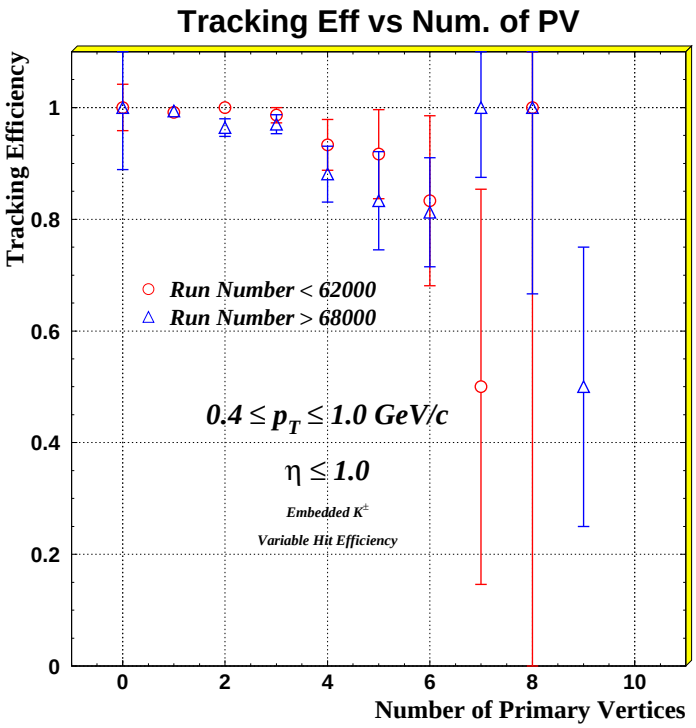

Fig. C.24. Tracking efficiency vs number of class 12 primary vertices for the low p_T momentum bin.

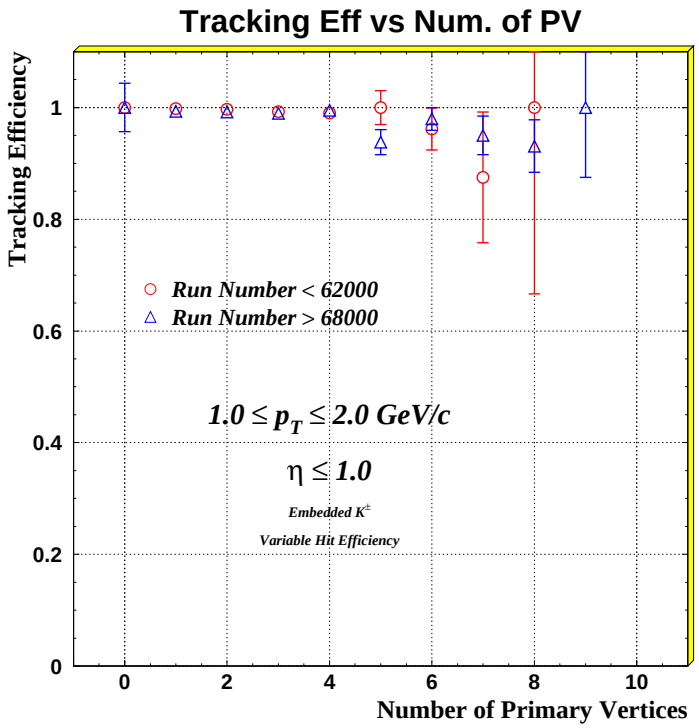

Fig. C.25. Tracking efficiency vs number of class 12 primary vertices for the mid p_T and high p_T momentum bins.

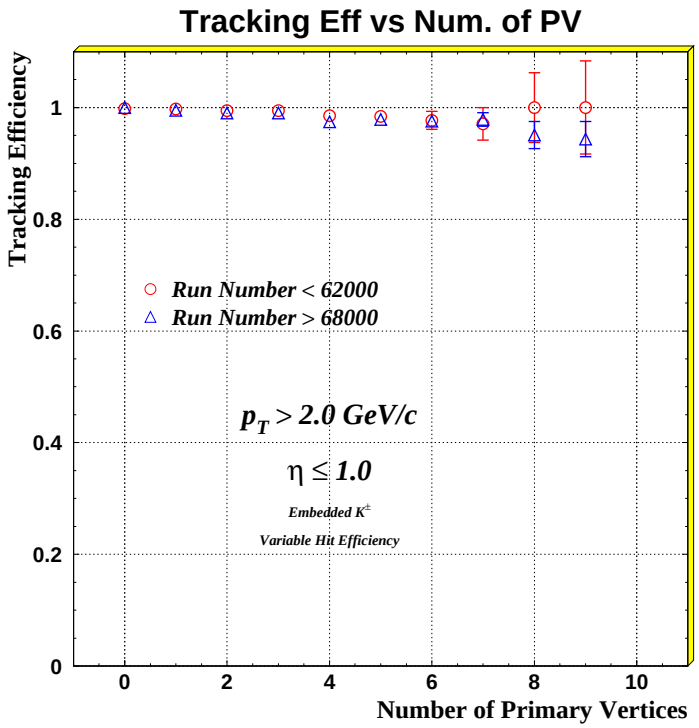

Fig. C.26. Tracking efficiency vs number of class 12 primary vertices for the mid p_T and high p_T momentum bins.

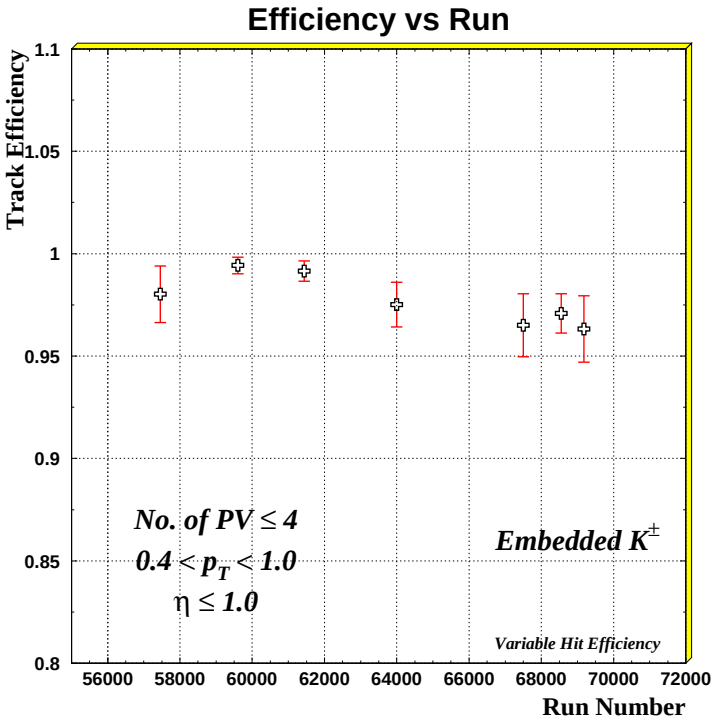

Fig. C.27. Tracking efficiency vs Run for low momentum tracks.

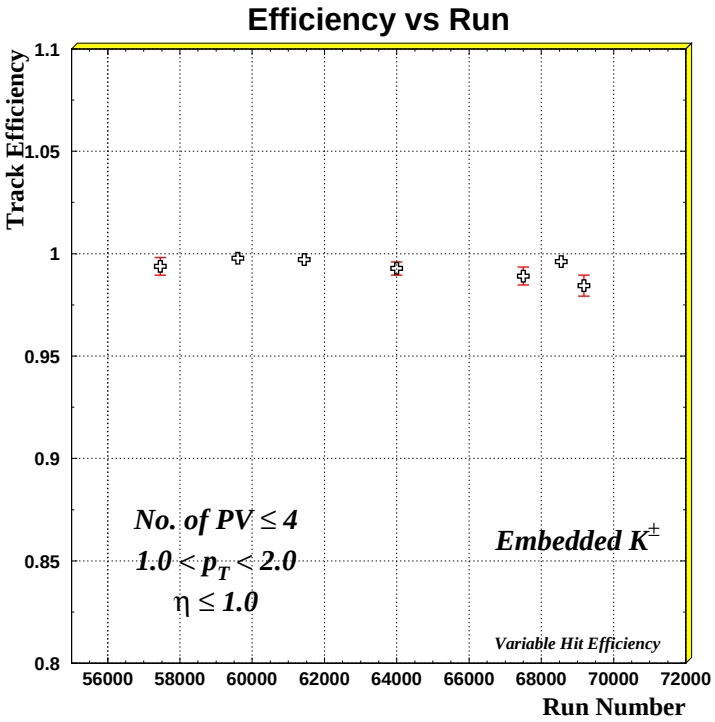

Fig. C.28. Tracking efficiency vs Run for mid momentum tracks.

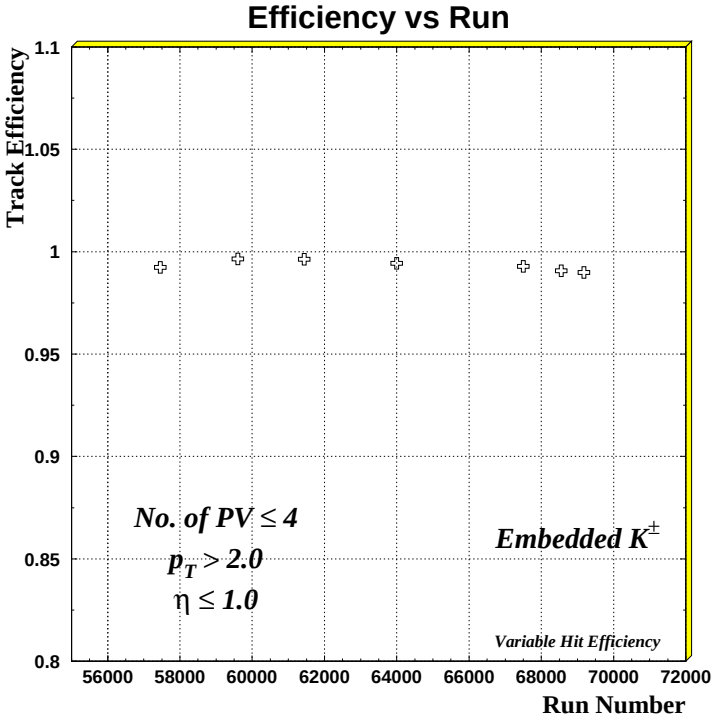

Fig. C.29. Tracking efficiency vs Run for high momentum tracks.

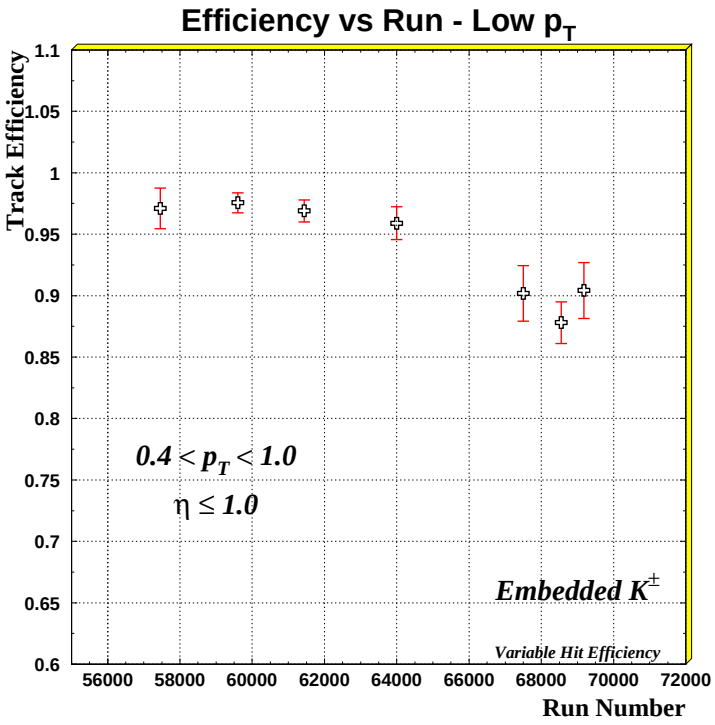

Fig. C.30. Tracking efficiency vs Run for all primary vertex events in the low p_T bin.

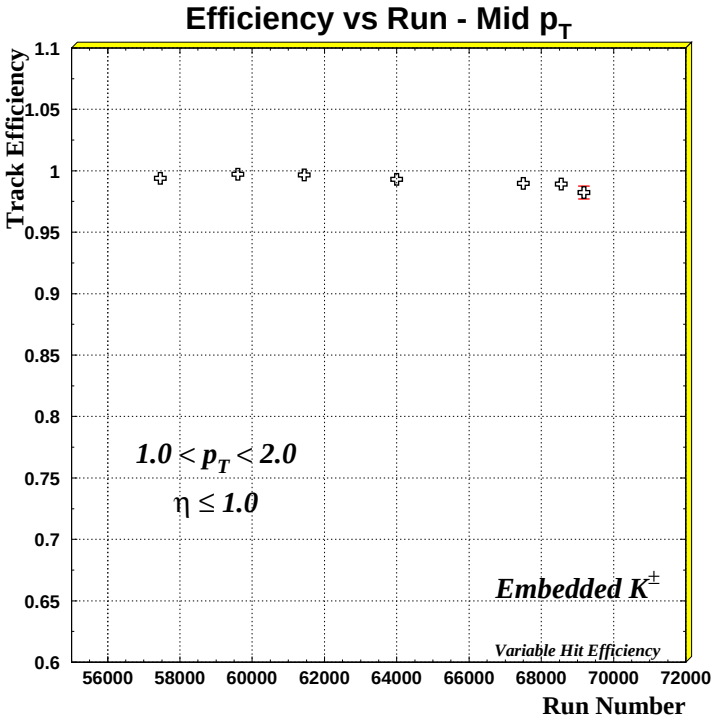

Fig. C.31. Tracking efficiency vs Run for all primary vertex events in the mid p_T bins.

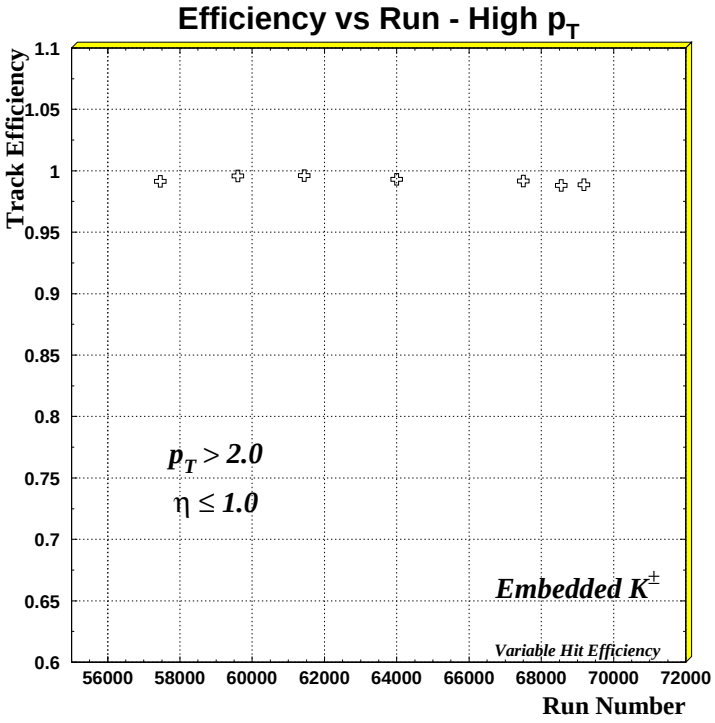

Fig. C.32. Tracking efficiency vs Run for all primary vertex events in the high p_T bins.

C.5 Reconstruction Efficiency Conclusions

We have studied the CTC tracking efficiency by embedding kaons into a sample of displaced J/ψ 's taken from the beginning and the end of the run. Using the muons from the J/ψ decay in the data we have measured the CTC wire-hit efficiencies per super layer for events with one class-12 primary vertex as a function of run number and detector η of the track. We parameterized the wire-hit efficiencies and incorporated them into the embedding procedure.

We find that for tracks with $p_T < 1.0$ GeV/c there is up to a 10% loss in track reconstruction efficiency at the end of run 1B relative to the beginning. Therefore, the reconstruction for low momentum tracks is degrading over the course of the run or the instantaneous luminosity effects have not been completely taken out implying that low p_T tracks are more sensitive to occupancy effects. For tracks with a transverse momentum above 1.0 GeV/c, the track reconstruction efficiency does not change throughout run 1B. Unfortunately, this does not explain the observed loss in the J/ψ yield since the muons coming from the decay will have a transverse momentum of 2.0 GeV/c or greater.

APPENDIX D: KAON MOMENTUM FOR TRACK EMBEDDING

In order to embed a Monte Carlo generated kaon track so that the B^+ mass is preserved when combining it with a J/ψ candidate, the transverse momentum and the angle with respect to the J/ψ must fixed to the appropriate values. Given the angle, α, between the J/ψ and the kaon, the transverse momentum can be calculated. This section outlines the derivatoin the kaon momentum required to obtain a B^+ meson mass when added to the four momenta of the J/ψ.

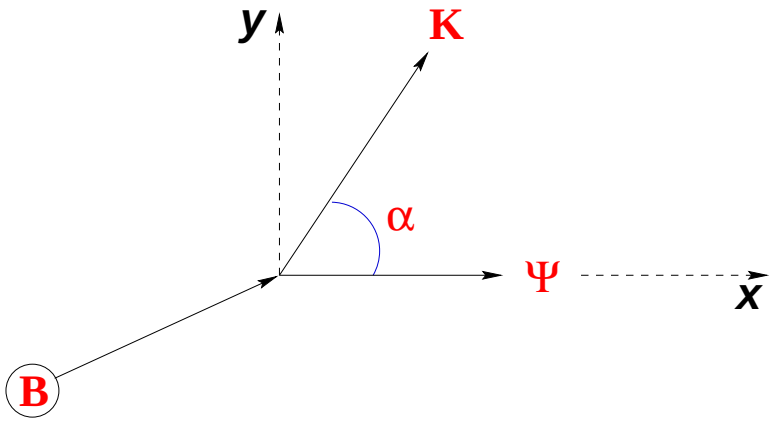

Fig. D.1. Typical B^+ meson decay.

Starting with the invariant mass of the B meson:

$$m_B^2 = E_B^2 - p_B^2 \tag{D.1}$$

$$E_B = E_\Psi + E_K = E_\Psi + \sqrt{m_K^2 + p_K^2} \tag{D.2}$$

Conservation of momentum gives

$$p_{B_x} = p_\Psi + p_K \cos\alpha \tag{D.3}$$

and

$$p_{B_y} = p_K \sin\alpha . \tag{D.4}$$

Combining Equations (D.1) through (D.4) and keeping terms containing p_K on the right hand side of the equation yields

$$\frac{m_B^2 - E_\Psi^2 - m_K^2 + p_\Psi^2}{2} = E_\Psi \sqrt{m_K^2 + p_K^2} - p_\Psi p_K \cos\alpha \tag{D.5}$$

Introducing the following shorthand notation, let

$$A \equiv \frac{m_B^2 - E_\Psi^2 - m_K^2 + p_\Psi^2}{2} \tag{D.6}$$

$$\Rightarrow A = E_\Psi \sqrt{m_K^2 + p_K^2} - p_\Psi p_K \cos\alpha \tag{D.7}$$

and

$$B \equiv \frac{A p_\Psi \cos\alpha}{E_\Psi^2 - p_\Psi^2 \cos^2\alpha} \tag{D.8}$$

then

$$\frac{A^2 - E_\Psi^2 m_K^2}{E_\Psi^2 - p_\Psi^2 \cos^2\alpha} = p_K^2 - 2Bp_K \tag{D.9}$$

Completing the square on the right hand side:

$$\frac{A^2 - E_\Psi^2 m_K^2}{E_\Psi^2 - p_\Psi^2 \cos^2\alpha} = (p_K - B)^2 - B^2 \tag{D.10}$$

Solving for p_K yields:

$$p_K = \sqrt{\frac{A^2 - E_\Psi^2 m_K^2}{E_\Psi^2 - p_\Psi^2 \cos^2\alpha} + B^2} + B \tag{D.11}$$

The resulting momentum preserves the angle between the J/ψ and the kaon allowing reconstruction of the B^+ mass.

BIBLIOGRAPHY

BIBLIOGRAPHY

1. P. Nason, S. Dawson, and R. Ellis. The Total Cross-Section for the Production of Heavy Quarks in Hadronic Collisions. *Nucl. Phys.*, B303:607, 1988.

2. M. Mangano, P. Nason, and G. Ridolfi. Heavy-quark Correlations in Hadron Collisions at Next-to-leading Order. *Nucl. Phys.*, B373:295, 1992.

3. A. Martin, W. Stirling, and R. Roberts. Parton Distributions Updated. *Phys. Lett.*, B306:145, 1993.

4. N. Cabibbo. Unitarity Symmetry and Leptonic Decays. *Phys. Rev. Lett.*, 10:531, 1963.

5. M. Kobayashi and T. Maskawa. CP-Violation in the Renormalizable Theory of Weak Interaction. *Prog. Theor. Phys.*, 49:652, 1973.

6. R.P. Feynman and M. Gell-Mann. Theory of the Fermi Interaction. *Phys. Rev*, 109:193, 1958.

7. J. J. Sakurai. Mass Reveral and Weak Interactions. *Nuovo Cim.*, 7:649, 1958.

8. D. H. Perkins. *Introduction to High Energy Physics*, chapter 2. Addison-Wesley, Menlo Park, California, 3^{rd} edition, 1987.

9. S. L. Glashow. Patial-Symmetries of Weak Interactions. *Nucl. Phys.*, 22:579, 1961.

10. S. Weinberg. A Model of Leptons. *Phys. Rev. Lett.*, 19:1264, 1967.

11. A. Salam. *Weak and Electromagnetic Interactions: Elementary Particle Theory*, chapter 4, page 367. Almqvist and Wiksells, Stockholm, 1968.

12. G. Altarelli and G. Parisi. Asymptotic Freedom in Parton Language. *Nucl. Phys.*, B126:298, 1977.

13. N. Ellis and A. Kernan. Heavy Quark Production at the CERN $p\overline{p}$ Collider. *Phys. Rep.*, 195:23, 1990.

14. Torbjorn Sjostrand. Status of Fragmentation Models. *Int. J. Mod. Phys.*, A3:751, 1988.

15. C. Peterson et al. Scaling Violations in Inclusive e^+e^- Annihilation Spectra. *Phys. Rev. D*, 27(1):105, 1983.

16. J. Chrin. Upon the Determination of Heavy Quark Fragmentation Functions in e^+e^- Annihilation. *Phys. Rev. Lett.*, 67:2418, 1988.

17. Joey Thompson. Introduction to Colliding Beams at Fermilab. FERMILAB-TM-1909, 1994.

18. A WWW primer on the Fermilab accelerator complex, *Concepts Rookie Book*, can be found at the URL address: http://www-bd.fnal.gov/operations/-rookie_books/concepts/conceptstoc.html.

19. Some accelerator parameters can be found on the WWW at the URL address: http://www-fermi3.fnal.gov/.

20. J. R. Snaford. The Fermi National Accelerator Laboratory. *Ann. Rev. Nucl. Sci.*, 26:151, 1976. Note that several parameters have changed since its publication. The ion species previously produced were protons and the energy achieved by the Linac was 200 MeV.

21. A WWW primer on antiproton production and cooling, *Pbar Rookie Book*, can be found at the URL address: http://www-bd.fnal.gov/operations/-rookie_books/pbar_book/contents.html.

22. A. G. Ruggiero. The Fermilab Tevatron I Debuncher Ring. *IEEE Trans. Nucl. Sci.*, 30:2478, 1983.

23. B. Autin, J. Marriner, A. Ruggiero, and K. Takayama. Fast Betatron Cooling in the Debuncher Ring for the Fermilab Tevatron I Project. *IEEE Trans. Nucl. Sci.*, 30:2593, 1983.

24. F. Abe et al. The CDF Detector: An Overview. *Nucl. Inst. Meth. Phys. Res.*, A271:387, 1988.

25. S. Tkaczyk et al. The CDF Silicon Vertex Detector. *Nucl. Phys.*, A342:240, 1994.

26. D. Amidei et al. The Silcon Vertex Detector of the Collider Detector of Fermilab. *Nucl. Phys.*, A350:73, 1994.

27. D. Amidei et al. SVX′: The New CDF Silicon Vertex Detector. *Nucl. Inst. Meth. Phys. Res.*, A360:137, 1995.

28. F. Bedeschi et al. Design and Construction of the CDF Central Tracking Chamber. *Nucl. Inst. Meth. Phys. Res.*, A268:50, 1988.

29. J. Jackson and J. Crawford, Fermilab's Collider Run I, FermiNews, Volume 19, No. 5, page 6, March 8, 1996.

30. D. Amidei et al. A Two Level Fastbus Based Trigger System for CDF. *Nucl. Inst. Meth. Phys. Res.*, A269:51, 1988.

31. F. Abe et al. Evidence of Top Quark Production in $p\bar{p}$ Collisions at $\sqrt{s} = 1.8$ TeV. *Phys. Rev. D*, D50:2966, 1994.

32. J. T. Carroll et al. The CDF Level 3 Trigger. *Nucl. Inst. Meth. Phys. Res.*, A300:552, 1991. Although several important details have since changed, the design philosophy and the interaction with the DAQ system are rather similar to the recent versions of the Level 3 trigger system.

33. A. Warburton. Run 1A and 1B Low-p_T Single- and Double-Track CTC Pattern Recognition Efficincies. CDF Note 4139, 1997.

34. C. Caso et al. Review of Particle Physics. *Eur. Phys. J.*, C3(1-4), 1998.

35. F. Abe et al. Transverse-Momentum Distributions of Charged Particles Produced in $p\overline{p}$ Interactions at $\sqrt{s} = 630$ and 1800 GeV. *Phys. Rev. Lett.*, 61:1819, 1988.

36. A. D. Martin, R. G. Roberts, W. J. Stirling, and R. S. Thorne. Update of MRST Partons. 1999.

37. P. Avery, K. Read, and G. Trahern. QQ: A Monte Carlo Generator. Internal Software Note CSN-212, 1985.

38. S. Pappas, J. Lewis, and G. Michail. Run 1B Low p_T Central Dimuon Trigger Efficiencies. CDF Note 4076, 1997.

39. C. Anway-Weise. Offline Muon Matchin Cuts. CDF Note 1986, 1993.

40. K. Ohl, V. Papadamitriou, and T. Rodrigo. Update on Υ Cross Section Measurements. CDF Note 3052, 1995.

41. T. Keaffaber et al. CTC Track Reconstruction Efficiency Studies. CDF Note 4768, 1999.

42. G. Feild et al. Study of Run 1B Data Sets. CDF Note 4312, 1998.

43. Greg Feild, Jonathan Lewis, and Michail Schmidt. J/ψ Cross Sections and Instantaneous Luminosity. CDF Note 4769, 1999.

44. D. Cronin-Hennessy and A. Beretvas. Luminosity at CDF. CDF Note 4721, 1998.

45. M. Bailey et al. Measuring the b Quark Cross Sections Using the Exclusive Decays $B^{\pm} \to J/\psi K^{\pm}$ and $B^0 \to J/\psi K^{*0}$. CDF Note 1994, 1993.

46. F. Abe et al. Measurement of b quark fragmentation fractions in the production of strange and light B mesons in p anti-p collisions at S**(1/2)=1.8-TeV. *Phys. Rev.*, D60:092005, 1999.

47. H. L. Lai et al. Global QCD Analysis of Parton Structure of the Nucleon: CTEQ5 Parton Distributions. hep-ph/9903282, 1999.

48. A. Caner et al. Tracking Efficiency for Soft Lepton Tagging. CDF Note 2363, 1993.

49. M.W. Bailey et al. CTC Tracking Efficiency for the B Cross-Section Analysis. CDF Note 2815, 1994.

50. J.B. Gonzalez et al. Measurement of the CTC Tracking Efficiency, Offline Version 7_09, for $B^{\pm} \to J/\psi K^{\pm}$, $B^0 \to J/\psi K^0_s$, and $B^{\pm} \to J/\psi K^{*\pm}$. CDF Note 3010, 1994.

51. H. Wenzel, K. Maeshima, D. Benjamin, , and E. Hayshi. A Study of the CTC Tracking Performance during Run 1B. CDF Note 3421, 1995.

52. P. Ngan and P. Spicas. Luminosity Dependence of 1B J/ψ Yield. CDF Note 4313, 1997.

53. J. Lewis and P. Avery. CLEOMC: The Interface to the CLEO Monte Carlo (QQ). CDF Note 2724, 1994.

54. The hit embedding machinery was the work of Aseet Mukherjee.

VITA